Citation: Swayze, G.A., R.N. Clark, A.F.H. Goetz, K.E. Livo, G.N. Breit, F.A. Kruse, S.J. Stutley, L.W. Snee, H.A. Lowers, J.L. Post, R.E. Stoffregen, and R.P. Ashley, 2014, Mapping advanced argillic alteration at Cuprite, Nevada using imaging spectroscopy: Economic Geology, v. 109, no. 5, p. 1179-1221. doi: 10.2113/econgeo.109.5.1179

Mapping Advanced Argillic Alteration at Cuprite, Nevada Using Imaging Spectroscopy

Gregg A. Swayze[1], Roger N. Clark[1], Alexander F.H. Goetz[2], K. Eric Livo[1], George N. Breit[1], Fred A. Kruse[3], Stephen J. Sutley[1], Lawrence W. Snee[1], Heather A. Lowers[1], James L. Post[4], Roger E. Stoffregen[5], and Roger P. Ashley[6]

[1] U.S. Geological Survey, MS 964 Box 25046
Denver Federal Center, Denver, CO 80225
(303) 236-0925 email: gswayze@usgs.gov

[2] University of Colorado, Department of Geological Sciences, Emeritus
Boulder, CO 80309

[3] Physics Department and Remote Sensing Center
Naval Postgraduate School
Monterey, CA 93943

[4] 740 Zion St., Nevada City, CA 95959

[5] AWK Consulting Engineers, 1225 Rodi Rd.
Turtle Creek, PA 15145

[6] U.S. Geological Survey, 345 Middlefield Rd.
Menlo Park, CA 94025

Version 5.0

Abstract

Mineral maps based on Airborne Visible/Infrared Imaging Spectrometer (AVIRIS) data were used to study late Miocene advanced argillic alteration at Cuprite, Nevada. Distributions of Fe-bearing minerals, clays, micas, sulfates, and carbonates were mapped using the Tetracorder spectral-shape matching system. The Al-content of white micas increases toward altered areas and near intrusive rocks. Alunite composition varies from pure K to intimate mixtures of Na-K endmembers with subpixel occurrences of huangite, the Ca-analogue of alunite. Intimately mixed Na-K alunite marks areas of relatively lower alteration temperature, whereas co-occurring Na-alunite and dickite may delineate relict hydrothermal conduits. The presence of dickite, halloysite, and well-ordered kaolinite but absence of disordered kaolinite is consistent with acidic conditions during hydrothermal alteration. Partial lichen cover on opal spectrally mimics chalcedony, limiting its detection to lichen-free areas. Pods of buddingtonite are remnants of initial quartz-adularia-smectite alteration. Thus, spectral maps provide a synoptic view of the surface mineralogy, and define a previously unrecognized early steam-heated hydrothermal event.

Faulting and episodes of hydrothermal alteration at Cuprite were intimately linked to upper plate movements above the Silver Peak – Lone Mountain detachment and growth, collapse, and resurgence of the nearby Stonewall Mountain volcanic complex between 8 and 5 Ma. Isotopic dating indicates that hydrothermal activity started at least by 7.61 Ma and ended by about 6.2 Ma. Spectral and stable isotope data suggests that Cuprite is a late Miocene low-sulfidation adularia – sericite type hot spring deposit overprinted by late-stage steam-heated advanced argillic alteration formed along the margin of the Stonewall Mountain caldera.

Introduction

Remote sensing has been used as a tool to examine hydrothermal alteration from airborne and orbital satellite platforms for the past four decades. These sensors have become more sophisticated resulting in lower detection limits, potential detection of a greater number of materials, and finer spatial resolution. Recently, portable field spectrometers have become widely accepted by the economic geology community for evaluating exposed alteration assemblages that may be linked to ore mineralization (Thompson et al., 1999 and references therein; Herrmann et al., 2001; Ducart et al., 2006; Chang et al., 2011; Kerr et al., 2011). Spectroscopy is also playing an increasing role in analyses of alteration in drill cores (Cudahy et al., 2009; Thompson et al., 2009; Kruse et al., 2011; Haest et al., 2012; Harraden et al., 2013). The present study aims to build on the utility of portable spectrometers by demonstrating that spectral features attributable to surface mineralogy can be resolved regardless of the distance between the sensor and the surface.

Many minerals formed by alteration during hydrothermal mineralization are stable over limited pH and temperature ranges (White and Hedenquist, 1995). Understanding their distribution facilitates reconstruction of hydrothermal conditions. Imaging spectroscopy (or hyperspectral imaging, HSI) over the visible to near-infrared (VIS-NIR or VNIR-SWIR) 0.4 to 2.5 μm range is an effective tool for evaluating subtle patterns of hydrothermal alteration in areas with sparse vegetation. Thompson et al. (1999) noted that reflectance spectroscopy could identify many of the fine-grained phases associated with argillic and advanced argillic alteration that are difficult to identify with traditional field methods. It can be used to identify some alteration minerals better than some laboratory methods including standard X-ray diffraction

(Swayze et al., 2000).

Our goal is to show how information from imaging spectroscopy can be integrated with more traditional exploration methods by demonstrating its effectiveness for mapping hydrothermal alteration at Cuprite, Nevada. This desert site is ideally suited for remote sensing because of its diverse alteration mineralogy, excellent rock exposures, sparse vegetation, dry climate, and relatively easy access. Although the Cuprite area has been intensively prospected for sulfur and mercury, and mined for silica, no significant precious metal mineralization has been recognized (Buchanan and McDonald, 1989, unpublished report). Cuprite was selected as the study area because it has the same advanced argillic alteration assemblage present at many ore deposits (Ashley and Abrams, 1980), but the Cuprite area has been minimally disturbed by mining activities.

The Cuprite mining district is located about 200 km northwest of Las Vegas, Nevada along U.S. Highway 95, about 14 km south of Goldfield, NV (Fig. 1). Cuprite served as one of the test sites for some of the first broadband remote sensing instruments (Rowan et al., 1974; Abrams et al., 1977; Ashley and Abrams, 1980) and later for some of the first hyperspectral (imaging spectrometer) instruments (Goetz et al., 1985; Kruse et al., 1990). A previously undetected occurrence of the NH_4-mineral buddingtonite was discovered with imaging spectroscopy at Cuprite (Goetz and Strivastava, 1985). The Cuprite area has been the subject of numerous other remote sensing studies (Swayze, 1997 and references therein; Rowan et al., 2003; Clark et al., 2003; Swayze et al., 2003; Mars and Rowan, 2006; Mars and Rowan, 2010; Chen et al., 2010; and many others) involving the use of airborne and orbital visible, near-infrared, and thermal-infrared sensors.

Many recent remote sensing studies of Cuprite have focused on instrument performance and spectral identification techniques, and less on integrating the spectral results with the hydrothermal and geologic framework of the area. This study presents such integration as a means to demonstrate the utility of imaging spectroscopy for exploration in frontier areas. The first half of the paper explains how spectral measurements of alteration minerals (i.e., white mica, alunite, kaolinite, and hydrated silica) have advanced beyond identification to a level where subtle changes in their spectra can provide information about the environment in which they form and how that helps us understand alteration at Cuprite. The second half of the paper deals with a reinterpretation of Cuprite geology because much of the information presented here is new.

Geologic Setting of Cuprite

The Cuprite area contains well-exposed zones of advanced argillic alteration distributed around two centers on each side of U.S. Highway 95 (Ashley and Abrams, 1980). The altered areas are along the western margin of the Stonewall Mountain Caldera (Figs. 1 and 2). Stonewall Mountain is one of a group of middle to late Miocene potassic to peralkaline volcanic centers, collectively known as the Southwestern Nevada Volcanic Field. The field trends NW across the southern part of the Great Basin (Noble et al., 1976). Cuprite and Stonewall Mountain are located within the transtensional Walker Lane Belt, a 100 km wide NW-trending depression extending 800 km north from the Las Vegas area to south central Oregon (Stewart, 1988; inset Fig. 1), which separates the Great Basin from the Sierra Nevada (Oldow, 1994). Albers and Stewart (1972), Abrams et al. (1977), and Ashley and Abrams (1980) have prepared geologic maps of the Cuprite area. West of highway 95, altered rocks include Cambrian metasedimentary rocks, Tertiary conglomerates, and intrusive rocks composed of quartz latite and

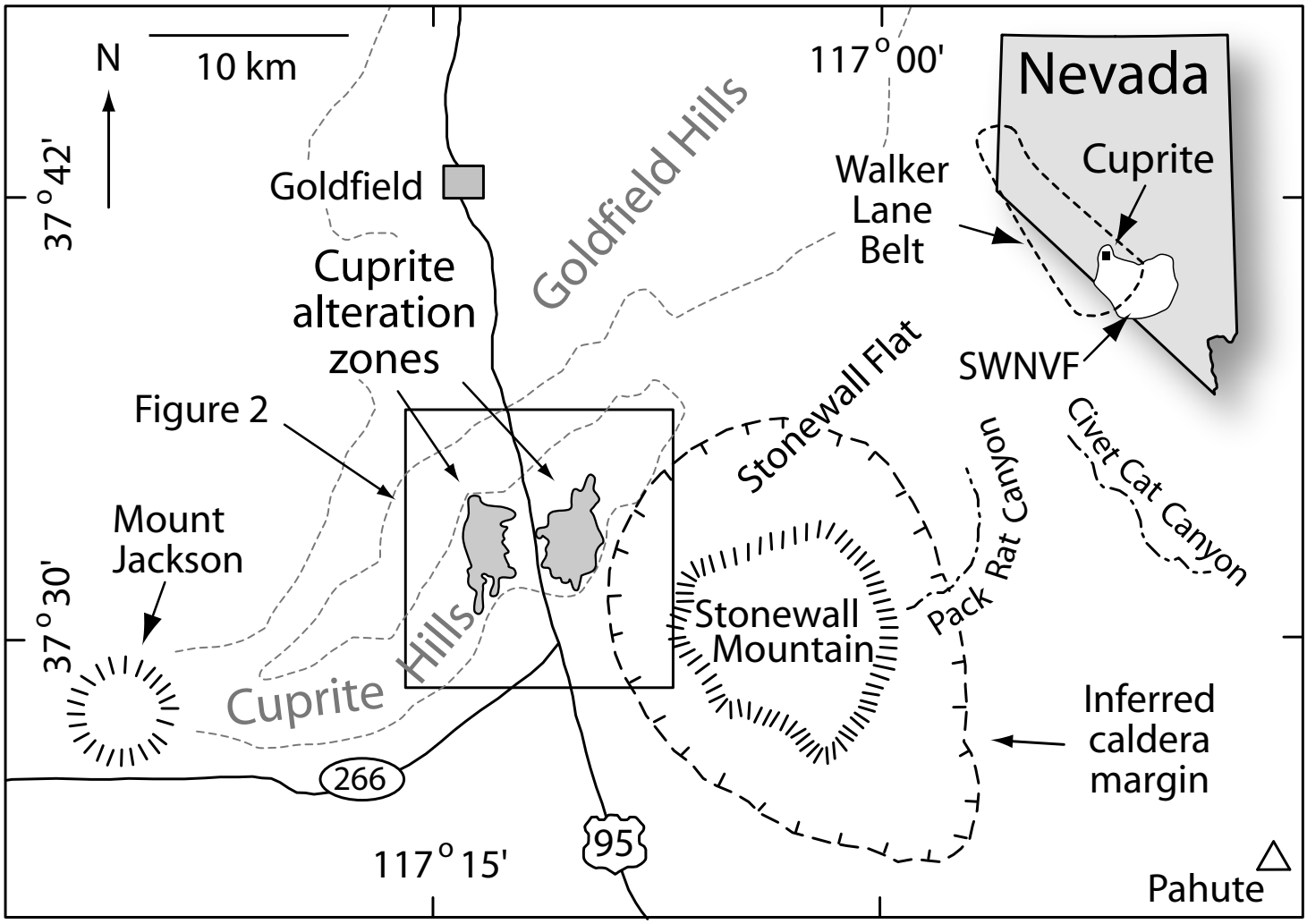

Fig. 1. Location of the Cuprite study area relative to the inferred margin of the late Miocene-age Stonewall Mountain Caldera in Southwestern Nevada modified from Noble et al. (1988). Locations of Southwestern Nevada Volcanic Field (SWNVF) and Walker Lane Belt from Grauch et al. (1999). Borders of the Cuprite and Goldfield hills shown in light gray dashed lines.

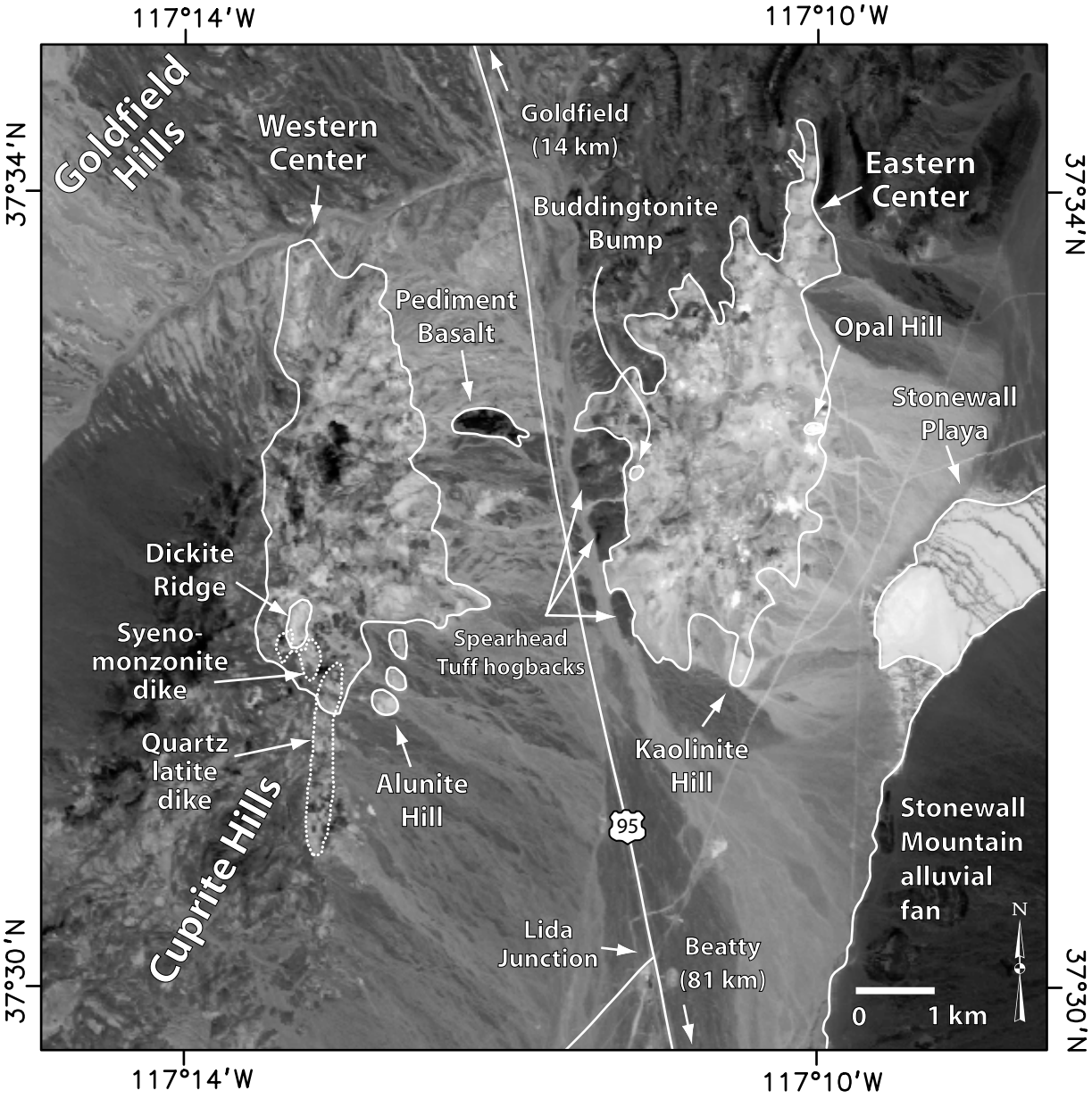

Fig. 2. Single channel (0.64 μm) Airborne Visible/Infrared Imaging Spectrometer (AVIRIS) image of hydrothermal alteration at Cuprite. Points of interest are discussed in the text.

syenomonzonite. East of the highway, altered rocks include Tertiary rhyolitic ash-flow and air-fall tuffs, conglomerate, and basalt (Fig. 3). For convenience, the foci of the two areas of hydrothermal alteration are referred to as the western and eastern centers. The two centers are separated by a nearly 2-km wide pediment of Quaternary age. Details of these rock units are presented below.

Exposed phyllites, quartzites, and limestone that crop out at Cuprite are part of the lower Cambrian Harkless Formation (Ch) and Mulespring Limestone (Cms). Exposures of interlayered limestone and chert, located west of the Harkless phyllite outcrops, belong to the upper Cambrian Emigrant Formation (Ce). These miogeoclinal rocks, underwent complex thrusting and low-temperature metamorphism during middle Jurassic and early Cretaceous magmatism and deformation (Albers and Stewart, 1972). Cambrian rocks exposed in the western center are part of an arcuate northeast to west-trending range known as the Cuprite Hills. This range and the nearby Goldfield Hills (Fig. 1) are probable fault blocks in the relatively unmetamorphosed upper plate of the Silver Peak – Lone Mountain detachment, part of a low-angle displacement transfer system active from 11 to 4.8 Ma between the Owens Valley and Furnace Creek faults to the west and Walker Lane transcurrent faults to the east (Oldow et al., 1994).

The altered quartz latite dike (Tql) exposed at the southern end of the western center (Fig. 3) is probably of Tertiary age, but no crosscutting relationships with Tertiary volcanic units have been observed (Ashley and Abrams, 1980). This dike may be related to quartz latite rocks encountered in boreholes of the pre-Tertiary section in the pediment between the centers (Swayze, 1997).

The oldest Tertiary volcanic unit (Tw), which covers parts of the eastern center, is a crystal-rich rhyolite or quartz latite ash-flow tuff characterized by quartz, sanidine, plagioclase, and biotite phenocrysts (Ashley and Abrams, 1980). Where it is unaltered, it can be distinguished from overlying tuff units by abundant biotite phenocrysts. $^{40}Ar/^{39}Ar$ dating of a sample collected 3.5 km north of the western center gives an age of 26.99 ± 0.08 Ma (Table 1), suggesting that this unit may be related to the 28.6 ± 6.4 Ma Sandstorm Rhyolite (Ashley and Silberman, 1976) exposed in the Goldfield area. This volcanic unit lies directly on the Harkless phyllite at the collection locality, but due to an incomplete section the unit's original thickness is unknown. In the eastern center, an air-fall pumice-lapilli tuff of variable thickness overlies the crystal-rich rhyolitic tuff. Ashley and Abrams (1980) correlate this unit with exposures of the 13 - 16 Ma Siebert Tuff at Goldfield. The poorly welded Siebert Tuff (Tst) varies in thickness locally from 0 to 60 meters due to erosion, being thickest in the middle of the eastern center.

In the eastern center, stream channels eroded into the Siebert Tuff are filled with a conglomerate composed mostly of altered phyllite clasts and lesser volcanic clasts. Ashley and Abrams (1980) considered this conglomerate to be part of the Siebert unit. The presence of phyllite clasts, some altered to advanced argillic grade, is consistent with derivation from eroded Harkless phyllite exposed in the western center after the onset of hydrothermal alteration there, suggesting that the conglomerate is 5 to 8 m.y. younger than the Siebert Tuff (Swayze, 1997). This unit is herein informally referred to as the Cuprite Hills conglomerate (Tch) and is not a formally recognized stratigraphic unit. A porphyritic plagioclase-olivine basalt flow (Tb1) overlies the conglomerate in the eastern center (Ashley and Abrams, 1980). Intense alteration and complex faulting make it difficult to determine whether the basalt is interbedded with the conglomerate at this location.

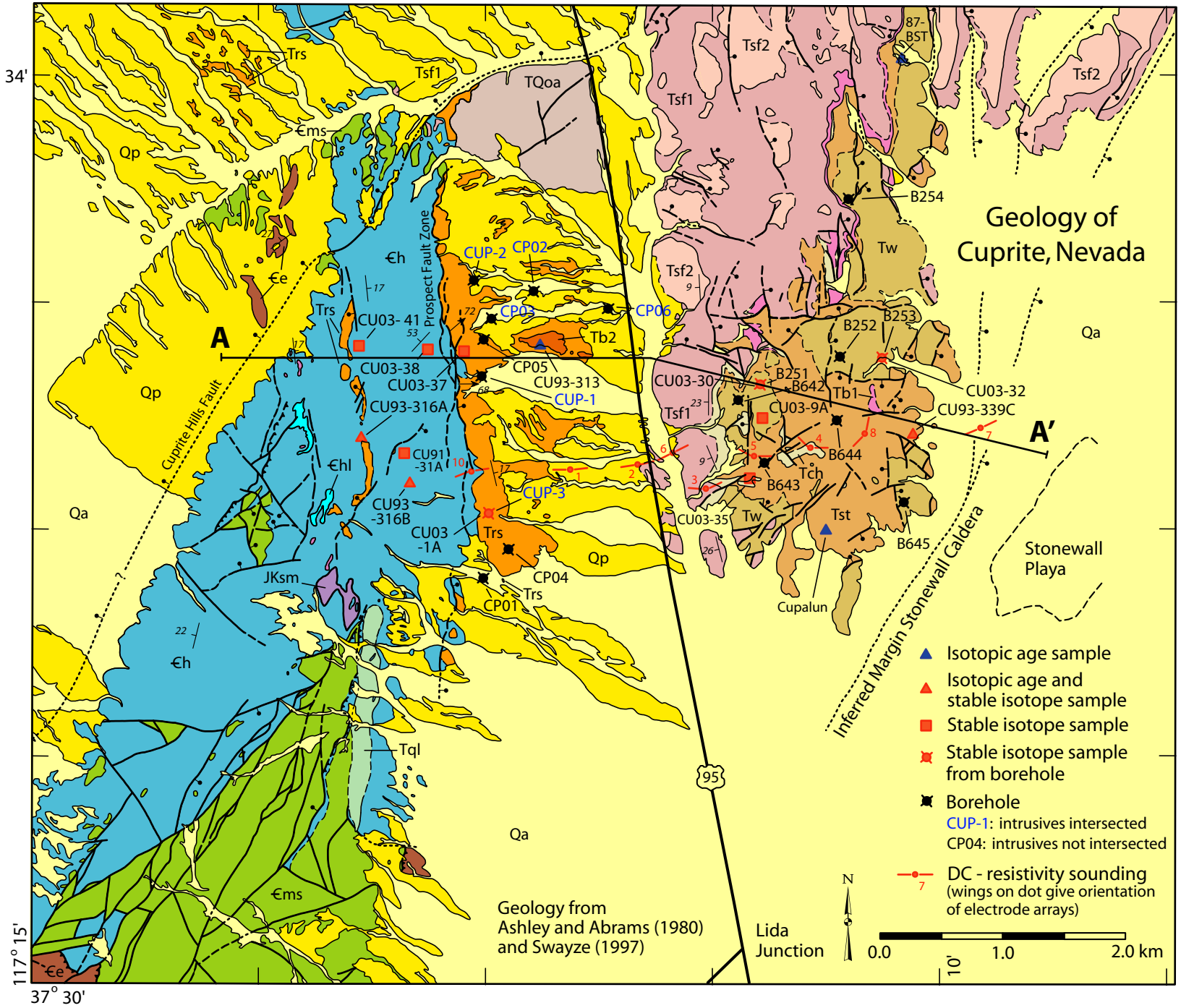

Fig. 3A. Geologic map of the Cuprite area. Faults and geologic contacts are long dashed where approximately located; short dashed where inferred; dotted where concealed. Ball symbols are placed on the downthrown block of faults. Borehole symbols with blue labels indicate intrusive rocks were intersected. Line labeled A --- A' shows position of cross section shown in Figure 23. Units defined in Fig. 3B.

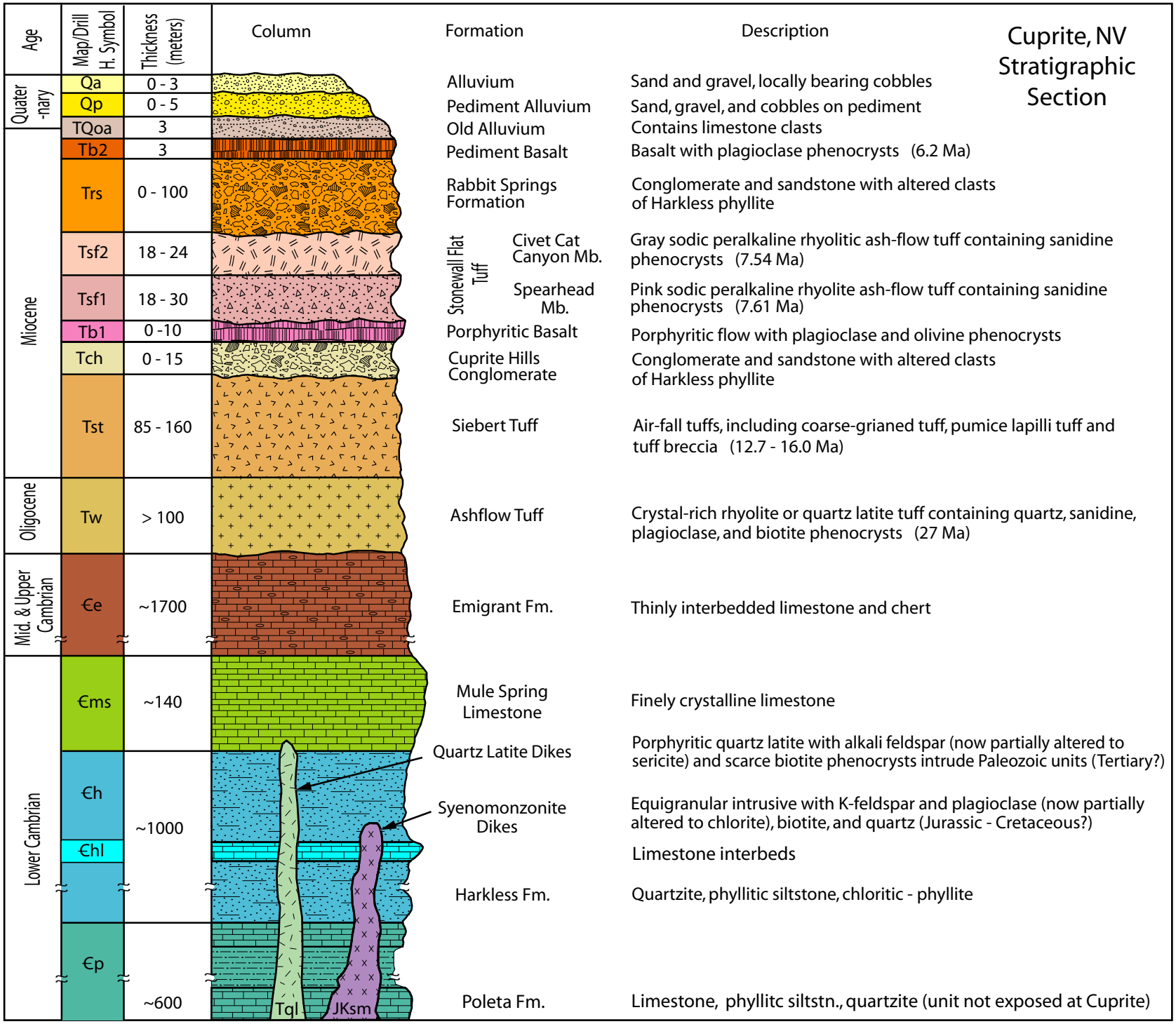

Fig. 3B. Stratigraphic section of the Cuprite area (and map key for Fig. 3A) compiled from Ashley and Abrams (1980), Albers and Stewart (1972), and unpublished borehole logs. Isotopic dates from sources listed in Table 1.

Table 1. Isotopic ages for geologic rock units and altered rocks at Cuprite, Nevada.

Unit	Sample	Method	Age ± 2σ	Location	Source
Coarse-grained alunite veinlet, Siebert tuff (Tst) Ectr	Cupalun	K/Ar alunite	6.0 ± 0.6	N37° 32' 00" W117° 10' 30"	Noble et al., 1988
Pediment basalt (Tb2) K_2O= 2.49 wt% $^{40}Ar^*$=2.21502x10^{-11}mol/g $^{40}Ar^*/\sum^{40}Ar$=38.8%	CU93-313	K/Ar whrx	6.2 ± 0.2	N37° 32' 50" W117° 12' 11"	Present study & Swayze (1997)
Bladed vein alunite, Harkless fm. (Ch) Wctr (g.s. 100 to 400 μm)	CU93-316B	$^{40}Ar/^{39}Ar$ alunite	6.21 ± 0.06	N37° 32' 13" W117° 12' 54"	Present study
Fine-grained alunite, Harkless fm. (Ch) Wctr (g.s. 10 to 40 μm)	CU93-316A	$^{40}Ar/^{39}Ar$ alunite	6.48 ± 0.06	N37° 32' 25" W117° 13' 11"	Present study
Fine-grained alunite, Siebert Tuff (Tst) Ectr (g.s. 10 to 50 μm)	CU93-339C	$^{40}Ar/^{39}Ar$ alunite	6.86 ± 0.1	N37° 32' 26" W117° 10' 11"	Present study
Civet Cat Canyon mb. of Stonewall Flat Tuff (Tsf2)	BH86N33	$^{40}Ar/^{39}Ar$ sanidine	7.54 ± 0.06	Various Locations	Hausback et al., 1990
Spearhead mb. of Stone-wall Flat Tuff (Tsf1)	Mean of 3 samples	$^{40}Ar/^{39}Ar$ sanidine	7.61 ± 0.06	Various Locations	Hausback et al., 1990
Siebert Tuff (Tst)	51-12 164-69 164-19 164-69	K/Ar biotite biotite sanidine plagioclase	 12.7 ± 0.6 14.2 ± 0.6 16.0 ± 0.6 14.6 ± 4.8	Goldfield, NV	Ashley and Silberman, 1976; Silberman and McKee, 1972
Phenocryst-rich rhyolitic ash-flow tuff (Tw)	87-BST	K/Ar sanidine	19.8 ± 1.2†	N37° 34' 05" W117° 10' 12"	Noble et al., 1988
Biotite-crystal-rich rhyolitic tuff (Tw)	CU93-45	$^{40}Ar/^{39}Ar$ sanidine	26.99 ± 0.08	N37° 35' 13" W117° 13' 33" (GPS)	Present study

K/Ar: Potassium-Argon isotopic age; $^{40}Ar/^{39}Ar$: ^{40}Argon/ ^{39}Argon mineral thermal-release age; whrx = whole rock analysis; fm. = formation; mb. = member; Ectr = eastern center; Wctr = western center; g.s. = grain size of alunite. Sample location is ±100m or better, unless GPS is specified then location is accurate to within ± 15m or better (using NAD27 datum). $^{40}Ar^*$ refers to radiogenic argon. †Sample 87-BST is from argillic zone so date may be suspect.

The rhyolitic Stonewall Flat Tuff, the uppermost unit in the eastern center, is composed of the Spearhead (Tsf1) and overlying Civet Cat Canyon (Tsf2) members, which originated from the nearby (5 km distant) Stonewall Mountain volcanic center (Noble et al., 1984). Isotopic dating by Hausback et al. (1990) has revised the age of the Spearhead member to 7.61 ± 0.06 Ma and the Civet Cat Canyon member to 7.54 ± 0.06 Ma. The Stonewall Caldera formed during the eruption of the Civet Cat Canyon member (Foley, 1978; Noble et al., 1984; Weiss and Noble, 1989). Post-eruption faults offset both members of the Stonewall Flat Tuff down-to-the-east, in three NE-trending en echelon fault blocks parallel to the inferred caldera margin just north of the eastern center (Fig. 3A; Swayze et al., 1997). Immediately north of the western center, Spearhead Tuff lies directly on Harkless phyllite and Mulespring Limestone.

Erosional outliers of a conglomerate lithologically similar to, but coarser than the Cuprite Hills conglomerate, unconformably overlie the Harkless phyllite along the topographically highest points of the western center (Fig. 3A). Similar conglomerate crops out northwest of the western center (Ashley and Abrams, 1980). At the northeastern corner of the western center (Fig. 3A) this conglomerate contains fragments of Spearhead Tuff. These scattered conglomerate exposures are considered the stratigraphic equivalent of a thin discontinuous layer of sandstone and conglomerate overlying the Stonewall Flat Tuff west of Goldfield, known as the Rabbit Springs Formation (Trs) (Ransome, 1909). This conglomerate crops out along nearly the entire length of the N–S trending normal faults that form the eastern margin of the Cuprite Hills, the range containing the western center. This set of faults is herein referred to as the Prospect Fault Zone. These and other exposures of conglomerate (labeled Trs) located between the alteration centers and partially concealed by pediment gravels, were originally classified by Albers and Stewart (1972) as Siebert Tuff. Borehole logs indicate that this conglomerate overlies the Stonewall Flat Tuff in the subsurface beneath the pediment (Swayze, 1997). A small, isolated plagioclase-olivine basalt flow (Tb2), isotopically dated at 6.2 ± 0.2 Ma and herein referred to as the pediment basalt (Figs. 2 and 3), overlies this conglomerate. Several pediment surfaces formed between the alteration centers during the late Tertiary and/or Quaternary (Ashley and Abrams, 1980). These include a particularly well-developed pediment surface underlain by alluvial gravels (TQoa), which consist of phyllite and limestone clasts eroded from exposures in the Goldfield Hills northwest of the western center. A younger pediment (Qp) is laterally surrounded by more recent alluvial material eroded from the alteration centers.

Hydrothermal Alteration at Cuprite

Cambrian metasedimentary rocks in the western center and Tertiary volcanic rocks in the eastern center are in places pervasively altered to advanced argillic assemblages. Ashley and Abrams (1980) divided altered rocks into silicified, opalized, and argillized map units (Fig. 4). Silicified rocks consist of quartz, chalcedony, minor alunite and kaolinite, and post-alteration calcite after opal (Ashley and Abrams, 1980). Where these rocks crop out they are vuggy and in places have stockwork texture with silica defining fractures that served as conduits for acidic hydrothermal fluids. Opalized rocks are the most laterally extensive of the alteration zones and contain minor alunite and kaolinite. In this zone, primary quartz phenocrysts remain as relicts with unaltered sanidine phenocrysts present in alunite-free opalized rocks. Argillized areas, located within the opalized zones or at the edge of the altered areas, contain kaolinite after plagioclase with glass altered to opal, montmorillonite, and kaolinite. The alteration zones of Ashley and Abrams (1980) were mapped using traditional field, laboratory, and broadband

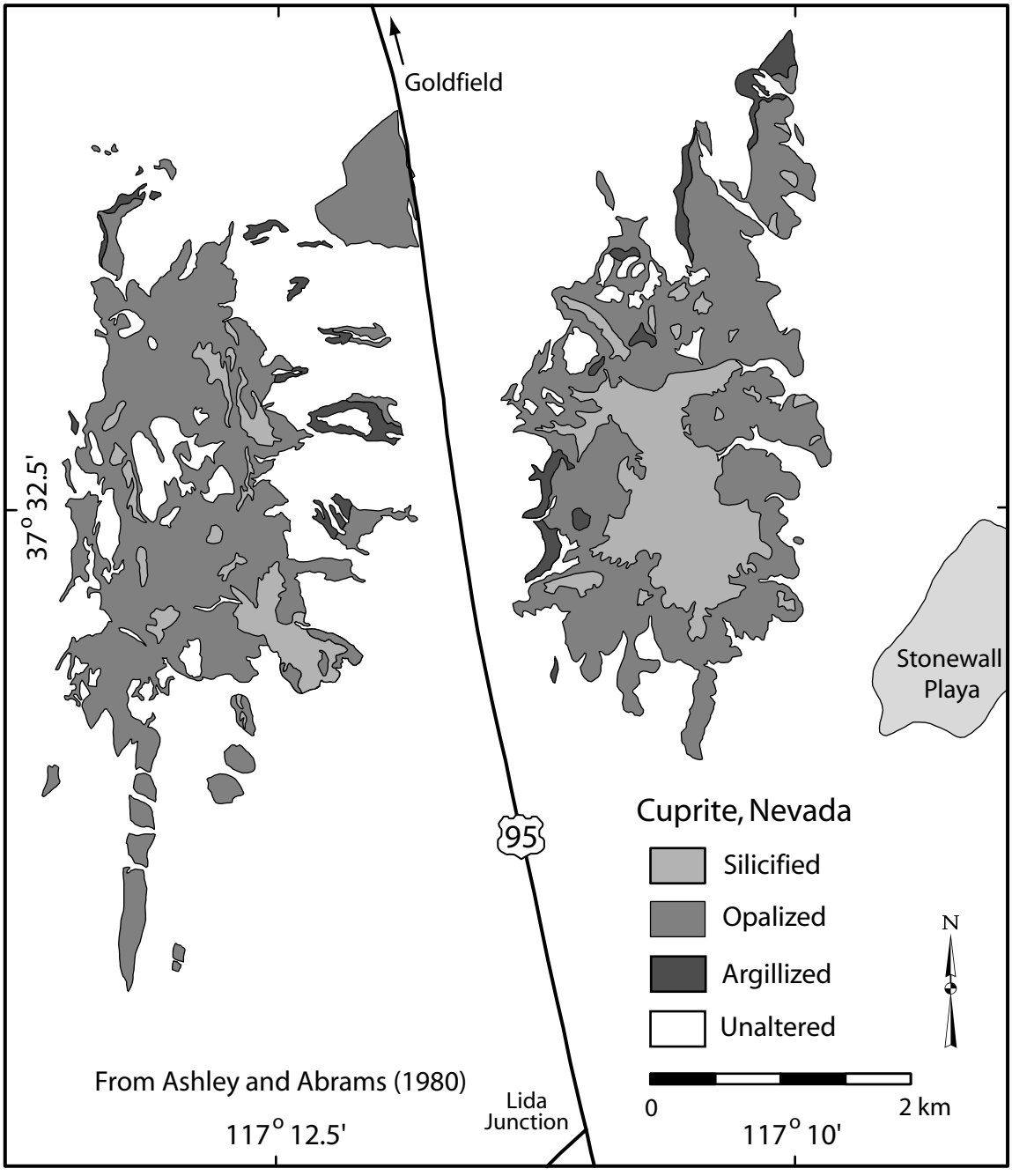

Fig. 4. Alteration map of the Cuprite area based on field mapping by Ashley and Abrams (1980).

remote sensing techniques. This study builds on those pioneering results by using imaging spectroscopy to describe the spatial distribution of a greater number of spectrally detectable alteration minerals.

Analytical Methods and Data Collection

There are a variety of electronic and vibrational processes that shape reflectance spectra of surface materials (Farmer, 1974; Hunt, 1977; Burns, 1993; Clark, 1999). The electronic absorptions primarily range from wavelengths of 0.1 to about 1.3 μm and vibrational absorptions are primarily beyond 0.9 μm. Both spectral regions can be used to identify phases in surface materials, although each provides spectral information originating from different mechanisms. Electronic absorptions arise from charge transfers and crystal field effects of the transition metals, conduction bands, and color centers (Burns, 1993). In this study we refer to the 0.4 to 1.3 μm region as the electronic absorption region. Vibrational absorptions arise from vibrational modes of molecular bonds (Farmer, 1974). In this study we use overtone and combination absorptions in the reflected light portion of the spectrum located within the 1.3 to 2.5 μm region, herein referred to as the vibrational region. These overtone and combination absorptions occur at shorter wavelengths than the fundamental absorptions and are an order of magnitude weaker, but are enhanced by increased penetration due to weaker absorption thus allowing them to be detected with reflectance spectroscopy. Because electronic and vibrational processes are active in different wavelength regions, different classes of surface materials can be identified simultaneously using information from these two spectral regions (Hunt, 1977; Clark et al., 2003).

Spectral Data Collection and Calibration

The spectral region from 0.4 to 2.5 μm is the wavelength range used by most terrestrial imaging spectrometers that measure reflected light because that spectral region of the Earth's atmosphere is reasonably transmissive and there is limited interference from thermal emission from the surface. The Airborne Visible/InfraRed Imaging Spectrometer (AVIRIS) is a NASA/Jet Propulsion Laboratory whiskbroom scanner that collects spectra in a cross-track manner using an oscillating mirror to sequentially reflect light from each spatial location (pixel) on the ground to a spectrometer one pixel at a time. AVIRIS collects spectra in 224 continuous spectral channels covering the wavelength range 0.38 - 2.5 μm with an approximately 10-nm spectral sampling interval and bandpass width (Green et al., 1998). Because AVIRIS measures reflected sunlight, it can only provide information on minerals exposed in the top tens of microns to few millimeters of the surface. Thus, thick vegetation cover can totally obscure the ground surface.

The AVIRIS data used for this study were collected over Cuprite on June 23, 1995 at local noon under high visibility conditions by a NASA ER-2 aircraft flying at an altitude of 20 km, producing an image of the surface 10.5 km wide and 614 pixels across, where each pixel is composed of a spectral measurement of a 17 x 17 m spot on the ground. Solar flux, atmospheric absorptions, and path radiance (atmospheric scattering) were removed from the AVIRIS radiance data using a model-based atmospheric correction program called ATREM (Gao et al., 1993). Artifacts remaining after ATREM processing were removed by subtracting a correction for residual path radiance from the data and then multiplying by correction factors derived from field spectra of nearby Stonewall Playa using the method of Clark et al. (2002). A total of 150 spectral measurements covering approximately 500 m^2 of the playa surface were collected at

noon one day after the flight with an ASD Inc. Fieldspec® FR Spectrometer. These spectra were averaged and corrected to absolute reflectance. Shadowed areas north of the eastern center were used to derive the residual path radiance correction. Images were georeferenced using the CO_2 band-depth-derived digital elevation model method of Clark et al. (1998; 2003) followed by a first-degree polynomial stretch to orthophoto reference points, providing a 9 m root mean square error for the final registration.

Spectral Mapping

AVIRIS data calibrated to apparent reflectance were spectrally mapped using the Tetracorder System (Clark et al., 2003). Tetracorder uses a modified band-shape fitting technique to spectrally identify materials and vegetation to create maps of their distribution. The primary algorithm works by comparing absorption features in library reference spectra to absorption features in an observed spectrum (e.g., from an AVIRIS pixel) and then calculating a modified linear least-squares correlation between them. The correlation coefficient is called the "*fit*." The algorithm derives *fits* for all of the spectra in its library, applies constraints on absorption features, and selects the material with the highest *fit* as the best spectral match to the observed spectral features. In most cases, Tetracorder identifies the spectrally dominant material(s) in the 1- and 2-μm spectral regions where electronic and vibrational processes dominate respectively; it is capable of identifying mixtures (e.g., alunite + kaolinite) if representative spectra of those mixtures are added to its library. Unique colors are assigned for each different material successfully identified by the spectral analysis and these are applied to each pixel to create maps of alteration phase distribution.

When Tetracorder identifies a phase as spectrally dominant, that phase does not have to be pure, it may be present with in a multiminerallic coating or in an intimate or areal mixture with other phases exposed at the ground surface. Intimate mixtures are those where grains of different materials are mixed on a centimeter or finer scale such that scattered photons can interact with different minerals before reflecting back to the sensor (e.g., mineral crystals within a rock, sand, or soils). Areal (linear) mixtures are those where materials are mixed on a centimeter or coarser scale (e.g., alluvial fans covered by rocks with different mineral components, mixed vegetation, or patchy soil cover). Spectral dominance means that the diagnostic absorptions of that material are the strongest features in a given spectral region and are not obscured beyond recognition by absorptions from other phases.

In total, 274 reference materials were used for Tetracorder mineral mapping – not all were detected at Cuprite. Spectral comparisons included 140 material categories in the electronic region and 134 in the vibrational region. Categories include individual minerals, discrete members of mineral solid-solution series, areal and intimate mineral mixtures, and a few mineral grain-size series. Tetracorder outputs *fit*, *depth* (of diagnostic absorptions), and *fit*depth* images for each reference material (Clark et al., 2003). The *depth* of an absorption is calculated by dividing the reflectance of an absorption band's bottom by the reflectance at the same wavelength of a continuum (i.e., in this case a straight line) between the shoulders of the absorption (Clark and Roush, 1984). Doing the same for all channels in an absorption results in a normalized "continuum-removed" spectral feature. In each image, pixels are either turned on (successful identification) or off (no detection) with each illuminated pixel's brightness a direct measure of the calculated *fit*, *depth*, or *fit*depth* where the phase was detected. Because *fit*depth* images contain complimentary information (e.g., the degree of spectral fit and spectral

abundance derived from the depth of diagnostic absorptions), they were used to make color-coded maps of mineral abundance indicated by spectral signal.

Other minerals may be present in a pixel, but their spectral signatures are overwhelmed by stronger absorptions from spectrally dominant phases. Because the depth of a mineral's absorptions is a function of its grain size, absorption coefficient, and abundance, the spectrally dominant phase may not always be the most abundant (Clark and Roush, 1984). Non-hydrated quartz and most unaltered feldspars have at most only weak spectral features in the 0.4 - 2.5 μm region, hence neither were mapped using the AVIRIS data, even though they may be the most abundant minerals within a pixel. Accordingly, the resulting maps generated by this study present the spectrally dominant mineral in each pixel for the two spectral regions.

Spectral Map Verification

Four levels of verification were used to check the mineral maps: 1) comparison to published geologic maps and reports, 2) detailed field observations, 3) mineralogical analyses of field samples, and 4) comparison of retrieved AVIRIS spectra to library reference spectra of well-characterized minerals. Composite surface samples were collected over a 17 x 17 m AVIRIS-pixel-sized area from sites with high Tetracorder *fit*depth* values considered diagnostic for specific solid phases or mixtures of solid phases. At each site several rock fragments were gathered to assure representative samples of the targeted mineralogy were collected. Table A1 lists the Tetracorder mineral identification and laboratory analysis results for samples representative of 23 spectral categories collected from primary field verification sites. Sites representative of 13 additional categories were visually checked in the field in lieu of sample collection and laboratory analysis because they were composed of areal mixtures of phases already verified at the primary sites. Spectra for all 36 categories were retrieved from the AVIRIS data over these field verification sites and compared with matching reference mineral spectra. For each category, spectra of six adjoining AVIRIS pixels were averaged to increase the signal-to-noise ratio and show that these mineral signatures were consistent over relatively large areas (half the area of a football field). Large areas also facilitate comparison with future remote sensing datasets.

Other Analytical Techniques

Field and laboratory reflectance measurements were made with an ASD Inc. Fieldspec® Full Range Spectrometer over the wavelength range from 0.35 to 2.5 μm using the sun or a halogen lamp for illumination and Spectralon® panel for reference. These spectra were converted to absolute reflectance using a modified National Institute of Standards and Technology (NIST) traceable Spectralon® reflectance spectrum supplied with the Spectralon® panel by Labsphere, Inc. The ASD spectrometer has 5-nm spectral resolution from 0.35 to 1.0 μm and 11 nm spectral resolution from 1.0 to 2.5 μm. Wavelength positions are accurate to < 1 nm based on annual ASD, Inc. calibrations, and independently verified by us using measurements of well-characterized sharp spectral features in a Corning® REE-doped glass, a clear mylar sheet, and a NIST wavelength standard. Higher spectral resolution NIR reflectance spectra were measured relative to a stainless steel mirror on a Nicolet 780 Magna Spectrometer® equipped with a Spectrotech® reflectance attachment, KBr beam splitter, and cryogenically cooled MCTB and InSb detectors.

Electron probe microanalysis (EPMA), scanning electron microscopy (SEM), and X-ray fluorescence (XRF), and X-ray diffraction (XRD) analyses were used for supplemental phase identification. Quantitative elemental analyses of muscovite and illite field samples were obtained using a fully automated, five-wavelength spectrometer JEOL JXA 8900 Electron Microprobe® operated at 15 kV, 20 nA (cup), and a spot beam. Analytical precision for major and minor elements based on replicate analysis of standards was better than ± 2 percent relative concentration and equal to counting statistics for trace elements (< 3 wt%). X-ray peak intensity mapping of alunite samples was done at 15 kV, 30 nA (cup) current, using a spot beam. Typical map sizes were 500 by 500 pixels with a 0.5 micrometer pixel size and dwell time of 40 microseconds per pixel. SEM analyses of hydrated SiO_2 field samples was done on gold coated grains using a JEOL 5800LV® instrument. Energy dispersive X-ray analysis was performed using an Oxford ISIS EDS® system equipped with an ultra-thin-window detector. XRF analyses used a Philips PW1606 Simultaneous X-Ray Spectrometer® and lithium tetraborate flux (Taggart and Siems, 2002). For XRD analyses field samples were dry pulverized with a mortar and pestle to an average particle size of about 50 -150 μm. About one gram of each specimen was then packed in an aluminum sample holder and analyzed with a Scintag X-1 Automated Diffractometer® using copper (Cu) K-alpha radiation and fitted with a spinning sample holder.

Five mineral separates from four samples were analyzed by the $^{40}Ar/^{39}Ar$ age-spectrum method at the U.S. Geological Survey Argon Laboratory in Denver, Colorado using analytical procedures described by Snee (2002). Analytical data and details of the analyses for these samples are presented in Table A2. A K-Ar whole rock age of basalt sample CU93-313 was determined using the procedure outlined in Fleck et al. (1996) with analytical data listed in Swayze (1997).

Stable isotope samples were prepared using techniques developed by Wasserman et al. (1992). Isotopic $\delta^{34}S$ analyses were made using continuous flow mass spectrometry at the G.G. Hatch Isotope Laboratories at the University of Ottawa, Ontario. Hydrogen and oxygen isotope compositions were determined by continuous flow techniques through a TC/EA coupled to a ThermoFinnigan Delta XL Mass Spectrometer® similar to the methods of Sharp et al. (2001) at the U.S. Geological Survey Isotopic Laboratory in Denver, Colorado.

A geophysical survey of the subsurface structure and alteration at Cuprite involved collecting nine one-dimensional vertical Direct Current (DC) resistivity soundings along a 4 km-long east-west transect from the eastern margin of the western center across the pediment and eastern center halfway to Stonewall Playa (Fig. 3A). Each sounding used the Schlumberger array configuration, where four electrodes were placed along a nearly straight line (when possible) on the surface, with direct current from a portable 5 Kva generator introduced into the ground via two outlying electrodes A and B, and the electrical potential measured between two central electrodes M and N (Zhody et al., 1974). Each sounding was acquired in three segments. The first segment was measured by expanding the current-electrode spacing (AB/2) from 3.05 to 30.5 m with the potential-electrode spacing (MN/2) held constant at 0.61 m. The next two segments were made by expanding the current-electrode spacing from 30.5 to 305 m then from 305 m to 609 or 914 m (depending on topographic obstacles) with the potential-electrode spacing held constant at 6.1 m and then 61m respectively. The resulting sounding curves were corrected for non-linear geometry of the electrical array and then modeled to obtain interpreted vertical resistivity (ohm–m) versus depth profiles using the method described in Zhody (1989).

Imaging Spectroscopy

Mineral maps of the electronic and vibrational spectral regions were produced for the Cuprite area (Fig. 5). The most prominent features on these maps are the assemblage of minerals attributed to zones of hydrothermal alteration as distinguished from the surrounding alluvial fans. Tetracorder identified categories consisting of spectrally dominant single minerals (e.g., pyroxene, calcite, Na-montmorillonite, nontronite) and intimate mineral mixtures (e.g., chlorite+white mica, buddingtonite+Na-montmorillonite), mostly in hydrothermal zones or unaltered bedrock exposures, and areal (linear) mineral mixtures (e.g., kaolinite+white mica, calcite+white mica), mostly on alluvial fans (Fig. 6). Field samples were collected in areas corresponding to the AVIRIS spectral retrievals (Table A1). There is a strong similarity in shape between AVIRIS and laboratory spectral features (Fig. 6). For example, the AVIRIS spectrum retrieved from site 6E has a weak but still recognizable 1.0-μm absorption consistent with pyroxene when compared to the lab spectrum. The subdued signal is attributed to the nearly opaque desert varnish coating on rocks at this site.

Electronic Region

Electronic processes influence the reflectance spectra of minerals with transition metals (e.g., Fe, Ti, Mn, Cu, Ni, Co, Cr, and V), producing absorptions with shapes and wavelength positions that are in many cases diagnostic of their crystal structure (Hunt, 1977; Burns, 1993). Continuum removed AVIRIS and laboratory spectra show slight changes in the position and width of electronic transition absorptions from 0.4 to 1.3 μm in hematite, jarosite, and goethite, which can be used to spectrally differentiate among these minerals (Fig. 7). Relatively sharp absorptions due to kaolinite and alunite in the retrieved AVIRIS spectra near 1.4 and 2.2 μm can spectrally dominate the vibrational region, but these minerals have no significant electronic absorptions so do not interfere with identification of the coexisting Fe-minerals (Fig. 7B). Thus, differences in the shape, width, and wavelength position of the 1-μm region absorptions allow Tetracorder to differentiate between Fe-minerals and jarosite + goethite mixtures (Fig. 7C). Goethite and hematite have overlapping intense absorptions in the 0.3 to 0.45 μm region that are diagnostic though grain size variations strongly influence the intensity of absorption in this region. Jarosite and other similar Fe-sulfates have narrow diagnostic absorptions near 0.43 μm that are apparent when these mineral form thick coatings. Hematite, jarosite, and goethite have relatively weaker absorptions between 0.6 - 0.7 μm; however, these are located at the same wavelength as the intense chlorophyll absorption in plants. Tetracorder uses electronic absorptions in the 0.5- and 1-μm regions but not at 0.6-0.7 μm for identification of Fe-minerals to avoid potential confusion with plants (Clark et al., 2003).

Jarosite has a sharp vibrational absorption at 2.265 μm that appears infrequently at Cuprite because it is usually overwhelmed by much stronger kaolinite and alunite absorptions in neighboring rocks (see very weak 2.265-μm absorption marked by vertical tick under spectrum 1A in Fig. 7B). It is possible to identify jarosite remotely using the 2.265-μm absorption when it is intense enough, as was demonstrated terrestrially (Ong et al., 2003) and on Mars (Milliken et al., 2008; Farrand et al., 2009). In fact, subtle variations in the wavelength position and shape of vibrational absorptions near 1.4, 1.85, and 2.26 μm can be used to differentiate K- from Na-jarosite (Bishop and Murad, 2005; Basciano and Peterson, 2008; Swayze et al., 2008a) but there is no significant difference in the shape or wavelength position of the electronic absorptions between these endmembers. When fine-grained jarosite is exposed to rain or snow it usually

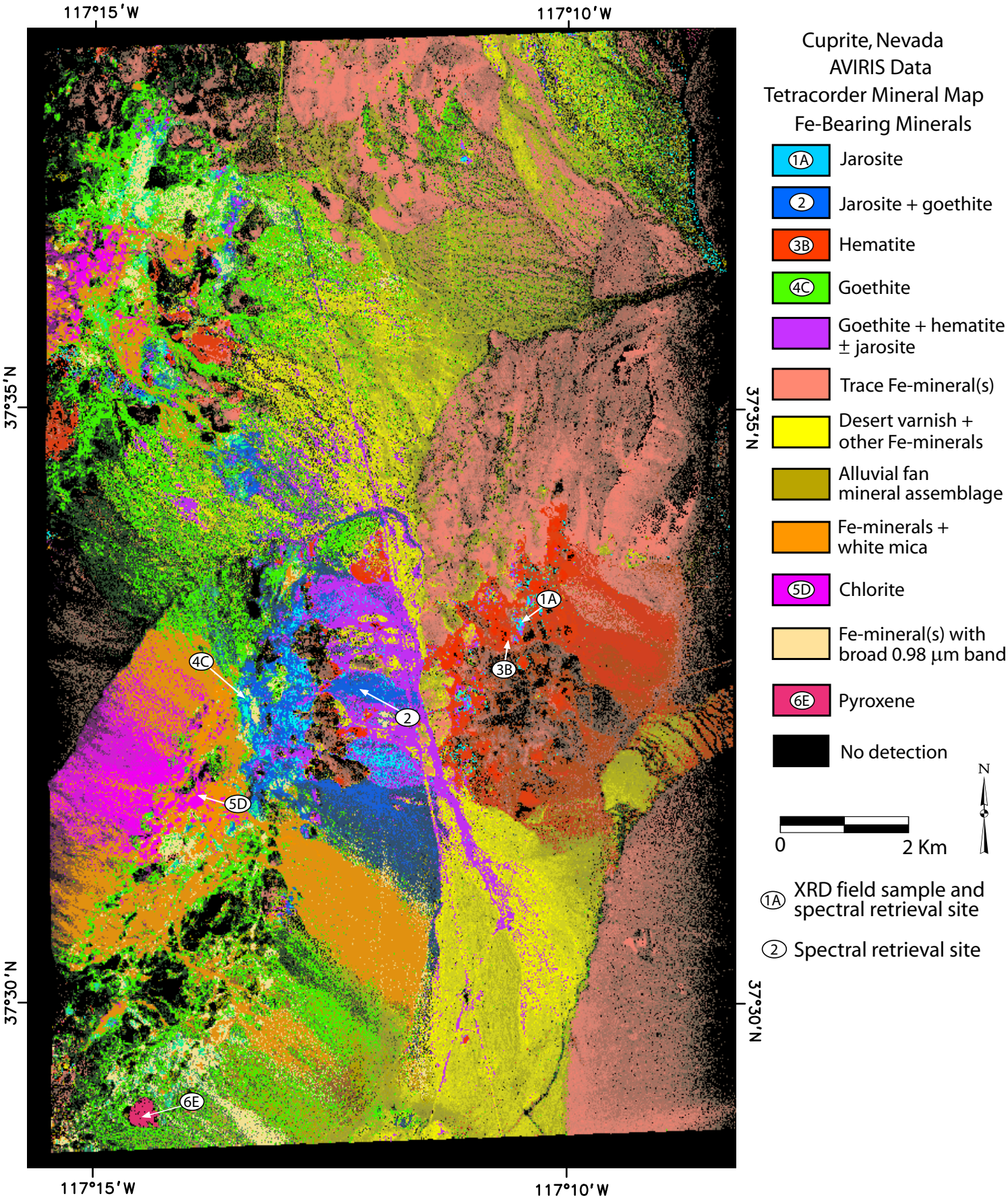

Fig. 5A. Tetracorder mineral map of the spectrally dominant Fe-bearing minerals at Cuprite using the 0.4 to 1.3 µm electronic absorption region of the AVIRIS data. Arrows mark locations of spectral retrieval sites. Number-letter combinations refer to spectral retrievals done at localities where samples were collected and analyzed (see Table A1). Projection is UTM zone 11 using NAD27 datum.

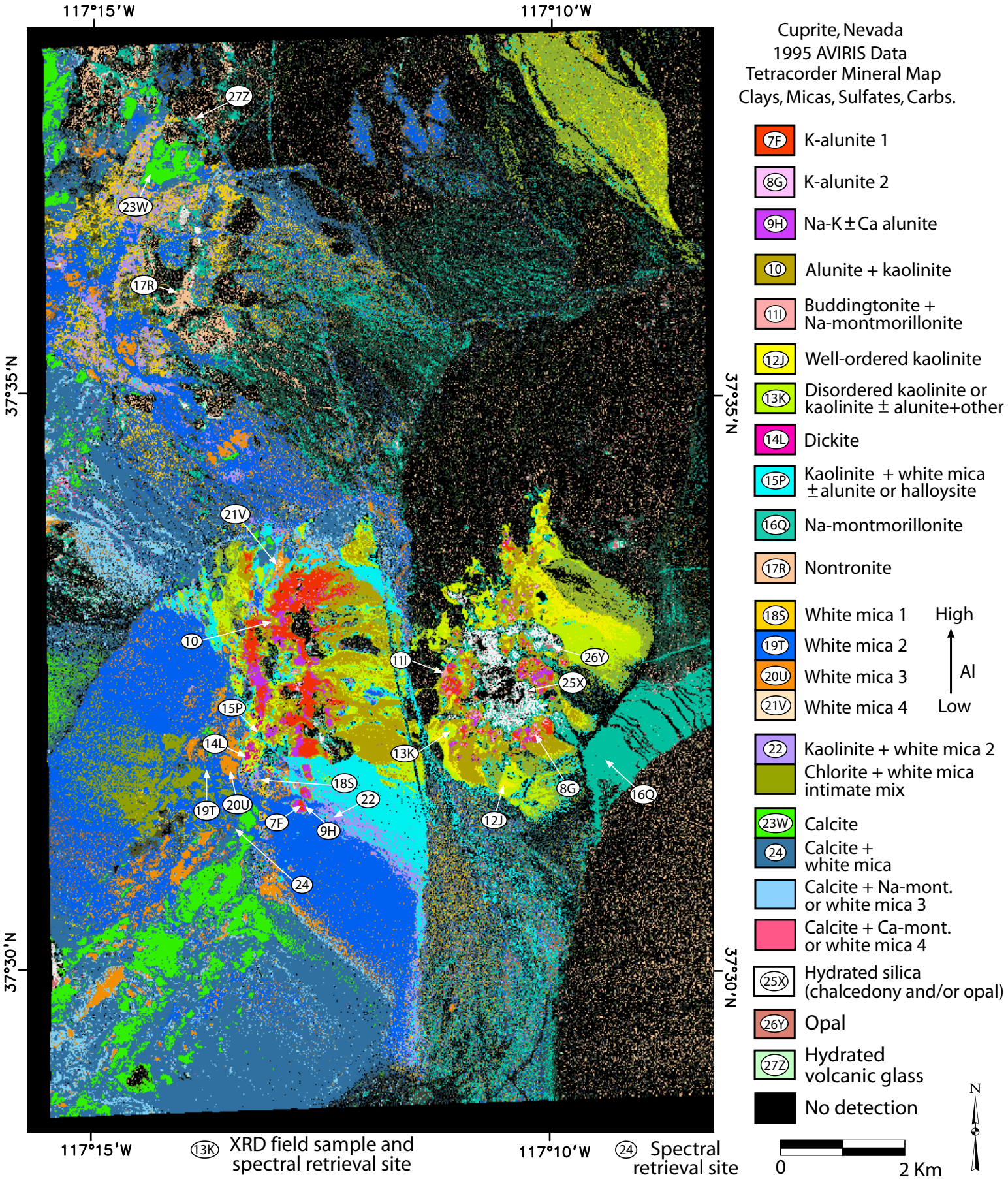

Fig. 5B. Mineral map of spectrally dominant clays, micas, sulfates, and carbonates at Cuprite using the 1.3 to 2.5 μm vibrational absorption region of the AVIRIS data. Arrows mark locations of spectral retrieval sites. Number-letter combinations refer to spectral retrievals done at localities where samples were collected and analyzed (see Table A1). Projection is UTM zone 11 using NAD27 datum.

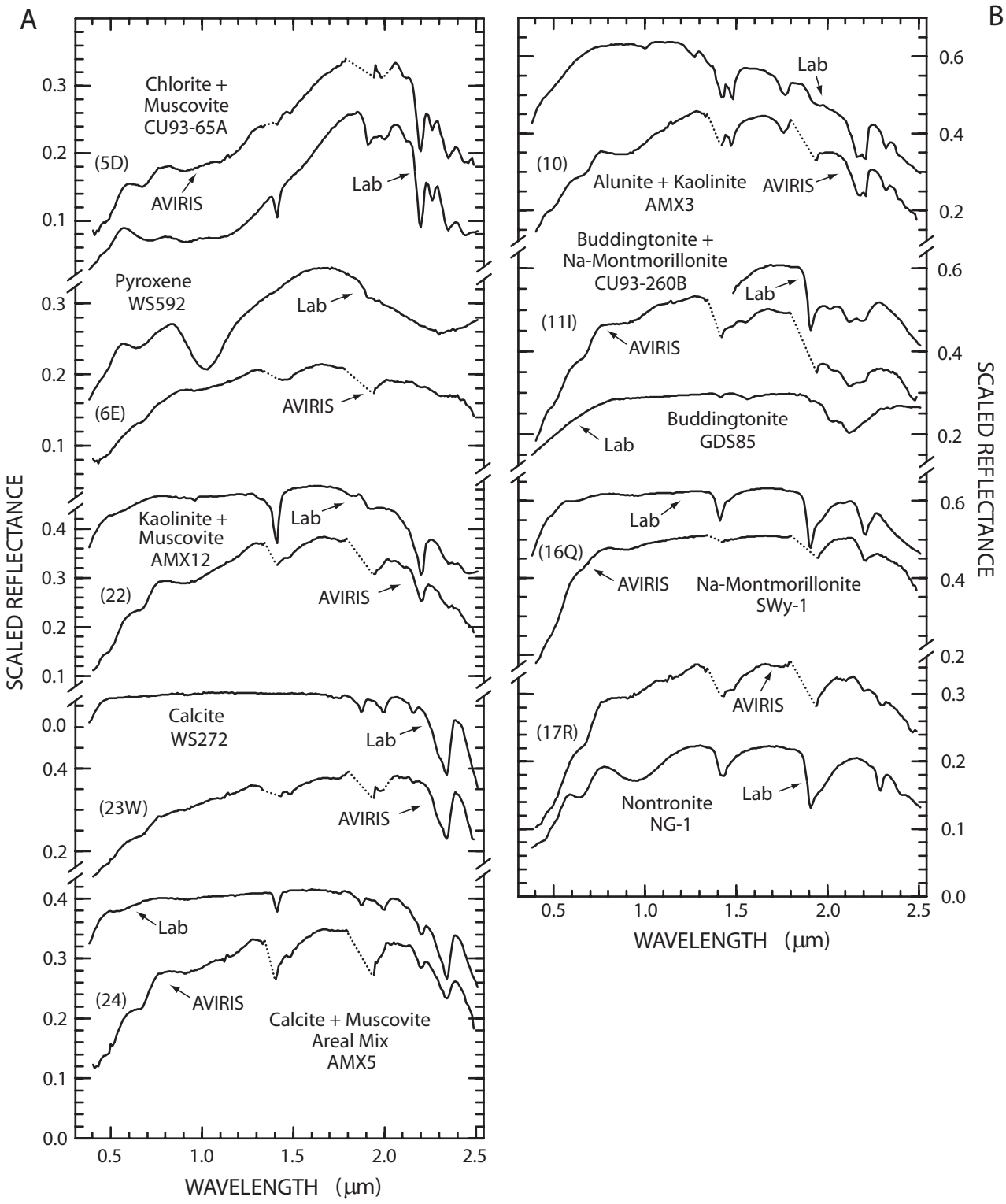

Fig. 6. Spectra retrieved from the AVIRIS data compared with laboratory reflectance spectra of well-characterized reference minerals (Clark et al., 2007) convolved to AVIRIS spectral resolution. Number and letter codes in parentheses (i.e., map codes 5D, 6E, 22, etc.) refer to spectral retrieval and sample collection locations shown on Figures 5A and B. Each AVIRIS spectrum is an average of the spectra from a cluster of six adjoining pixels. Regions of strong atmospheric absorptions (dotted lines) have been deleted in AVIRIS spectra. In many cases, the spectra retrieved from the AVIRIS data have absorption features from more than one mineral (e.g., absorptions in both the electronic and vibrational regions). AMX indicates reference spectrum is a constructed areal (linear) mixture.

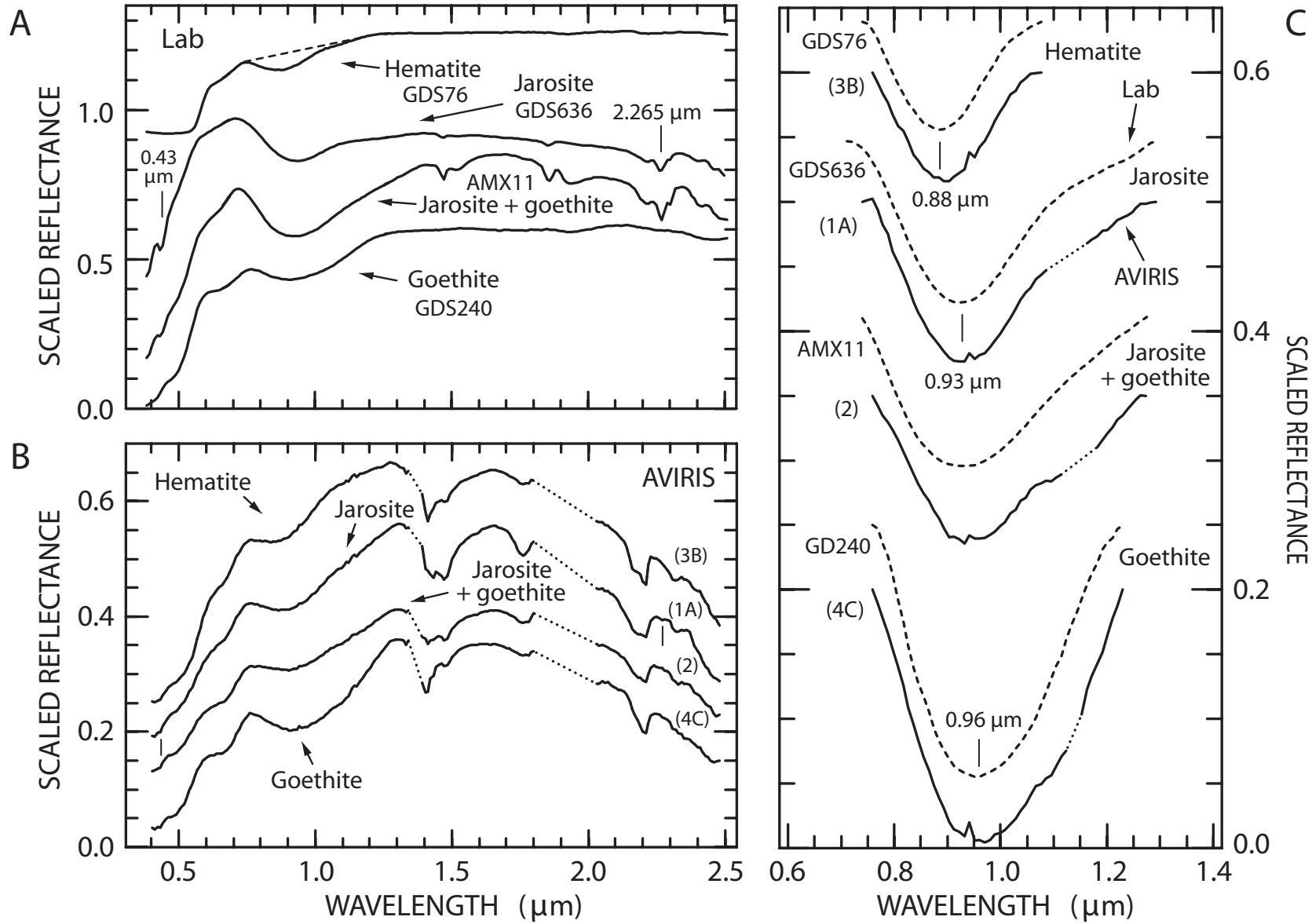

Fig. 7. A) Reflectance spectra of laboratory reference minerals hematite, jarosite, goethite, and a constructed areal (linear) mixture of jarosite and goethite. Equal parts hematite and goethite were each individually mixed with 98 weight percent quartz to unsaturate their electronic absorptions to better match spectra of field samples. The jarosite spectrum is of a thin film (~60 µm thick) to mimic a rock coating. Spectra convolved to AVIRIS resolution. B) Fe-bearing mineral spectra retrieved from the AVIRIS data. Alunite and kaolinite spectral features spectrally dominate the weaker jarosite 2.265-µm absorption even when they occur below thin jarosite coatings (remnant of jarosite 2.265-µm absorption marked by vertical line below spectrum 1A). Number and letter codes in parentheses refer to spectral retrieval sites shown on Figure 5A with corresponding field sample analyses listed in Table A1. Each spectrum is an average of spectra from six adjoining pixels. C) Comparison of continuum-removed electronic absorptions from laboratory reference minerals and AVIRIS data. Dashed line in (A) is the continuum used to normalize the hematite absorption feature shown in (C). Regions of atmospheric absorptions (dotted lines) have been deleted in AVIRIS spectra. All spectra offset vertically for clarity.

transforms to ferrihydrite and eventually to goethite when the pH of contact solutions are not kept acidic (pH < 3) by contact with sulfides and their weathering products (Bigham et al., 1992; Swayze et al., 2000). As a result, goethite commonly coats jarosite, but because these coatings are sometimes thin (< ~ 40 μm), they can be relatively transparent at wavelengths beyond 2 μm, thus allowing the 2.265-μm absorption from the underlying jarosite to show through. In this situation, the spectrally dominant mineralogy in the electronic region reflects the current pH conditions of the ground surface (Swayze et al., 2000). For this reason, the spectral detection of fine-grained jarosite at discrete sites at Cuprite, using its electronic absorptions is considered indicative of active oxidation of sulfides minerals near the ground surface that maintain a low pH.

The electronic absorption map (Fig. 5A) shows that each hydrothermal center is spectrally dominated by different Fe-minerals. The surface of the western center is characterized by extensive areas of jarosite and jarosite + goethite. Field investigation of areas that mapped as "Fe-mineral with broad 0.98-μm band" in the western center (just east of the arrow from "4C" in Fig. 5A and top center of Fig. A1) found that these areas are propylitically-altered (i.e., rocks contain chlorite, magnetite, and minor epidote) sandwiched between zones of advanced argillic alteration. The high magnetite content of these propylitic rocks lowers reflectance levels enough to obscure chlorite's strong Fe-electronic and vibrational absorptions. Areas mapped as "trace Fe-mineral(s)" along the eastern margin of the western center (Fig. A1) correspond to silicified (chalcedony-rich) rocks in the Harkless and Rabbit Springs Formations. Black lichen, desert varnish, and wind-blown dust containing trace levels of Fe-bearing minerals form coatings and thin discontinuous soils on these siliceous rocks that would otherwise be blank (show as black) on the 1-μm mineral map.

The eastern center is spatially dominated by hematite in altered volcanic rocks surrounding a Fe-mineral poor chalcedony/opal-rich siliceous zone (black areas just south of site 3B in Fig. 5A). The prevalence of hematite with only a few small patches of jarosite suggests that the eastern center has not yet eroded to expose more extensive sulfide and jarosite zones likely present beneath the surface (Swayze, 1997). The large central siliceous zone also mapped in places as "trace Fe-mineral(s)" based on the combined spectral signature of accumulated soil, lichen cover, and desert varnish (compare with same area in Fig. 5B).

Areas outside the hydrothermal centers are also characterized by the presence of Fe-minerals. A weak spectral signature of pyroxene was detected in a basalt dike 6 km southwest of the western center (site 6E in Fig. 5A; spectrum 6E in Fig. 6). Extensive exposures of the Stonewall Flat Tuff north of the eastern center and alluvium on the western slope of Stonewall Mountain (Figs. 2 and 5A) mapped as the trace Fe-mineral category because of weak Fe-absorptions that are attributed to widely dispersed hematite grains on weathered surfaces of the volcanic tuff. Harkless phyllite exposures south and north of the western center mapped as chlorite and muscovite with broad 1-μm bands (site 5D and surrounding area in Fig. 5A). Deeply weathered Mule Springs Limestone apparently contains goethite, whereas fresh exposures lack detectable Fe-minerals and are black on the 1-μm map (just north of site 6E in Fig. 5A). Desert vegetation covers up to 15 percent of the surface at Cuprite, interfering to some degree with Fe-mineral identification because of vegetation's relatively strong 1.18-μm H_2O absorption. As vegetation cover increases the certainty of Fe-mineral identification decreases, requiring generalized spectral map labels (e.g., "desert varnish + other Fe-minerals").

Vibrational Region

The vibrational absorption map (Figs. 5B and 8) shows that both centers have zones where alunite is spectrally dominant, and these grade laterally into zones dominated by kaolinite. In some areas the transition zone is partially concealed by alunite float (mapped as areal mixtures of alunite + kaolinite) shed from alunite-dominated topographically higher areas. The western center contains two N-S trending partially overlapping alunite zones separated by discontinuous lower-grade propylitic (labeled black areas on Fig. 8) and sericitic (cyan colored kaolinite + white mica) alteration. The western alunite zone grades southward into a ridge spectrally dominated by dickite. This locality is herein referred to as "Dickite Ridge" (Fig. 8). Likewise, the southern extension of the eastern alunite zone consists of three isolated hills, the southernmost of which is herein referred to as "Alunite Hill."

An extensive area of chalcedony and opal occupies the central part of the eastern center, which is in turn surrounded by concentrically-shaped zones of spectrally dominant alunite and kaolinite. The N–S trending structural grain evident in the western center is not as pronounced in the eastern center, but may be represented by two trends of altered rocks, which extend north and south from the center of alteration. The southern projection is informally called "Kaolinite Hill" (Fig. 8). Unlike the western center, no large areas (> 1 hectare) of white mica were detected in the eastern center.

White Mica Post and Noble (1993) documented a systematic shift in the wavelength position of vibrational absorptions in the 2.2-μm region of muscovite and illite reflectance spectra as a function of Al_2O_3 content. These absorptions are due to combinations of OH stretch and Al-, Fe-, and Mg-O-H bend vibrations arising from bonds in the octahedral sheets of these minerals (Rossman, 1984). Illite cannot be distinguished from muscovite in the 0.4 to 2.5 μm region at AVIRIS spectral resolution, so these minerals are grouped in the white mica spectral category (van Ruitenbeek et al., 2005). This category includes fine-grained muscovite that is commonly identified as sericite (Hurlbut and Klein, 1977).

Spectral measurements of the Post and Noble (1993) muscovite/illite compositional series show that the wavelength position of the 2.2-μm Al-OH combination absorption, arising from vibrations of the Al-OH-Al octahedral bonds, closely correlates with the abundance of Al in the octahedral layer (Al^{oct}) (Fig. 9). As Al^{oct} decreases due to substitution of Mg and/or Fe in the octahedral site, the 2.2-μm absorption shifts to longer wavelengths and weaker adsorptions attributed to Al-OH-Mg and/or Al-OH-Fe bonds develop as shoulders on the long wavelength side of the absorption. There is a strong correlation ($R^2 = 0.94$) between Al^{oct} content and wavelength position of the 2.2-μm absorption over a wide compositional range (Fig. 9B). A similar correlation exists for the position of the shoulder near 2.25 μm. Compositionally induced band shifts in muscovite and illite have been extensively modeled with *ab initio* quantum mechanical calculations (Sainz-Diaz et al., 2000; Martinez-Alonso et al., 2002). Martinez-Alonso et al. (2002) attribute the apparent Al-OH combination band shift to changes in the relative strengths of combination absorptions produced by Al-coordinated OH, due to OH located in different crystallographic sites of the unit cell, and to lack of perfect crystallinity, as observed by Saksena (1964). An alternative explanation for the shift may be the presence of multiple unresolved overlapping Al-OH absorptions that change strength (i.e., ones at shorter wavelengths get weaker while those at slightly longer wavelengths get stronger) as Si (Si^{Tet}) progressively substitutes for Al in nearby vibrationally-coupled tetrahedral sites. This is likely

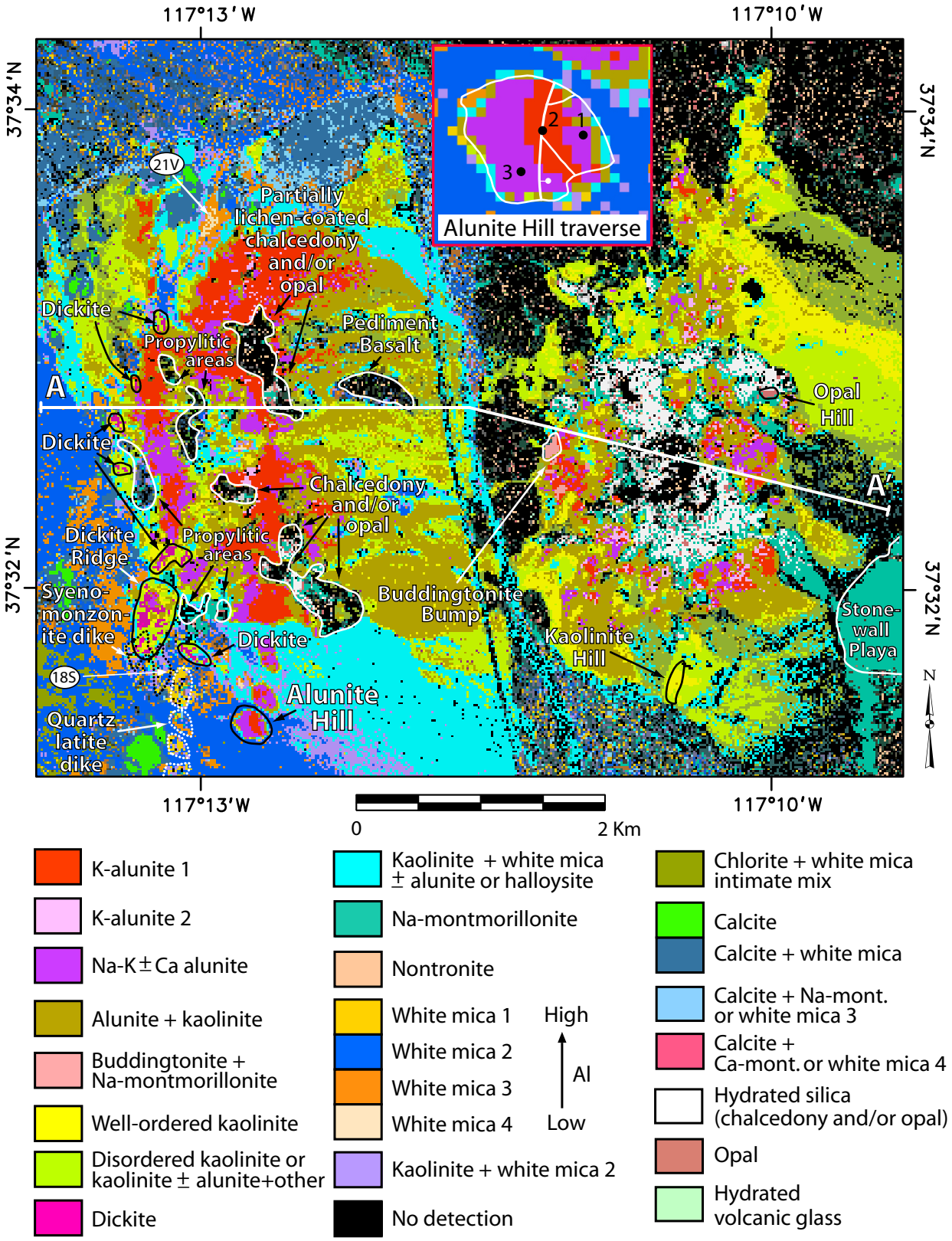

Fig. 8. Details of 2-µm vibrational region mineral map centered on the hydrothermal alteration at Cuprite. Inset shows sample collection locations for "Alunite Hill." Geologic contacts and fault information (from Ashley and Abrams, 1980) are shown in white on the inset image. Line labeled A --- A' shows position of cross section shown in Figure 23.

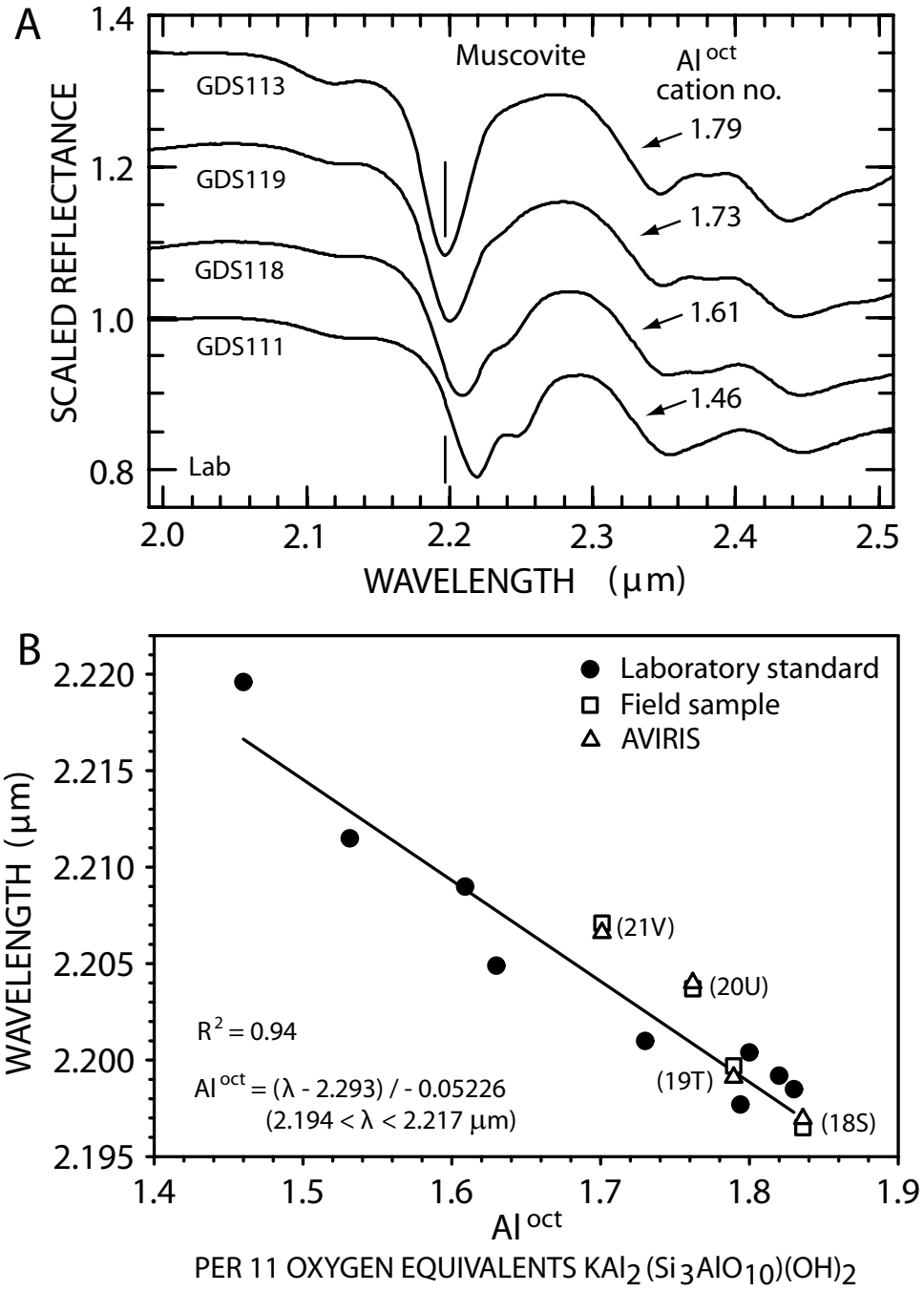

Fig. 9. A) High resolution reflectance spectra of muscovites showing band position as a function of Al in the octahedral site. Vertical reference lines mark the wavelength position of the Al-OH combination band in an Al-rich muscovite (GDS113). Spectra offset vertically for clarity. B) Wavelength position of the 2.2-µm Al-OH combination absorption as a function of octahedral Al content in white micas from lab standards, field samples, and AVIRIS data. R^2 is the square of the correlation coefficient calculated for the best-fit line to the laboratory standards (8 muscovites and one illite). In the best-fit equation λ is the wavelength of the 2.2-µm absorption in microns. Wavelength positions for all samples from continuum-removed laboratory reflectance spectra measured on a Nicolet FTIR Spectrometer® (lab standards) and ASD FR Spectrometer® (field samples). Cation formulae for octahedral Al (Al^{oct}) of lab standards from XRF measurements listed in Post and Borer (2002) for Empire Illite GDS121 and in Clark et al. (2007) for muscovites. Cation formulae of field samples based on microprobe measurements of 4 to 7 mineral grains in each sample. Number-letter code beside each field sample symbol refers to XRD analyses listed in Table A1 with collection locations shown in Figure 5B.

due to coupled substitution [Si^{tet} + (Mg, Fe^{2+})^{oct} = Al^{tet} + Al^{oct}] similar to that observed in high Al-phlogopite (Papin et al., 1997).

White micas identified by Tetracorder at Cuprite exhibit an Al-OH band between 2.195 and 2.210 μm, thus they have muscovite compositions and fall short of the phengite field as spectrally defined by Yang et al. (2011). There is a 2.2-μm-band shift in spectra of white micas retrieved from AVIRIS data over the western center (Fig. 10; sites 18S, 19T, 20U, and 21V in Fig. 5B). Their wavelength positions are nearly identical to those obtained from laboratory measurements of field samples collected from these sites (Fig. 9B), confirming that AVIRIS can match the accuracy of spectra taken using field spectrometers for determining white mica Al-compositions (see Table A1 for calculated Al^{oct} values).

The vibration region map shows that white micas with intermediate-Al compositions are most abundant in unaltered metamorphic rocks south of the western center (Fig. 8). Based on field observations, there is in places an abrupt 10 to 20 m wide transition from this intermediate-Al white mica (dark navy blue and orange pixels in Fig. 8) to kaolinite + white mica (cyan pixels), at the outer edge of areas affected by hydrothermal alteration in the western center. In several locations, most notably at the northern end of the western center (site 21V in Fig. 8), low Al white mica (tan pixels) grades laterally into more Al-rich mica (orange pixels) toward greater hydrothermal alteration. Leaching of Mg and Fe from micas by hydrothermal fluids may have increased the Al composition of pre-existing white mica or this could represent formation of Al-rich illite. A similar compositional trend is apparent in the vibrational mineral map of the quartz latite dike, which crops out between Dickite Ridge and Alunite Hill (Fig. 8). These intrusive rocks are altered to high-Al white mica (gold pixels) but are bordered on the east by intermediate-Al white mica bearing metamorphic rocks (dark navy blue and orange pixels). A sample of Harkless phyllite collected 60 m west of the dike, closer to alteration at Dickite Ridge, has an XRD pattern compatible with the presence of illite (site 18S in Fig. 8; analysis listed in Table A1), suggesting that hydrothermal fluids may have formed Al-rich illite. The N–S trend of the quartz latite dike and the distribution of the alteration zones suggest fractures controlled the localization of magma and subsequent hydrothermal fluid movement (Ashley and Abrams, 1980; Swayze, 1997).

A number of investigators have used spectrally measured muscovite composition to investigate metamorphic and hydrothermal rocks. Early Tetracorder mapping at Cuprite (Swayze et al., 1992) demonstrated that muscovite Al composition could be measured with imaging spectroscopy at the scale of an entire mining district. Spectroscopic field measurements of the 2.2-μm muscovite band positions were used to monitor the progress of exchange reactions associated with prograde metamorphism in the Black Hills of South Dakota (Duke, 1994), Precambrian basement rocks of Madagascar (Longhi et al., 2000), and Belt Supergroup rocks in Montana and Idaho (Duke and Lewis, 2010). In these studies, the 2.2-μm Al-OH absorption shifted to shorter wavelengths in the highest-grade rocks. AVIRIS measurements of the Al content of hydrothermal illite in the Comstock mining district are interpreted to vary with the acidity of hydrothermal fluids in discharge zones (Yang et al., 1999). Hydrothermal fluid pathways in the Panorama volcanic-hosted massive sulfide deposit in Western Australia were mapped using the 2.2-μm band position of white micas (Cudahy et al., 1999; van Ruitenbeek et al., 2005). Spectral measurements revealed longer wavelength band positions in hotter upwelling zones and shorter wavelength positions in cooler recharge zones. These studies showed that temperature, rock composition, and fluid chemistry were the primary factors

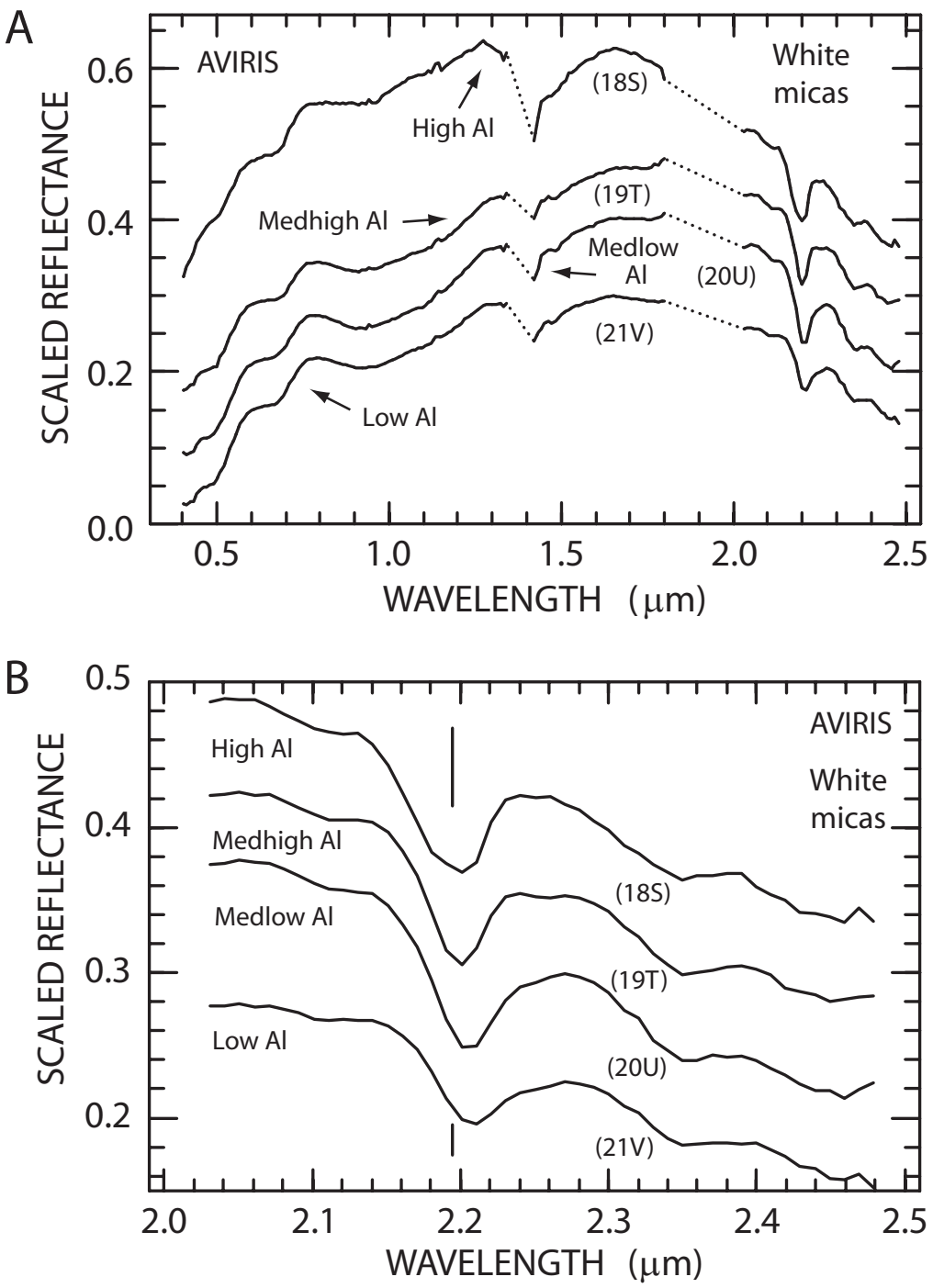

Fig. 10. A) Spectra of white-mica-bearing phyllites retrieved from the AVIRIS data. Number-letter codes in parentheses refer to spectral retrieval and sample collection locations shown on Figure 5B with sample mineralogy and compositions listed in Table A1, where Al-contents are assigned based on wavelength shift of the 2.2-μm absorption. Each spectrum is an average of spectra from six adjoining pixels. Spectra offset vertically for clarity. B) Same spectra as in (A) showing details of the 2-2.5 μm region. Note how the 2.2-μm absorption shifts to longer wavelengths in each successive spectrum. This shift is a direct indication of Al-composition (compare with Fig. 9A). Medhigh = medium high; medlow = medium low.

controlling white mica band positions in these two zones. In addition, spectral measurements of drill core from the Hellyer massive sulfide deposit in Tasmania revealed compositional variations in white mica where the 2.2-μm band shifts to longer wavelengths in hot discharge zones, intensely altered volcanic rocks, and zones of Pb-Zn mineralization (Yang et al., 2011). Illite crystallinity determined from XRD analysis correlated with the wavelength position of the 2.2-μm absorption in spectra of drill cores from the Pebble porphyry deposit in Alaska (Harraden et al., 2013). In this case, the absorption shifted to shorter wavelengths in the hottest rocks. In these examples, the apparent inconsistency in the position of the white mica 2.2-μm Al-OH band as a function of metamorphic grade and hydrothermal temperature suggests that rock and fluid composition may control white mica composition in altered rocks more than temperature or depth of burial.

Alunite The sulfate minerals alunite [$KAl_3(SO_4)_2(OH)_6$] and natroalunite [$NaAl_3(SO_4)_2(OH)_6$] are important components of advanced argillic alteration in low and high sulfidation deposits (Hedenquist et al., 2000). Their distribution and composition reflect the location and intensity of the parent hydrothermal conditions (Deyell and Dipple, 2005). Bishop and Murad (2005) studied the spectral characteristics of alunite and compiled detailed band assignments for vibrational features observed in the NIR region from earlier studies (Hunt et al., 1971; Hunt and Ashley, 1979). They attribute the intense doublet near 1.4 μm to OH overtone vibrations and the broad band near 2.17 μm to an Al-OH combination vibration.

Several spectral trends can be observed in NIR reflectance spectra of high temperature (450°C) synthetic alunites spanning the Na - K solid-solution series (Figs. 11A and B). The OH overtone doublet absorptions at 1.43 and 1.48 μm in the spectrum of K-alunite shift toward longer wavelengths as Na content increases. In the 2-μm region, the main absorption at 2.17 μm becomes narrower and the 2.21-μm shoulder on the long wavelength side of the main absorption shifts to longer wavelengths as Na content increases. Although subtle at AVIRIS spectral resolution, the 2.31-μm absorption also shifts to longer wavelengths as Na increases (Fig. 11B). These band shifts are likely caused by shortening of the hydrogen bonds and simultaneous lengthening of the hydroxyl bonds as SO_4 tetrahedral and Al-OH octahedral layers interpenetrate more in Na alunites because of this interlayer cation's smaller size. Sigmoid-shaped best-fit curves fit to the wavelength positions of the 1.48- and 2.21-μm absorptions and Na-content in synthetic and natural alunites show that the position of the 1.48-μm absorption shifts most with composition so it can be used to calculate the mole fraction of Na (X_{Na}) to ± 0.05 at 1nm spectral resolution (Figs 11C and D). At AVIRIS resolution, an accuracy of ± 0.10 X_{Na} is possible using the 1.48-μm absorption, which is comparatively free of spectral interference from coexisting phases that may affect accuracy when using the other absorptions.

Reflectance spectra of K- and Na-alunites synthesized at different temperatures (150 to 450°C; Stoffregen and Alpers, 1992) display OH-related vibrational absorptions that are narrower and more intense in higher temperature samples (Swayze, 1997). These spectral changes may be related to protonation of hydroxyls that charge-balance Al deficiencies present in disordered low-temperature synthetic alunites. Replacement by H_2O of one or more of the three hydroxyls, which are each hydrogen bonded to the apical sulfate oxygen, disrupts strong intralayer vibrational coupling, thereby weakening the spectral absorptions (Swayze et al., 2006). When these samples are heated, the protonated hydroxyls are liberated as "excess water," and subsequent recrystallization produces well-ordered stoichiometric crystals with intense spectral

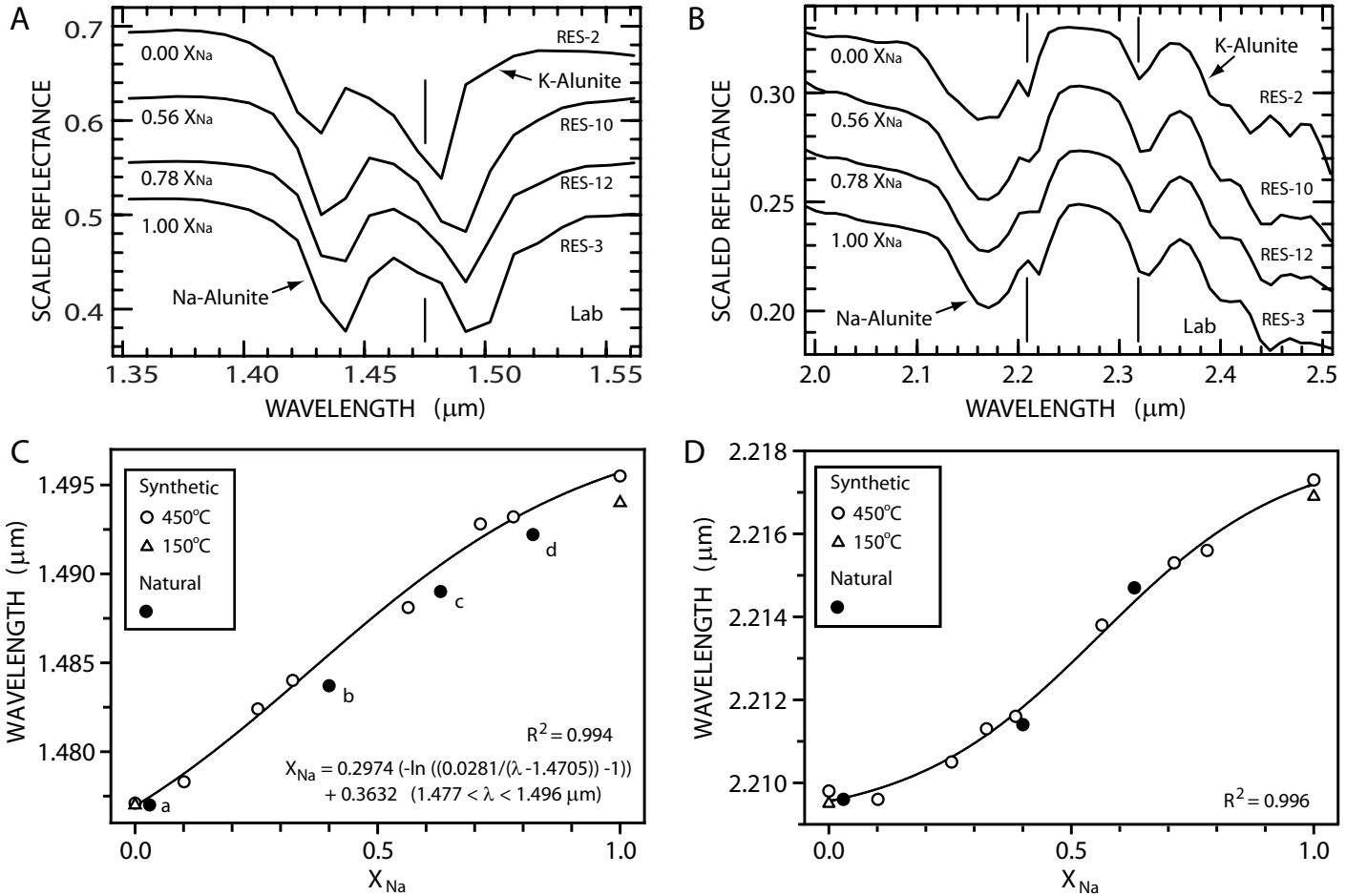

Fig. 11. A) Reflectance spectra of alunite Na-K solid-solution members synthesized at 450°C and convolved to AVIRIS resolution. X_{Na} is the mole fraction of Na in the alunite samples. Note how the doublet OH absorptions at 1.43 and 1.48 μm shift toward longer wavelengths as Na increases. Vertical reference lines mark position of 1.48-μm band in pure K-alunite. Spectra offset vertically for clarity. B) Same spectra as in (A) showing the 2.0 – 2.5 μm region. Note how the main 2.17-μm band narrows and how the 2.21 and 2.32-μm bands shift to longer wavelengths as Na content increases. (C) Wavelength positions of the 1.48-μm absorption as a function of X_{Na} in high and low temperature synthetic and natural alunites. R^2 is the square of the correlation coefficient calculated for the best-fit curve to the alunites. In the best-fit equation λ is the wavelength of the continuum-removed 1.48-μm absorption. Natural alunite samples: a = Marysvale, UT; b = Summitville, CO; c = Komatsuga, Japan; d = Sadler, TX. D) Same type of plot as in (C) but for the 2.21-μm absorption. Wavelength positions for all samples are from continuum-removed laboratory reflectance spectra measured on a Nicolet 760 FTIR Spectrometer® convolved to AVIRIS spectral resolution. Alunite compositions from Tables 1 and 2 in Stoffregen and Alpers (1992).

features that resemble those of natural high-temperature alunite (e.g., similar to what is seen in jarosite; Swayze et al., 2008a). Temperature-dependent spectral variations have been observed in 70 natural alunite samples formed at temperatures ranging from 20 to 400°C (Swayze et al., 2006). Spectral features of low temperature alunites formed in supergene, lacustrine, and speleogenic environments have weaker OH absorptions than those formed in higher temperature hydrothermal environments making it possible to recognize low temperature alunite from Martian orbit (Swayze et al., 2008b; Wray et al., 2011).

Most alunite identified by Tetracorder at Cuprite is K-rich with small-scattered areas of intimately mixed Na- and K-alunite (Fig. 8). Some alunite in the eastern center (i.e., spectral category K-alunite 2) has narrower and less intense spectral features than alunite exposed in the western center (i.e., K-alunite 1). Electron microprobe elemental maps (Fig. 12A) of sample CU91-217H collected from one of the Na-K±Ca alunite zones exposed on Alunite Hill (from site 1 on inset image in Fig. 8) show alunite crystals with Na-rich cores surrounded by rims of huangite (Ca analogue of alunite) in turn surrounded by K-rich alunite matrix. Another sample (CU93-322C from site 3) has alunite grains with Na-rich cores surrounded by thin K-rich rims. The K- and Na-alunite components have endmember compositions based on the positions of their OH overtone absorptions (based on downward projection of vertical lines from synthetic endmembers in Fig. 12B). A spectrum of a natural alunite sample from Tambo, Chile (Deyell et al., 2005) has OH absorptions indicative of huangite in addition to those from Na and K alunite, which can also be seen in the spectrum of CU91-217H. Huangite has diagnostic OH overtone absorptions at 1.371, 1.448, 1.457, and 1.511 μm (middle spectra of Figs. 12B and C) and combination absorptions at 2.193, 2.241, and 2.371 μm (middle spectra of Fig. 12D). At AVIRIS spectral resolution many of these absorptions are too weak or overlap with neighboring absorptions too much for detection at low concentrations (Figs. 12C and D). Huangite's potentially diagnostic 1.37-μm absorption is usually obscured by atmospheric H_2O in terrestrial remote sensing data (dotted spectral region in Fig. 12C), however, its 2.37-μm absorption can be used for identification because it is located at a wavelength clear of strong atmospheric absorptions and absorptions from K- and Na-alunite (Fig. 12D). Huangite absorption wavelengths are shifted from those of K- and Na-alunite, therefore a Ca component will not interfere with the determination of the Na/K cation ratio, given adequate spectral resolution and signal-to-noise ratio.

Tetracorder was able to differentiate intimate K- and Na-alunite endmember mixtures from areas dominated by K-alunite based on subtle differences in the shapes and positions of the 1.48- and 2.17-μm absorptions (Fig. 13). None of the retrieved AVIRIS spectra displayed a 2.37-μm absorption (i.e., nothing similar to the absorption seen in the spectrum of CU91-217H in Fig. 13B), indicating that huangite may not be a volumetrically significant component of alunite exposed at Cuprite.

No alunites with intermediate composition ($0.20 < X_{Na} < 0.8$) were identified in field samples collected at Cuprite. Stoffregen and Cygan (1990) suggest that the K-Na alunite system may contain a miscibility gap at low temperatures, similar to the one in the $CaCO_3$-$MgCO_3$ system. A few alunites with intermediate composition (i.e., two central black dots in Fig. 11C) were spectrally identified (Swayze et al., 2006) among more numerous endmember and near-endmember alunites from well-studied magmatic-steam and magmatic hydrothermal environments (Rye et al., 1992; Stoffregen and Alpers, 1992). Theoretically, alunites with intermediate composition only form at relatively high temperatures above the miscibility gap,

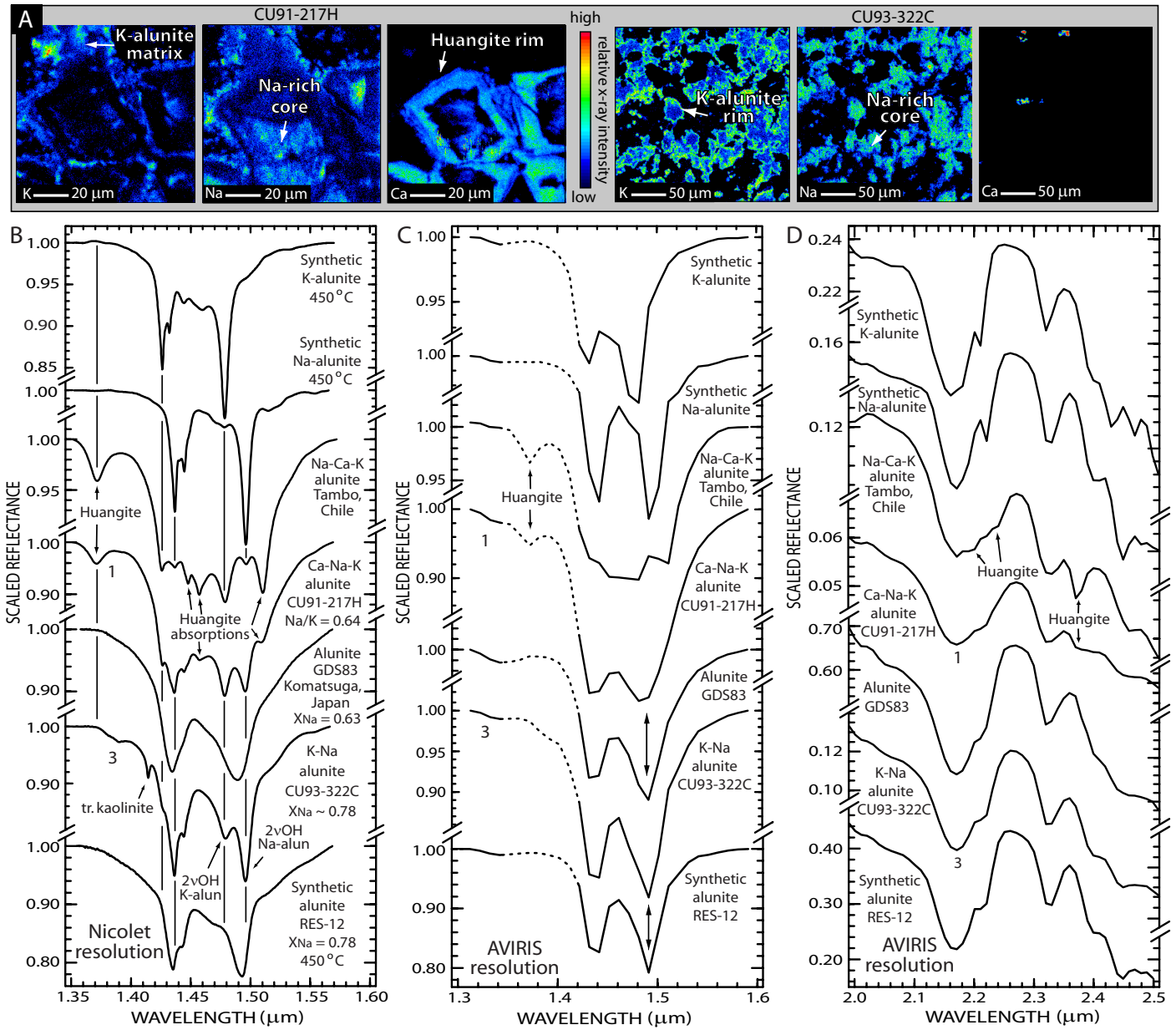

Fig. 12. A) Electron microprobe elemental maps for samples collected from the Na-K ± Ca alunite zones of Alunite Hill. Vertical color bar shows relative X-ray count levels for elements. B) Continuum removed high-resolution (4 cm^{-1}) reflectance spectra of samples collected from Alunite Hill with natural and synthetic intermediate, K-, and Na-alunite endmember spectra for reference in the 1.4-µm region. Numbers to left of spectra from Alunite Hill samples refer to collection locations shown in Figure 8 inset image. Vertical reference lines mark wavelength positions of main OH overtone absorptions in K- and Na-endmember alunites and the 1.37-µm absorption in huangite. X_{Na} is the mole fraction of Na in the alunites; Na/K = Na/K cation ratio. $2\nu_{OH}$ K-alun = first overtone of the OH stretch in K-alunite; likewise for $2\nu_{OH}$ Na-alun. C) Same spectra shown in (B) convolved to AVIRIS spectral resolution. Dotted portions of these spectra are obscured in AVIRIS data by strong atmospheric H_2O absorptions. D) Details of the 2-µm region Al-OH combination absorptions for samples shown in (B) convolved to AVIRIS spectral resolution.

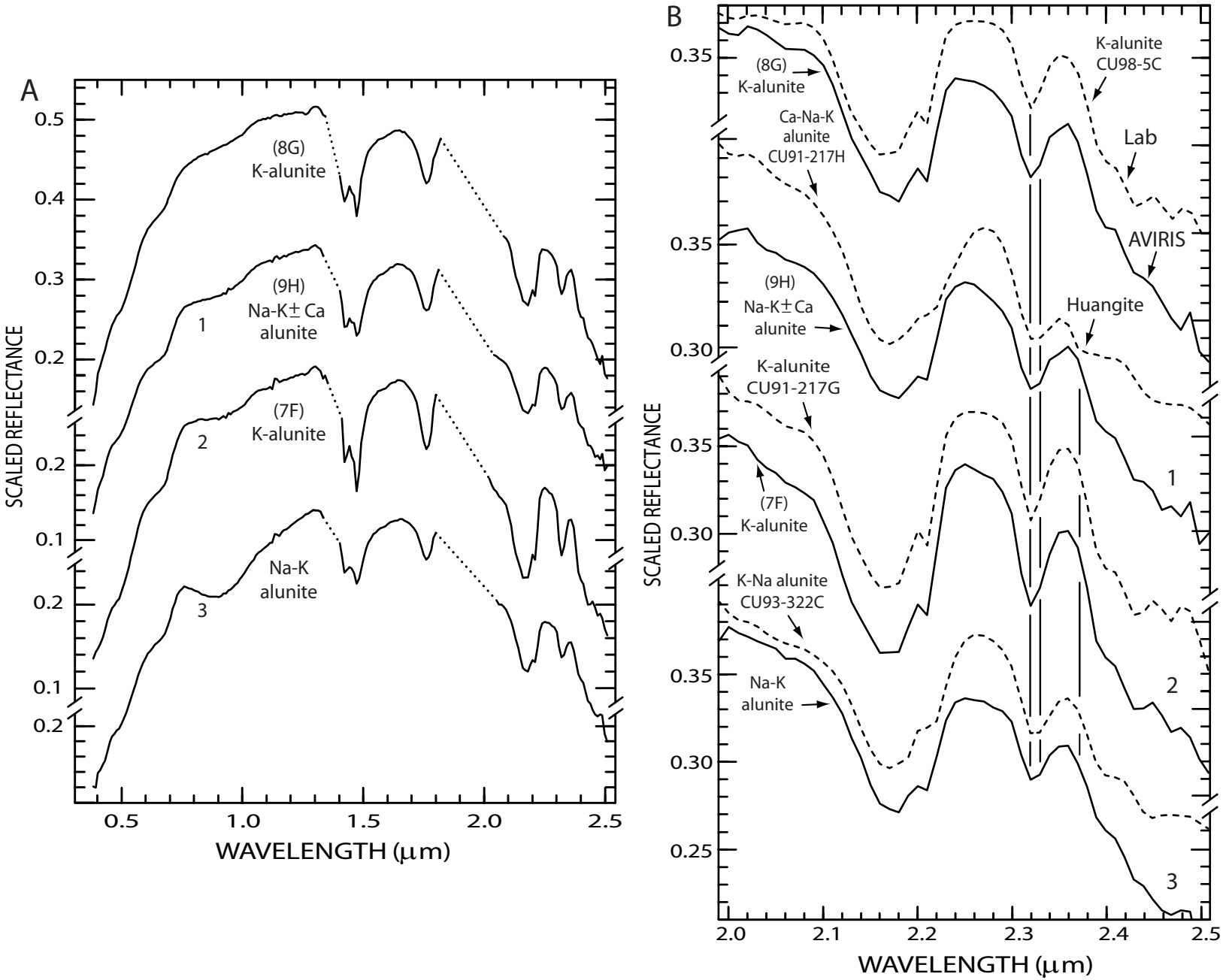

Fig. 13. A) Spectra of alunite-bearing rocks retrieved from AVIRIS data. Number-letter codes in parentheses and numbers to left of spectra refer to spectral retrieval and sample collection locations shown in Figure 5B and Figure 8 inset image respectively. Each spectrum is an average of the spectra from six adjoining pixels. Regions of strong atmospheric absorption (dotted lines) have been deleted. B) Same spectra as in (A) showing details of the 2-μm region compared with lab spectra of samples collected from these locations convolved to AVIRIS spectral resolution (dashed lines). Spectra offset vertically for clarity. See Table A1 for X-ray fluorescence (XRF) analyses of the field samples. Double vertical lines mark compositionally driven shift of the alunite 2.32-μm absorption. Single vertical line marks position of the 2.37-μm huangite absorption.

thus if detected remotely they may indicate a large magmatic vapor/fluid component during alteration.

Recognition of alunites with intermediate composition may be a challenge with most imaging spectrometers. For example, high-resolution spectra of a natural intimate mixture of K- and Na-alunite endmembers (CU93-322C) and a high temperature synthetic intermediate alunite (RES-12) with the same Na mole fractions (bottom two spectra in Fig. 12B), have obvious spectral differences, but are too similar at AVIRIS resolution (Figs. 12C and D) for Tetracorder to reliably differentiate. These samples are closer to the Na-endmember composition (X_{Na}= 0.78) so in the intimate mixture (CU93-322C in Fig. 12B), the K-alunite 1.48-μm OH overtone absorption only forms a shoulder on the stronger Na-alunite 1.495-μm OH overtone absorption. At AVIRIS resolution this creates a band that resembles a slightly wider intermediate Na-alunite OH absorption (compare the spectrum of CU93-322C with the spectrum below it in Fig. 12C). Consequently, intermediate alunites with near-endmember compositions will be the most difficult to spectrally differentiate from intimate mixtures of endmembers. In contrast, intimate mixtures composed of nearly equal amounts of K- and Na-endmembers will have an unresolved, broad-bottomed, OH overtone centered near 1.49 μm at AVIRIS resolution (e.g., spectrum of CU91-217H in Fig. 12C), so should be easier to spectrally differentiate from true intermediate composition alunites, which have narrower OH absorptions (e.g., spectrum of GDS83 in Fig. 12C).

Based on modeling, Deyell and Dipple (2005) have noted that at lower temperatures, small changes in fluid composition allow precipitation of both K- and Na-rich alunites, whereas at higher temperatures much larger changes in fluid composition are required to precipitate both near-endmember compositions, assuming near-equilibrium conditions. If their model is applicable to alteration at Cuprite, and barring major fluctuations in fluid composition, then the presence of endmember K- and Na-alunite compositionally zoned crystals at Alunite Hill may indicate areas of relatively lower temperature compared to the K-alunite rich band of rock they enclose (see inset image in Fig. 8). In fact, other areas of intimately mixed alunite endmembers tend to occur on the margins of larger K-alunite rich areas throughout the western center. Although Na-alunite formation is favored at higher temperatures given similar host rock type (Stoffregen and Cygan, 1990; Stoffregen and Alpers, 1992; Hedenquist et al., 1994; Chang et al., 2011), Deyell and Dipple (2005) suggest that initial host rock composition may influence the ultimate alunite composition.

Kaolin Group Minerals As may be apparent from discussion above, crystallographic disorder can significantly influence the shape of a mineral's spectral features (Hunt and Salisbury, 1970). This is evident for kaolin group minerals, three of which, including the hydrated variety, halloysite [$Al_2Si_2O_5(OH)_4 \bullet 2H_2O$], were found at Cuprite. Spectra retrieved from AVIRIS data (sites 12J, 13K, 14L, and 15P in Fig. 5B) compare favorably with reflectance spectra of dickite, well-ordered and disordered kaolinite, and halloysite (Fig. 14). Kaolinite and dickite have four distinct hydroxyl groups, three of which form (inner surface) hydrogen bonds across the interlayer region, nearly perpendicular to the crystallographic *c*-axis, with apical oxygens of neighboring silica tetrahedra. The fourth (inner) hydroxyl group lies within the basal plane of the crystals (Farmer, 1964). Halloysite (10Å) differs from these minerals by having interlayer H_2O and a curved-layer morphology (Joussein et al., 2005).

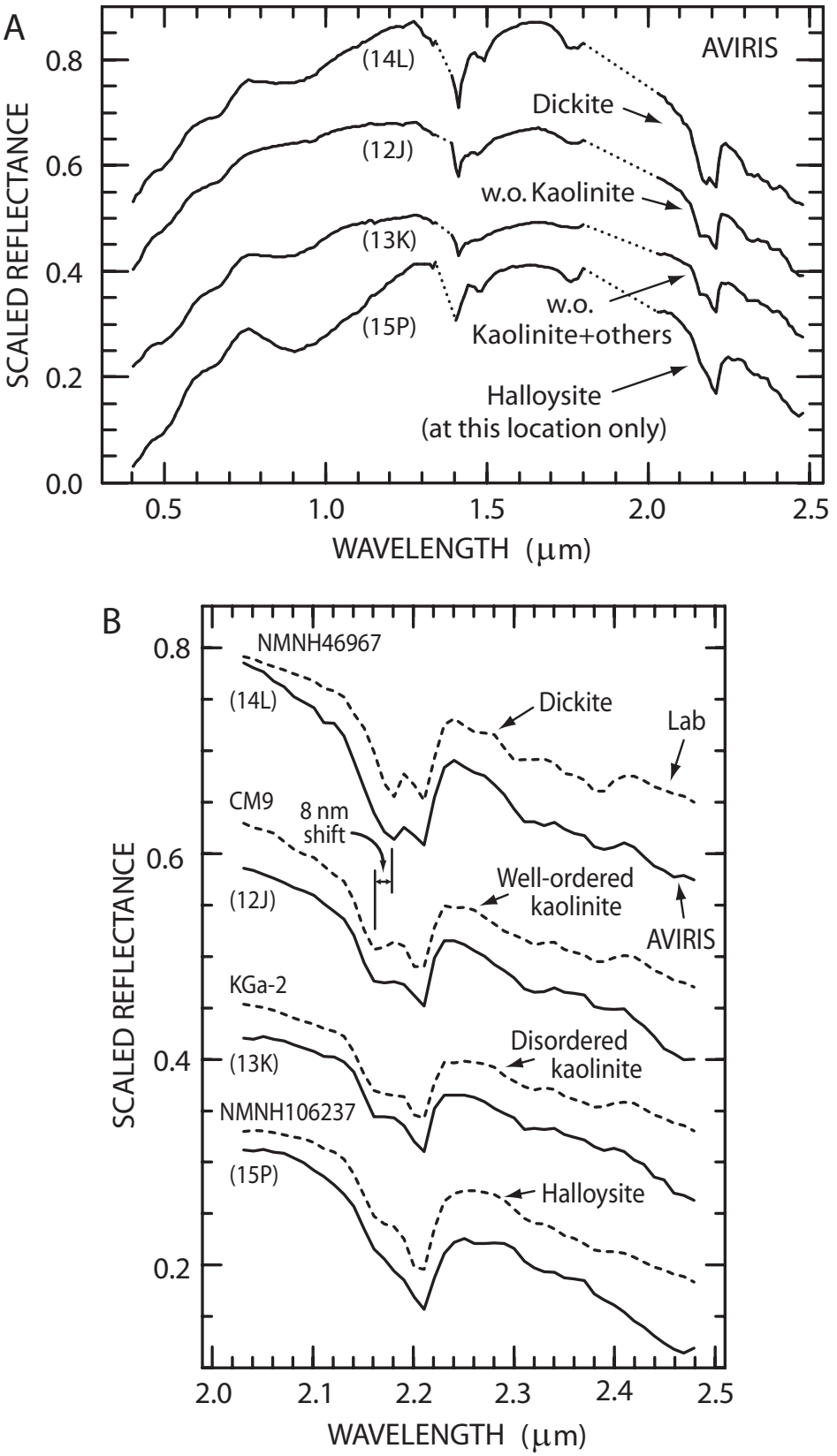

Fig. 14. A) Spectra of kaolin group minerals retrieved from AVIRIS data. Number-letter codes in parentheses refer to spectral retrieval and sample collection locations shown in Figure 5B and analyses listed in Table A1. Regions of strong atmospheric absorption (dotted) have been deleted. B) Same spectra as in (A) compared with kaolin group reference spectra convolved to AVIRIS resolution (dashed lines), showing details of the 2 - 2.5 μm region. The increased sharpness of the 2.21-μm absorptions in the AVIRIS spectra relative to reference spectra is due to contamination from trace levels of white mica or wind-blown smectite (see Table A1). All spectra are offset vertically for clarity. Vertical lines show the first band of the dickite doublet is shifted 8 nm toward longer wavelengths relative to those in the other kaolin group minerals. w.o. = well ordered.

These hydroxyl groups produce several sharp stretch fundamentals in the 2.7-μm region (Farmer, 1964), and accompanying stretch overtone and stretch-bend combination bands at 1.4 and 2.2 μm respectively (Hunt and Salisbury, 1970). Clark et al. (1990) observed a systematic decrease in the depth of the 2.16-μm band, the shorter wavelength band of the characteristic doublet combination absorption, from well-ordered kaolinite, through disordered kaolinite, to halloysite (lower three dashed spectra in Fig. 14B). Crowley and Vergo (1988) found that disordered kaolinite spectral features in the NIR resemble those of intimate mixtures of well-ordered kaolinite and dickite. Recent interpretations attribute structural disorder in kaolin group minerals to octahedral vacancy positional defects, interlayer translation defects, and modification of these interlayer translations by random shifts (Reynolds and Bish, 2002, and references therein).

Balan et al. (2001, 2005) summarize evidence from *ab initio* calculations for intra- and inter-layer coupling between vibrations of different hydroxyl groups in kaolin group minerals. Absorptions at 1.41 and 2.21 μm (longer wavelength bands of the doublet features in those regions) are due to the inner OH vibrations and their intensities are relatively unaffected by structural disruption of intralayer coupling. This is not the case for the shorter wavelength bands in the overtone and combination doublets. Apparently, nacrite- and dickite-like domains, in crystal stacking sequences of disordered kaolinite, offset octahedral Al-vacancies between adjacent sheets, locally modifying the orientation of inner surface OH bonds (Fialips et al., 2000; Johnston et al., 2008; Kogure et al., 2010). This disrupts intralayer vibrational coupling (Cruz-Cumplido et al., 1982) producing weaker than normal 1.39- and 2.16-μm absorptions.

At cryogenic temperatures (< 30K) disordered kaolinite displays discrete weak absorptions at wavelengths characteristic of cooled nacrite (another kaolinite polymorph) and dickite (Johnston et al., 2008). At room temperature these weak absorptions are obscured by stronger overlapping kaolinite absorptions. For disordered kaolinite, the lack of such intralayer vibrational coupling simultaneously weakens overlapping 2.16-μm kaolinite and 2.18-μm dickite-like absorptions, creating a shoulder where a separate absorption normally exists in well-ordered kaolinite (compare top three dashed spectra in Fig. 14B). For this reason, intimate mixtures of well-ordered kaolinite and dickite only roughly mimic details of the 1.4- and 2.2-μm spectral features of disordered kaolinite, because these mixtures consist of individual grains of each phase with full strength vibrationally-coupled absorptions. Acute disruption of intralayer coupling of inner surface OH vibrations is suggested in halloysite by its even weaker 2.16-μm band, which persists even after most interlayer H_2O is removed (lowermost dashed spectrum in Fig. 14B), and may be a consequence of its curved layer morphology. Bookin et al. (1989) concluded that a halloysite-like crystal structure should be the endmember of *b*-axis translational defect-type kaolinite.

It appears that XRD measurements of kaolinite disorder can be sensitive to natural abrasion (e.g., potentially from erosion) and grinding during lab preparation. However, octahedral vacancy positional defects should not be modified by physical treatment of a sample (Reynolds and Bish, 2002). This suggests that spectral determination of crystalline disorder in kaolinite should reflect its original state of order, as octahedral vacancy positional defects control the degree of intralayer vibrational coupling, and hence ultimately control the shapes of inner surface OH absorptions by which spectral disorder is gauged.

Fialips et al. (2000) found that the level of kaolinite disorder increased as the pH of synthesis fluids increased over the range from 0.5 to 14, but they found little influence from synthesis

temperature over the range from 200 to 240°C. They attribute kaolinite disorder to "poisoning" of crystal face growth caused by increased adsorption of impurities (e.g., Na, Fe, and Li) at higher pH. This suggests that in acidic hydrothermal systems one should expect well-ordered kaolinites. These lab observations are supported by XRD and spectroscopic measurements of disorder in naturally occurring kaolinites, where the highest degree of ordering was found in hydrothermal and sedimentary samples and most disorder was found in samples formed by weathering (Madejova et al., 1997). In theory, one can use this relationship to determine the local pH environment of kaolinite formation either on the Earth, Mars, or other planetary bodies using airborne or orbital imaging spectroscopy data.

Changes in the depth of the 2.16-μm band are evident in AVIRIS spectra collected at Cuprite (solid line spectra in Fig. 14B), indicating that the degree of crystallographic order in kaolin group minerals can be mapped remotely (Clark et al., 2003). Well-ordered kaolinite is relatively less abundant in the western center compared to the eastern center because of more extensive alunite and the occurrence of dickite (Fig. 8). AVIRIS spectra have a white mica/smectite component that sharpens the 2.21-μm band of the absorption doublet (see spectral and XRD data in Table A1). Previous studies have shown that areal mixtures of well-ordered kaolinite and wind-blown soil containing trace levels of white mica or montmorillonite can mimic the spectral shape of disordered kaolinite and may account for most of what Tetracorder initially mapped as disordered kaolinite (Clark et al., 2003; Swayze et al., 2003). We were unable to verify the presence of disordered kaolinite in samples collected from areas that mapped as disordered kaolinite (see analysis for sample CU00-19A from site 13K in Table A1). The presence of halloysite was verified by XRD analysis of a glycolated sample collected from site 15P, however, it is rare at Cuprite, with well-ordered kaolinite + white mica mixtures mimicking its broad spectral signature in most areas. Tetracorder did not detect dickite in the eastern center; however, it did find dickite at seven locations along the western margin of the western center, with the largest areas exposed at Dickite Ridge (Fig. 8). X-ray diffraction analysis indicates it occurs with kaolinite at sample collection site 14L (Fig. 5B). In active hydrothermal systems, kaolinite occurs from ambient temperatures up to 120°C; dickite ± kaolinite occurs from 120 to 200°C, and dickite from 150 to 270°C (Reyes, 1991; Zotov et al., 1998). The presence of dickite in the western center is consistent with overall higher temperatures and greater depth of burial.

Hydrated Silica Si-OH (silanol) related absorptions of opal and chalcedony are wider than those of weathered hydrated volcanic glass in the 0.9 to 2.5 μm region (Fig. 15). Langer and Flörke (1974) identified two types of silanol and water responsible for NIR vibrational spectral features in opal, which is composed of fairly regularly submicron-sized, closely packed silica spheres. A silanol group with weaker hydrogen bonding creates a sharp intense combination absorption at 2.21 μm while a silanol group with stronger hydrogen bonding results in a broader less intense combination absorption at 2.26 μm, both of which overlap to create a broad asymmetric absorption feature and are due to Si-OH bend plus OH stretch combination vibrations. The same relationship holds for two OH stretch overtone bands at 1.41 and 1.46 μm, though this last absorption is weaker in amorphous opal-A_N (Fig 15A) than other types of opal with more water. Weakly hydrogen-bonded water exists as isolated molecules in cage-like structures and more strongly bonded liquid-like water in films on sphere surfaces (Langer and Flörke, 1974), both giving intense but separate H-O-H bend plus OH stretch combination bands near 1.9 μm. Chalcedony consists of nanoscale intergrowths of quartz and a silica polymorph

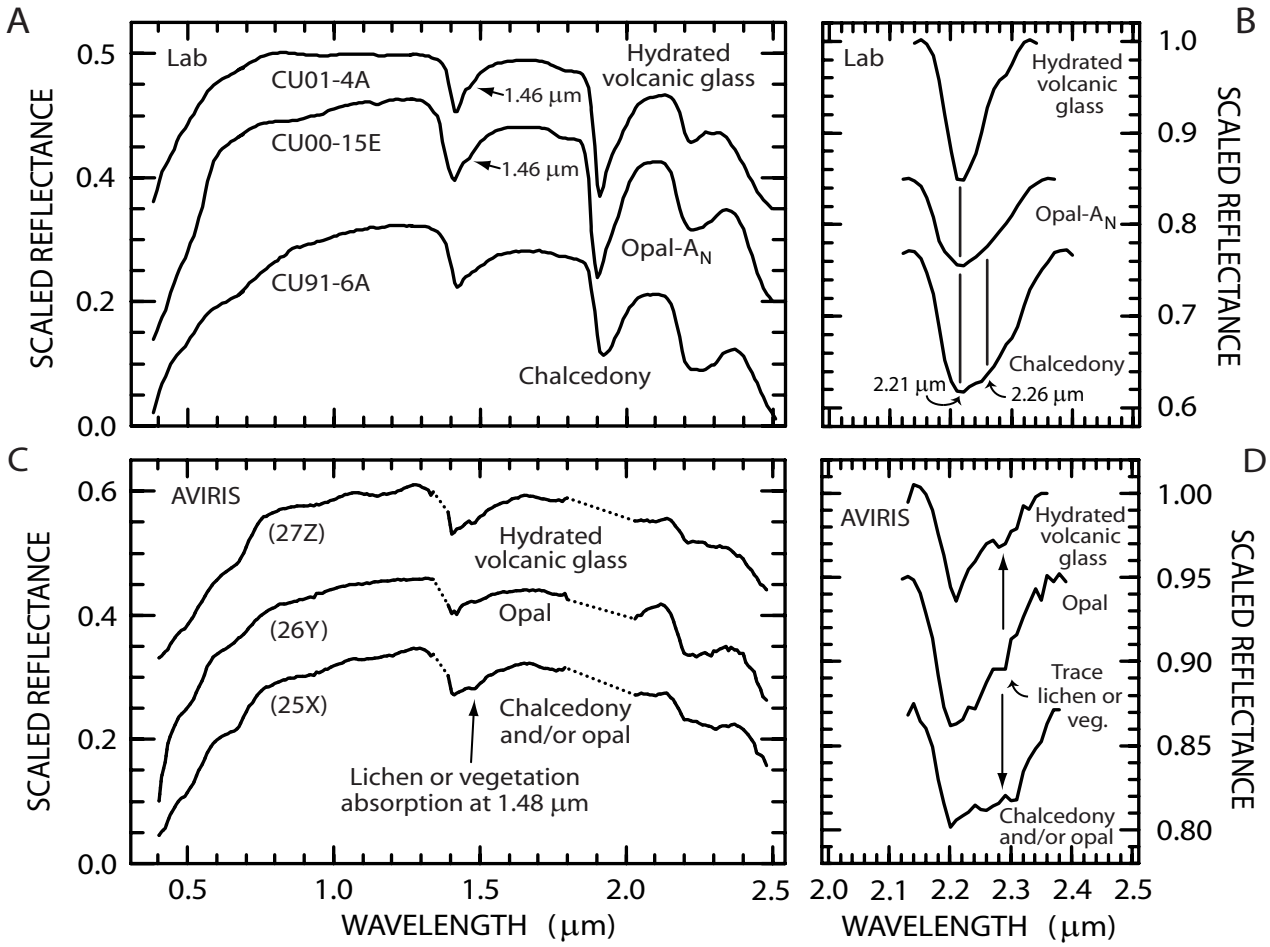

Fig. 15. A) Reflectance spectra of hydrated SiO_2 minerals convolved to AVIRIS resolution and offset vertically for clarity. Arrows point to shoulders on the long wavelength side of the OH overtone band, which are diagnostic of mineralogy (see text for details). Lab spectra measured with an ASD Inc. FR Spectrometer® using samples collected from locations corresponding to number-letter codes in (C). B) Details of the continuum removed 2.21- and 2.26-μm Si-OH combination absorptions. Note how bandwidth increases progressively from hydrated volcanic glass to opal to chalcedony. C) Spectra of hydrated SiO_2 minerals retrieved from the AVIRIS data. Number-letter codes in parentheses refer to spectral retrieval and sample collection locations shown in Figure 5B with analyses listed in Table A1. Regions of strong atmospheric absorption (dotted lines) have been deleted. Spectra offset vertically for clarity. D) Details of continuum removed 2.21- and 2.26-μm Si-OH absorptions in spectra retrieved from the AVIRIS data.

called moganite (Hearny, 1994). The major spectral difference between opal and chalcedony is the latter material's relatively broader 2.26-μm absorption (Fig. 15B) produced by silanol strongly interacting with absorbed freezable water in pore spaces between its fibers (Aines et al., 1984; Graetsch, 1994). Consequently, the correspondingly broader 1.46-μm silanol absorption in chalcedony is not separately detectable at AVIRIS spectral resolution because it overlaps with the nearby sharper silanol absorption at 1.41 μm (Fig.15A). In general, weathered volcanic glass of rhyolitic composition has silanol but it is less hydrated, giving a sharp 2.21-μm absorption but notably lacking a broader 2.26-μm silanol absorption associated with more strongly hydrogen-bonded water (Fig. 15B). Opal can resemble hydrated volcanic glass when it loses most of its hydrogen-bonded water in a low pressure, hyperarid environment such as that on Mars (Milliken et al., 2008).

Chalcedony, opal, and volcanic glass were mapped at Cuprite based on progressive broadening of their 2.21- and 2.26-μm absorptions in AVIRIS data (Figs. 15C and D). The middle of the eastern center is spectrally dominated by chalcedony and opal (Fig. 8; sites 25X and 26Y in Fig. 5B). Field observations indicate that both materials are also present in the western center in smaller elongated zones but identified only intermittently due to extensive spectrally opaque lichen cover. Based on the alteration map of Ashley and Abrams (1980), we expected to detect large areas of opal in the eastern center yet detected only a few small ones. It is possible that more opal is present but spectrally bins into chalcedony when minor (~10-30%) levels of lichen or vegetation partially cover opal, widening the overall 2.21- 2.26 μm absorption feature so it more closely resembles that of chalcedony. Unfortunately, the 1.46-μm shoulder in spectra of hydrated volcanic glass and opal is apparently too weak to be detected with AVIRIS, perhaps because it is swamped by stronger 1.48-μm absorptions from lichen or vegetation cover. A recently quarried, lichen-free hilltop in the NE portion of the eastern center mapped as opal (labeled "Opal Hill" in Figs. 8 and A2). At Cuprite, kaolinite and alunite are also present in most rocks containing opal (Abrams et al., 1977). Even at minor to trace concentrations, these minerals have much stronger absorptions that swamp the weaker absorptions of opal, frequently to an extent where opal's presence is not spectrally detectable.

Several scattered pixels mapped as hydrated volcanic glass in small exposures of the crystal-rich rhyolitic tuff (Tw) 8 km north of the western center (site 27Z in Fig. 5B). We also expected to map more hydrated volcanic glass, given the large areas covered by welded volcanic units surrounding the hydrothermal centers. Swayze et al. (2002) notes that the spectral signature of hydrated volcanic glass diminishes as clay content increases due to weathering in basaltic flows on Hawaiian shield volcanoes. Perhaps the majority of welded tuffs at Cuprite are too weathered or altered to retain significant quantities of hydrated volcanic glass on their exteriors.

Buddingtonite Five areas spectrally dominated by buddingtonite (a NH_4 analogue of K-feldspar) were detected along the western margin of the eastern center. Goetz and Strivastava (1985) named the northernmost outcrop "Buddingtonite Bump" (Figs. 8 and A2). The mineral map (site 11I in Fig. 5B) and retrieved AVIRIS spectra (Fig. 6B), show that buddingtonite at this location is intimately mixed with montmorillonite and does not contain NH_4-smectite in agreement with Felzer et al. (1994). The ammonia in buddingtonite (and in other NH_4-bearing minerals) has a distinct N-H combination absorption at 2.12 μm, a position similar to that of the cellulose absorption in dried vegetation, from which it can be distinguished based on its narrower

band width and asymmetry. If more than a trace level of NH_4-smectite were present then the 2.2 μm Al-OH absorption would be shallower relative to the 2.12 μm N-H combination absorption. Buddingtonite can be formed by alteration of primary feldspar when hydrothermal fluids incorporate ammonium from buried plant matter (Hallam and Eugster, 1976) and is common in low-sulfidation epithermal environments (Yang et al., 2001). This mineral is not uniquely hydrothermal as it also forms diagenetically in sedimentary phosphate deposits (Gulbrandsen, 1974) and oil shale (Loughnan et al., 1983).

Petrographic and SEM examination of samples from the Buddingtonite Bump area shows replacement of plagioclase phenocrysts by quartz and K-feldspar (i.e., buddingtonite). Buddingtonite, a phase not normally associated with advanced argillic alteration, may be remnant from an earlier stage of adularia – sericite type alteration (Queralt et al., 1995).

Spectral Alteration Zones

Even though most AVIRIS pixels contain combinations of alteration minerals in various proportions, they can be binned into six spectral zones representative of the spectrally- and spatially-dominant phases (i.e., hydrated silica, alunite, kaolinite, white mica, chlorite, and adularia-smectite; Fig. 16). For example, a pixel with spectrally dominant alunite identified by Tetracorder may also contain opal and low levels of dickite, kaolinite, jarosite, or goethite. A pixel with spectrally dominant white mica ± montmorillonite may contain low levels of kaolinite or halloysite. The three main electronic region minerals (i.e., hematite, jarosite, and goethite) individually span many of these six spectral zones, with goethite's distribution heavily influenced by post-alteration oxidation of sulfide minerals during weathering, thus, they provide a complimentary but less detailed picture of alteration at Cuprite. The 2-μm vibrational spectral data were also sufficient to define two compositional trends: 1) white-mica is more Al-rich in more intensely altered rock as discussed previously, and 2) K-alunite usually occurs adjacent to chalcedony-rich areas whereas near endmember Na-alunite sometimes occurs without K-alunite in small areas that also contain dickite. This last trend may reflect Na-alunite's tendency to form at higher temperatures.

An alteration map (Fig. 17A), based on the spectral zones defined above, with a few exceptions, is similar to the traditional field-based alteration map compiled by Ashley and Abrams (1980; reproduced in Fig. 4). The main difference is the replacement of traditional "opalized" zones by those of alunite and kaolinite, which spectrally dominate opal's weaker spectral signature. There is a large central hydrated silica (chalcedony/opal) zone in the eastern center but no equivalent one in the western center. Instead, smaller hydrated silica zones encapsulate the steeply east dipping Prospect Fault Zone (Figs. 17A and B), which forms the eastern margin of the western center, and suggest a structurally-controlled late stage of advanced argillic alteration. Propylitic remnants exposed between alunite zones are consistent with significant erosion of the western center, but they are lacking in the eastern center. The western center has central and discontinuous outer white mica ± montmorillonite zones that are also not evident in the eastern center (Fig. 17A). At the northern end of the western center, this outermost zone encompasses an outcrop of unaltered Harkless phyllite. The 2-μm region map, overlain on topography (Fig. 17B), illustrates how unaltered white mica rich rocks (tan, orange, and dark navy blue pixels) crop out topographically lower than advanced argillic alteration (cyan, olive drab, and red pixels) along the northwestern margin of the western center. The presence of these unaltered rocks apparently within the hydrothermal center, mark the location of

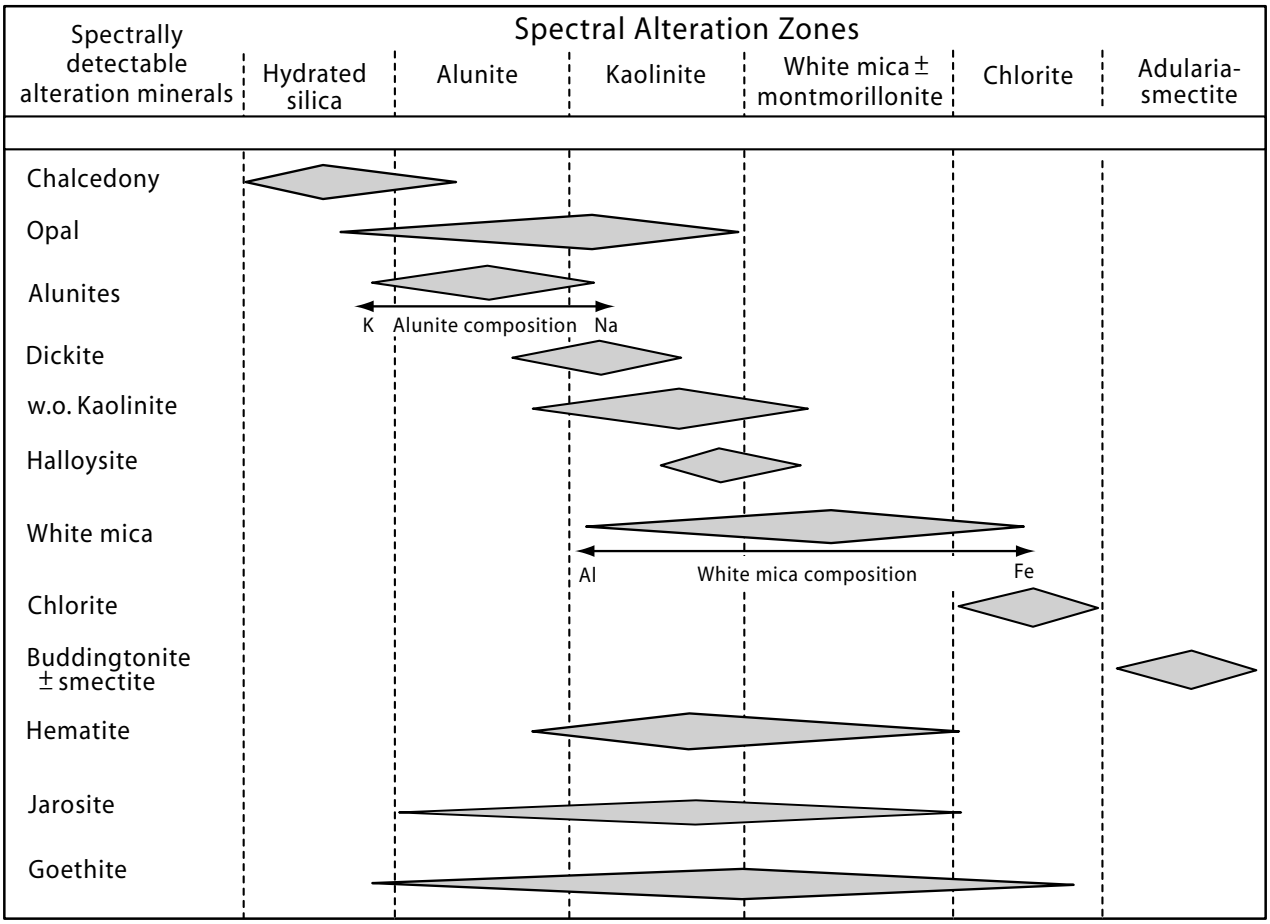

Fig. 16. Alteration zones are based on spectrally detectable mineral associations evident on the 1-μm electronic absorption mineral map (Fig. 5A) and 2-μm region vibrational mineral map (Figs. 5B and 8) and from analyses of field samples listed in Table A1. Diamonds representing individual spectrally-detectable minerals vary in vertical thickness according to their relative spectral abundance in a given alteration zone and overlap, to varying degrees, neighboring zones defined by dashed vertical lines. w.o. = well ordered.

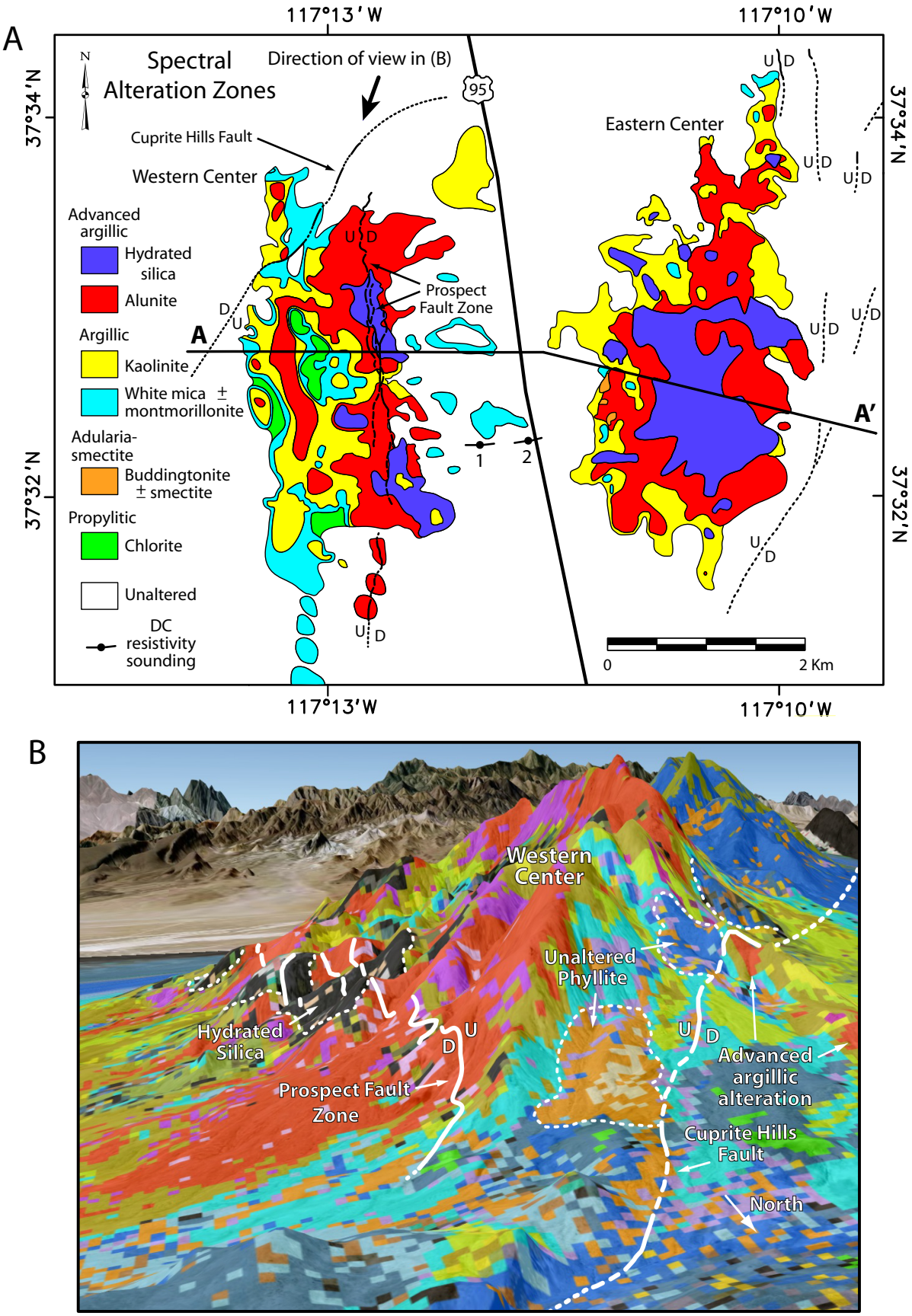

Fig. 17. A) Spectroscopic alteration map generalized from the distribution of minerals shown in Figures 5A and 8 using the spectral alteration zones defined in Figure 16. Colors do not necessarily correlate to those shown in (B). Location of faults taken from Figure 3A. Line labeled A --- A' is the position of the cross section shown in Figure 23. B) 3-D view of the 2-µm region vibrational mineral map draped on Google™ Earth topography and imagery looking SW toward the northern end of the western center at Cuprite. Color key is shown in Figure 8. Note exposures of unaltered Harkless phyllite (tan, orange, and dark blue zones) in the footwall of the Cuprite Hills Fault. Vertical exaggeration is 3x. AVIRIS image does not extend to mountains southwest of the Cuprite Hills area so colors there are from Google™ Earth base images.

a fault, herein named the Cuprite Hills Fault, that has down-dropped altered rocks (up to ~300 m) on the north and exposed unaltered rocks to the south in the footwall beneath the alteration zones. This fault continues SW beneath alluvial cover forming the main range-bounding fault on the west side of the Cuprite Hills Range (i.e., Cuprite Hills Fault in Fig. 3A).

Isotopic Dating

We used argon geochronologic ages to place tighter constraints on the hydrothermal and tectonic events at Cuprite. Five $^{40}Ar/^{39}Ar$ thermal-release ages were obtained to supplement those already reported. Table 1 summarizes relevant isotopic ages and Figure 3A shows the collection locations for samples analyzed in this study and those from an earlier study (Noble et al., 1988). Minerals from four samples were analyzed and their $^{40}Ar/^{39}Ar$ age spectra are shown in Figure 18; analytical values are summarized in Table A2. Sample CU93-45 was collected from the unaltered crystal-rich rhyolitic tuff (Tw) directly overlying Harkless phyllite, 3.5 km north-northwest of the western center outside of the geologically mapped area (location given in Table 1). The age spectrum of sanidine from this sample (Fig. 18A) is relatively simple with some evidence of excess ^{40}Ar, which probably does not affect the plateau date of 26.99 ± 0.08 (2σ) Ma defined by 84.5 percent of the total released $^{39}Ar_K$. The waxy appearing and oxidized biotite exhibits a statistically older plateau date of 27.41 ± 0.20 Ma with a step pattern that may result from excess argon or more likely from $^{39}Ar_K$ recoil from a small amount of chlorite. Both processes result in higher $^{40}Ar/^{39}Ar$ ratios and thus older apparent ages. It is likely that the sanidine date is the most reliable estimate for the extrusion age of the crystal-rich rhyolitic tuff (Tw), thus making it the oldest volcanic unit in the Cuprite/Stonewall Mountain area.

The three other geochronology samples are alunites from hydrothermal centers at Cuprite. Sample CU93-339C was collected from Siebert Tuff, altered to alunite + quartz, and exposed near a silica quarry on the eastern margin of the eastern center. The classical U-shape of this spectrum (Fig. 18B) results from effects of excess ^{40}Ar. Normally this shape and the fact that 74.9 percent of the released ^{39}Ar defines a plateau date of 6.86 ± 0.10 Ma would indicate that the best age estimate for the alunite is 6.86 Ma. The isochron date of 6.77 ± 0.10 Ma is similar. However, this sample had extremely low radiogenic ^{40}Ar percentages and contained very high argon concentrations (Table A2). Both of these features commonly occur if the alunite has abundant fluid inclusions. Fluid inclusions may contain argon and commonly they contain excess ^{40}Ar, thus potentially giving a plateau age that is too old. Nevertheless, given the upper-age constraint provided by altered Spearhead Tuff (alteration < 7.61 Ma) and the lower age constraint provided by faults that post-date eastern center alteration, this age is probably within ± 0.5 m.y. of the true age.

Sample CU93-316A was collected from Harkless phyllite altered to alunite in the western center. It also had excess argon and a relatively low radiogenic Ar yield, but the plateau age of 6.48 ± 0.06 Ma nearly coincides with the isochron age of 6.41 ± 0.04 Ma and both are probably fairly close to the age of the alunite (Fig. 18C). Sample CU93-316B is a bladed alunite from a vein cross-cutting altered Harkless phyllite in the western center. It has the best radiogenic yield of all three alunites, but has a more complicated age spectrum that could be the result of excess argon or mixing of argon from two generations of alunite. It has a plateau age of about 6.21 ± 0.06 Ma, but, if it has two alunite components, one would be 6 Ma and the other about 6.5 Ma (Fig. 18D). The argon closure temperature for alunite is ~ 200 to 220°C (Landis et al., 2005). Therefore assuming the host rocks were below 200°C at the time of alunite formation, the main

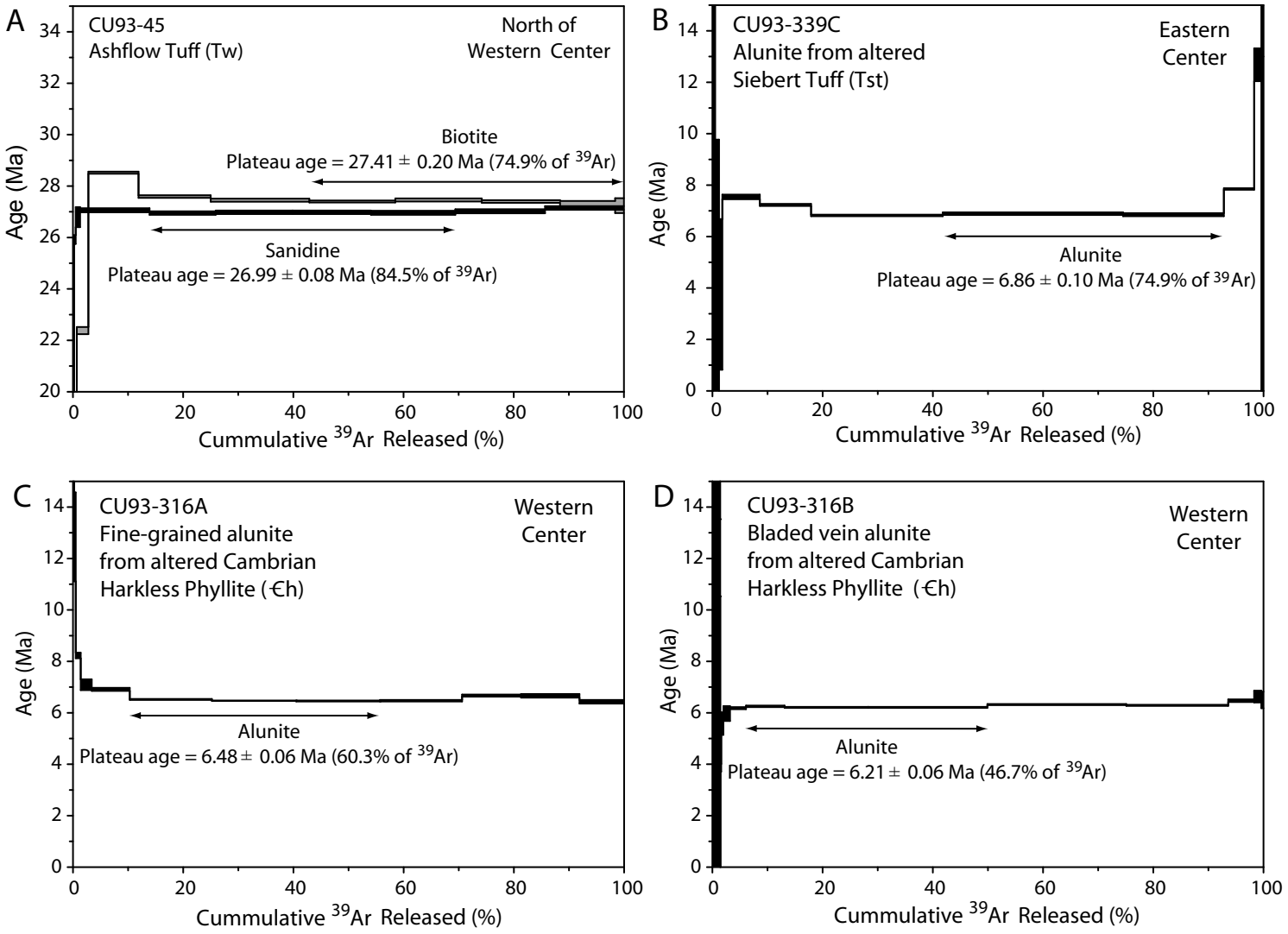

Fig. 18. $^{40}Ar/^{39}Ar$ age spectra for volcanic and altered rocks from the Cuprite area. Source of dated minerals is listed in the upper left of each plot. Table A2 lists $^{40}Ar/^{39}Ar$ data for these spectra. Errors are given at the 2σ level.

phase of hydrothermal activity occurred between 6.21 and 6.48 Ma at these dated areas of the western center.

A sample of the pediment basalt flow (Tb2) from just west of Highway 95 (Fig. 3A) was K-Ar whole rock dated to determine if it is associated with the petrographically similar porphyritic basalt unit (Tb1) sandwiched between the Siebert Tuff and Stonewall Flat Tuff in the eastern center (Fig. 3B). A best estimate age of 6.2 ± 0.2 Ma indicates that the pediment basalt is younger than the Stonewall Flat Tuff (7.61 Ma), which overlies the porphyritic basalt in the eastern center. The pediment basalt flow has a limited areal extent and covers the Rabbit Springs Formation (Trs) in the pediment between the alteration centers. The pediment basalt (Tb2) was not affected by the hydrothermal activity that argillically altered the underlying sediments (Ashley and Abrams, 1980), suggesting that hydrothermal activity had ceased along the eastern margin of the western center prior to eruption of the basalt (6.2 Ma).

Stable Isotopes

The stable isotope compositions of alteration minerals were used to help characterize the environment of alteration at Cuprite. Pyrite, native sulfur, alunite, and jarosite from both hydrothermal centers were analyzed for $\delta^{34}S$; three of the alunite samples were also analyzed for $\delta^{18}O_{SO4}$ and δD. Figure 3A shows the collection locations of stable isotope samples and Table 2 lists analytical results. The sulfate and sulfide samples generally have a relatively narrow range of $\delta^{34}S$ values (5.4 – 8.7‰ VCDT). Exceptions are pyrite samples from the western center, which range from 11.6 to 23.6 per mil VCDT (Fig. 19A). The three alunite samples have $\delta^{18}O_{SO4}$ and δD values that range from 13.9 to 17.6 per mil VSMOW and -67 to -75 per mil VSMOW (Fig. 19B), respectively. VCDT and VSMOW are defined at the bottom of Table 2.

The $\delta^{34}S$ values for pyrite and sulfur in the eastern center samples are typical of volcanic and hydrothermal sulfur in much of the Great Basin (e.g., nearby Round Mountain, Rye et al., 1992) where large values typically reflect the influence of sedimentary sulfur in volcanic and hydrothermal systems. The anomalously large $\delta^{34}S$ values (11.6 to 23.6‰) for hydrothermal pyrite in western center samples compared to values for such pyrite in volcanic rocks in the eastern center (Fig. 19A and Table 2) most likely reflect sulfur derived from isotopically heavy sedimentary pyrite in adjacent Cambrian rocks (e.g., Vikre, 1998). However, in contrast to the high $\delta^{34}S$ values of pyritic sulfur from the western center, native sulfur from the western center has a $\delta^{34}S$ value (5.4‰) comparable to that of pyrite (6.1 to 7.9‰) and sulfur (7.0‰) from the eastern center. The $\delta^{34}S$ values of elemental sulfur in both centers and pyrite in the eastern center are similar to that of associated alunite, suggesting a common origin for sulfur in these phases. Rye et al. (1992) recognized alunite formed in supergene, steam-heated, magmatic-steam, and magmatic-hydrothermal alteration environments based on geologic occurrence and variations in stable isotopes. Following their characterization, the generally similar $\delta^{34}S$ values of alunite, sulfur and pyrite in most Cuprite samples (excluding pyrite influenced by Cambrian sulfur) is consistent with the formation of sulfate in alunite by the oxidation of H_2S in a steam-heated system (Fig. 19A).

The δD and $\delta^{18}O_{SO4}$ values of alunite also support a steam-heated origin. In fact, a steam heated origin for the alunite is virtually required by the combination of large $\delta^{18}O_{SO4}$ and $\delta^{34}S$ values which are similar to those of pyrite in Figure 19A. The origin of the water however is not clear. Mineralization at Cuprite is about 6 to 8 Ma, in which case the δD value of ambient meteoric water was probably about what it is today in much of the Great Basin or less than -100

Table 2. Cuprite stable isotope data.

Sample	Mineral	Location	Source	‰	$\delta^{34}S_{vctd}$	$\delta^{18}O_{SO4}$	δD
		Eastern Center					
CU03-35	Sulfur	N37° 32' 14.7" W117° 10' 58.2"	Rock sample		7.0		
CU03-30A	Pyrite	N37° 32' 37.6" W117°10' 58.5"	Borehole cuttings		7.9		
CU03-32A	Pyrite	N37° 32' 44.0" W117° 10' 12.9"	Borehole cuttings		6.3		
CU03-32A	Pyrite	N37° 32' 44.0" W117° 10' 12.9"	Borehole cuttings (duplicate)		6.1		
CU03-9A1	Jarosite	N37° 32' 29.6" W117° 11' 02.1"	Rock coating		6.9		
CU93-339C	Alunite[/1]	N37° 32' 26" W117° 10' 11"	Fine-grained quartz-alunite rock sample		6.4	17.6	-75
		Western Center					
CU03-37	Sulfur	N37° 32' 46.7" W117° 12' 38.0"	Rock sample		5.4		
CU03-41A	Pyrite[/2]	N37° 32' 47.7" W117° 13' 09.0"	Quartz-alunite + pyrite rock sample		11.6		
CU03-38A	Pyrite	N37° 32' 46.7" W117° 12' 52.0"	Quartz-alunite + pyrite hand separated crystals		23.6		
CU03-1A	Pyrite	N37° 32' 05.6" W117° 12' 30.0"	Borehole cuttings (single crystal)		12.4		
CU03-41B	Jarosite[/3]	N37° 32' 47.7" W117° 13' 09.0"	Coating on CU03-41B rock sample		8.7		
CU03-38B	Alunite	N37° 32' 46.7" W117° 12' 52.0"	Bladed vein alunite + pyrite rock sample		8.6		
CU03-38B	Alunite	N37° 32' 46.7" W117° 12' 52.0"	Bladed vein alunite + pyrite (duplicate) rock sample		8.5		
CU03-41B	Alunite[/3]	N37° 32' 47.7" W117° 13' 09.0"	Quartz-alunite + pyrite rock sample		8.6		
CU93-316A	Alunite[/1]	N37° 32' 25" W117° 13' 11"	Fine-grained quartz-alunite rock sample		6.2	16.8	-72
CU93-316B	Alunite[/1]	N37° 32' 13" W117° 12' 54"	Bladed vein alunite rock sample		8.2	13.9	-67

[/1]See Wasserman et al. (1992) for a description of alunite preparation; measurements by conventional spectrometry.
[/2] Measured on H_2S from pyrite reprecipitated as AgS_2 derived from pyrite. [/3] Measured on sulfate from jarosite or alunite extracted in alkaline solution and reprecipitated as $BaSO_4$. Values are in per mil (‰). $\delta^{34}S$ values reported relative to Vienna Canon Diablo Trolite (VCDT); $\delta^{18}O_{SO4}$ and δD values reported relative to Vienna Standard Mean Ocean Water (VSMOW). Sample location is ±100m or better, unless decimal second is specified then location is accurate to within ± 15m or better (using NAD27 datum).

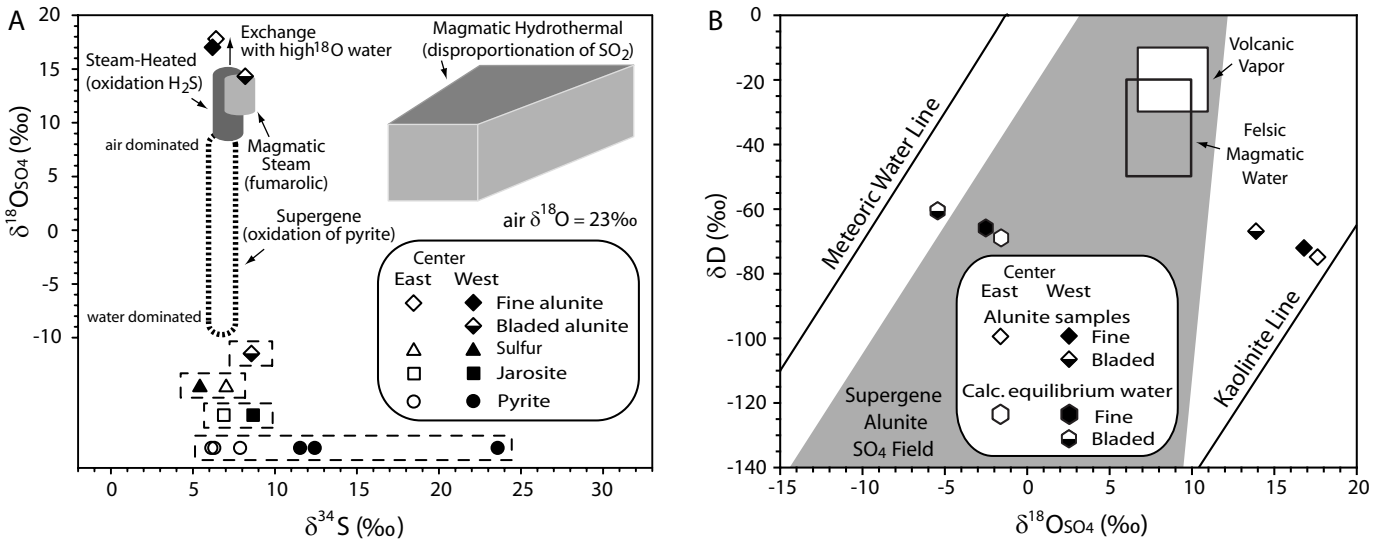

Fig. 19. A) $\delta^{34}S$ and $\delta^{18}O_{SO4}$ values of alunite; $\delta^{34}S$ values of sulfur, jarosite, pyrite, and additional alunite samples from alteration zones at Cuprite. Data fields are from Rye et al. (1992) for predicted O and S isotopic compositions of alunite in steam-heated, magmatic-steam, supergene, and magmatic-hydrothermal environments for assumed composition of parent fluid. B) $\delta^{18}O_{SO4}$ and δD values of selected alunites from Cuprite and their calculated equilibrium water compositions based on 100°C formation temperature and fractionation factors ($-19.25 + \delta^{18}O_{alunite\ SO4} = \delta^{18}O_{H2O}$; $6 + \delta D_{alunite} = \delta D_{H2O}$) from (Stoffregen et al., 1994). Reference lines and supergene field from Rye et al. (1992). Felsic magmatic water and volcanic vapor fields from Taylor (1992) and Giggenback (1992) respectively. Isotopic data listed in Table 2.

per mil based on published studies of ore deposits of similar age (Rye et al., 1992). The calculated composition of the parent alunite fluids in Figure 19B is similar to the evaporated lake water present in the moat of the Creede Caldera (Barton et al., 2000) and was the source of the hydrothermal fluids in the Creede district. Such a moat with evaporated lake water could have formed in the nearby Stonewall Mountain Caldera. The parent fluids may also have evolved as a mixture of meteoric water with a significant component of magmatic water (Fig. 19B).

The bladed alunite from a vein in the western center (CU93-316B) has slightly lower $\delta^{18}O_{SO4}$ and higher $\delta^{34}S$ values compared to a fine-grained alunite (CU93-316A) collected nearby (Fig. 3A). The values for this bladed alunite sample (Fig. 19A) are consistent with formation in a magmatic-steam environment during which the magmatic water dominant fluids undergo rapid decompression (Rye et al., 1992).

The sulfur isotopic compositions of jarosite are permissive of either hypogene or supergene origins. A jarosite sample from the western center has a $\delta^{34}S$ value (8.7‰) that matches the alunite it coats (8.6‰), but is lower than that of associated pyrite (11.6‰). The lack of isotopic similarity with pyrite suggests that this jarosite was most likely hypogene, and may indicate erosion down to the relict boiling zone. In contrast, $\delta^{34}S$ values of jarosite (6.9‰) and pyrite (6.1 – 7.9‰) from the eastern center overlap so jarosite there could be either hypogene or supergene.

Evidence from stable isotopes is consistent with both alteration centers being shallow zones of hydrothermal alteration that were dominated by steam-heated alteration. The data on the bladed vein alunite are indicative of a magmatic-steam environment within the steam-heated system. Similarly, the nearby intimate mixtures of dickite and natroalunite on Dickite Ridge further supports the proximity to a high temperature hydrothermal conduit, such as that observed at Marysvale, Utah (Rockwell et al., 2006).

Geoelectric Cross Section

To better understand the subsurface structure and alteration at Cuprite, individual one-dimensional Direct Current (DC) resistivity soundings were used to construct a geoelectrical profile (Fig. 20). There are two highly resistive zones (red; > 2000 ohm-m) corresponding to surficial exposure of siliceous alteration in the western and eastern hydrothermal centers. A gently approximately 4° west-dipping zone of moderate resistivity (green and yellow; 45 to 300 ohm-m), about 80m thick, separates two low resistivity zones (cyan and blue; < 45 ohm-m). The upper resistivity low extends 45m below the pediment surface between soundings 1 and 2, and the larger resistivity low dips approximately 15° east beneath the eastern center. The eastern center resistivity high has a pair of asymmetric roots with the deeper west-dipping root abutting the large east-dipping resistivity low. The distance between sounding 1 and 10 is large enough that interpolation between them may not provide enough detail to detect a matching low resistivity zone wrapping around the smaller discontinuous siliceous blankets in the western center.

The gently west-dipping zone of moderate resistivity projects up-dip to exposures of the Stonewall Flat Tuff in the eastern center. This zone is thinner than that of the complete Tertiary section exposed on the western margin of the eastern center, but is essentially the same (84 m) as encountered above the Harkless phyllite in borehole CP06 1.3 km north of DC sounding 2. Erosion prior to deposition of the Stonewall Flat Tuff that removed portions of the Siebert and Tw Tuffs can explain the westward thinning of the volcanic section. The close proximity of the

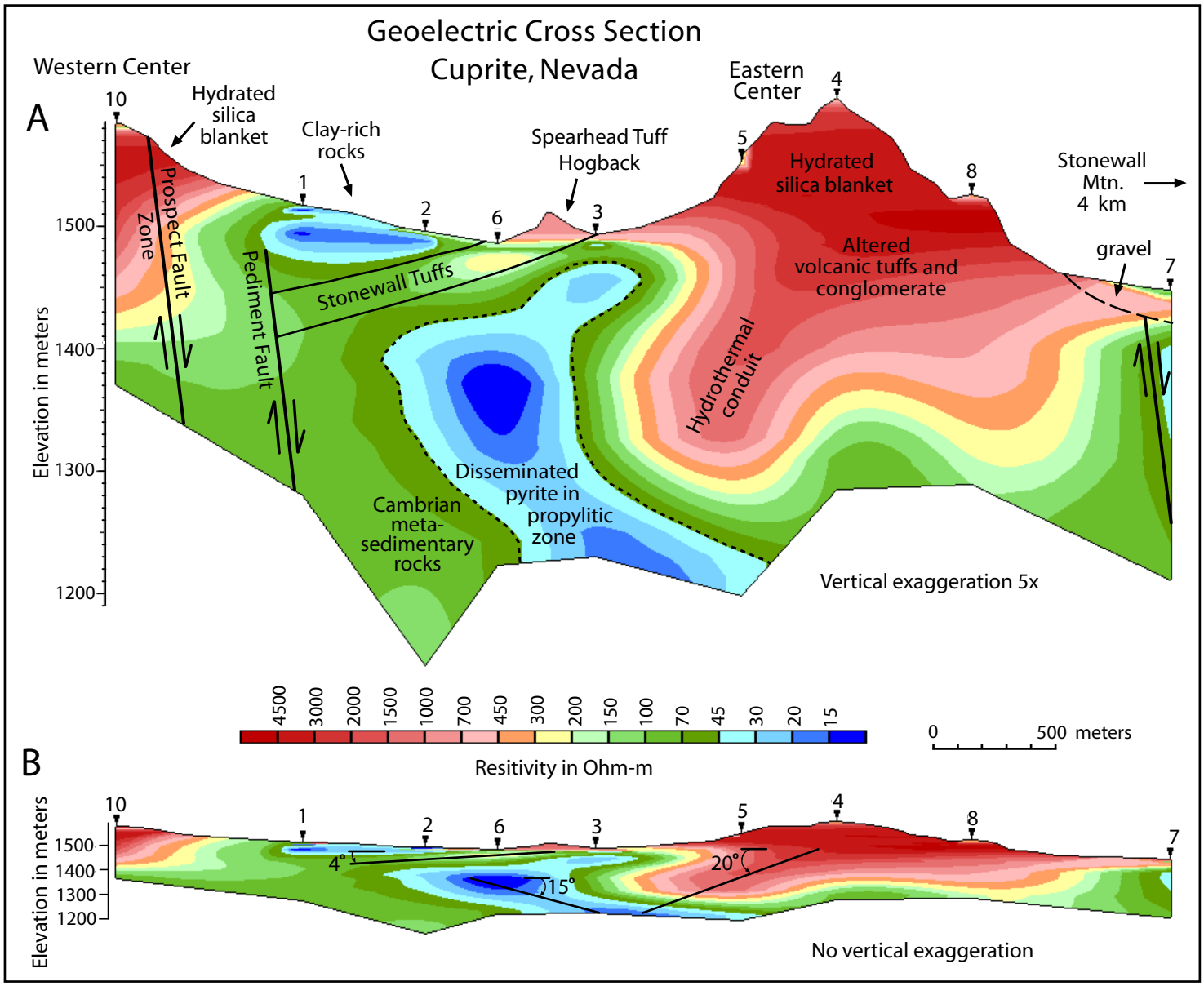

Fig. 20. Interpretive geoelectric E-W cross section of the hydrothermal centers at Cuprite. Locations of one-dimensional Direct-Current (D-C) resistivity soundings are given in Figure 3A. A) Vertically exaggerated (5x) cross-section with annotation. Concealed faults are inferred from geologic observations and borehole logs. Dashed line encompasses inferred pyrite-rich propylitic zone. B) Unexaggerated geoelectric cross section. The inferred propylitic zone dips approximately 15° eastward beneath the eastern center. The Stonewall Flat Tuff layer dips approximately 4° west under the pediment between the alteration centers at the location of the soundings.

eastern center's west-dipping root and the large resistivity low implies a common hydrothermal origin. It is inferred from examination of cuttings from borehole CP06 that the east-dipping resistivity low is caused by disseminated pyrite in propylitically altered rocks including volcanic rocks, Harkless phyllite, and the intrusive quartz latite. Stonewall Flat Tuff that dips west under the pediment between the alteration centers, may have acted as a barrier to rising H_2S-rich vapor beneath the pediment, directing the vapor up-dip toward the eastern center, forming the alteration zones which enclose the west-dipping hydrothermal root (conduit). The small tabular-shaped resistivity low just beneath the pediment surface (between soundings 1 and 2) is likely caused by clay-bearing rocks, which are part of the argillic zone mapped by Ashley and Abrams (1980; Fig. 4) and correlate with the white mica ± montmorillonite zone shown in Figure 17A. An Induced Polarization (IP) survey (C.S. Lide, 1990; unpublished report) indicates the presence of a north-trending fault concealed beneath the pediment. This is consistent with our interpretation of an east-dipping fault (herein referred to as the Pediment Fault) beneath sounding 1, which down drops Stonewall Flat Tuff and overlying clay-rich rocks.

Discussion

Integration of geologic observations with data from spectral mapping, age determinations, stable isotope measurements, and the electrical survey provide insights into the sequence of late Miocene volcanic and hydrothermal events at Cuprite. The Stonewall Flat Tuff is a key chronostratigraphic unit because of its well constrained age (7.54 to 7.61 Ma), its stratigraphic position above the Cuprite Hills conglomerate and below the Rabbit Springs Formation, its alteration by hydrothermal fluids in the eastern center, and its pre- and post-alteration offset along N- and NE-trending faults in the eastern center.

Conglomerates and Their Relation to Hydrothermal Alteration

Tabular clasts of the Harkless phyllite, some altered to advanced argillic grade, are conspicuous within the weakly altered Cuprite Hills conglomerate that is exposed beneath the Spearhead Tuff along the western margin of the eastern center (Fig. 21A). The same conglomerate is completely altered to advanced argillic grade 150 m southeast (Figs. 21B and F). This superimposed alteration is considered a product of the later eastern center system. Contrasting alteration in this conglomerate is evident in the spectra of two adjacent phyllite clasts from the outcrop shown in Figure 21A: one is altered to alunite whereas the other contains white mica (Figs. 21C and D). Muscovite blades in the matrix of the conglomerate are in contact with an alunite-kaolinite clast (Fig. 21E). The juxtaposition of these phases is consistent with the initial acid leaching of the alunite-bearing rock, subsequent erosion, transport, deposition, and *in situ* advanced argillic-grade alteration of the Cuprite Hills conglomerate along the western margin of the eastern center.

The Pozo Formation, a unit believed to be correlative with the Cuprite Hills conglomerate (Albers and Steward, 1972), was sampled at two locations, 14 km to the north near Goldfield and 13 km to the southwest at the base of Mt. Jackson (Fig. 1), to consider alternative sources of altered clasts. Neither site contained Harkless phyllite clasts, confirming the western center as the most likely source of these rock fragments. At site A in Figure 21F, the Cuprite Hills conglomerate and the overlying Spearhead Tuff dip west indicating that down-to-the east fault movement tilted these units, reversing the conglomerate's original dip direction relative to internal clast imbrication. The presence of commingled altered and unaltered Harkless phyllite

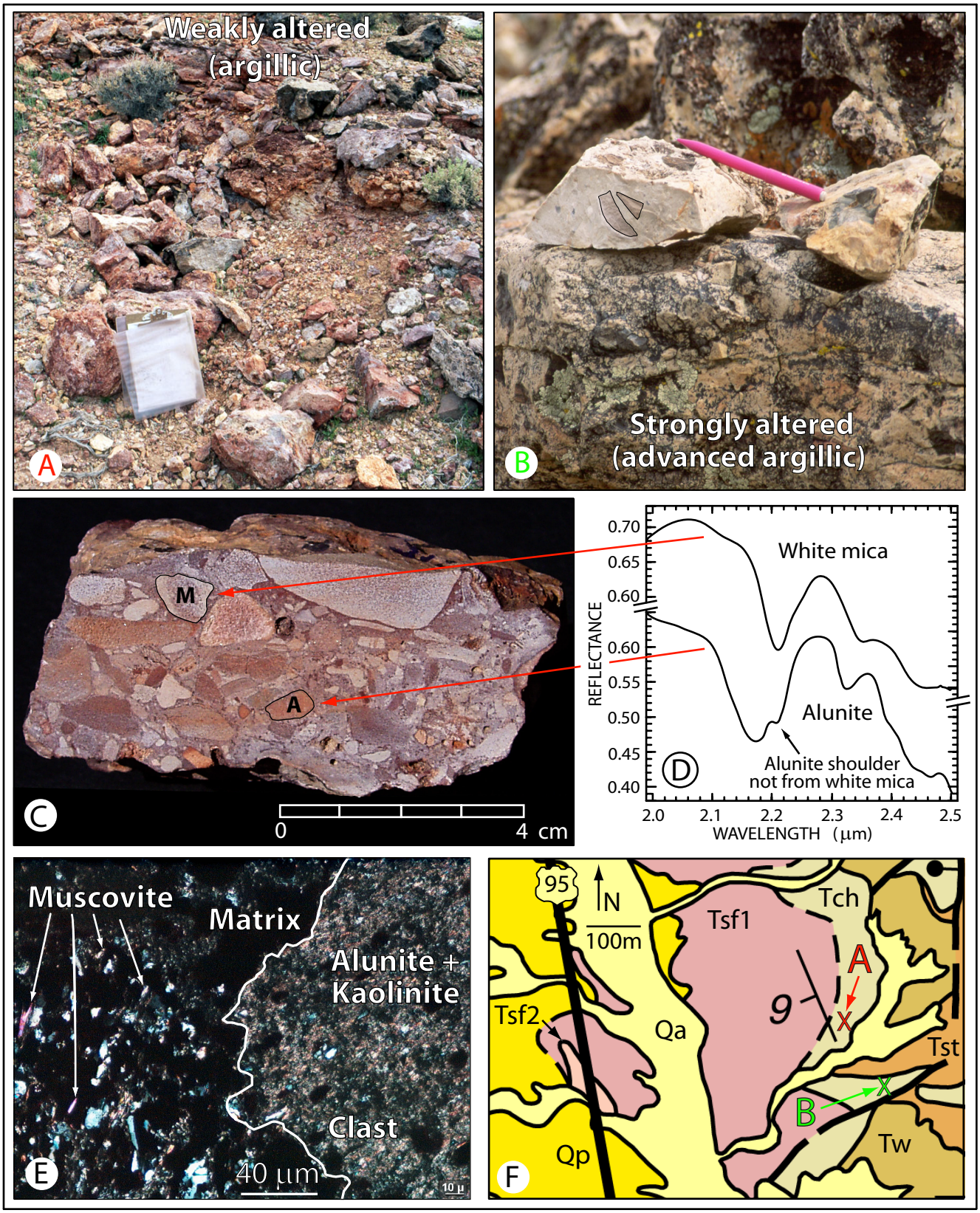

Fig. 21. A) Cuprite Hills conglomerate exposed under the Spearhead member of the Stonewall Flat Tuff in the argillic zone near the western margin of the eastern center. B) Cuprite Hills conglomerate altered to advanced argillic grade 150 m SE of outcrop in "A" (see (F) for locations). Clasts outlined in black are Harkless phyllite in a completely silicified matrix. C) Cuprite Hills conglomerate collected from location "A" has a white mica-bearing Harkless phyllite clast within centimeters of an alunite-bearing Harkless clast. Other clasts are mostly kaolinite-bearing regardless of their color. D) Reflectance spectra of these two clasts indicate spectrally pure but completely different mineral phases in each. E) Thin section photomicrograph of an altered phyllite clast in cross-polarized light adjacent to mica blades in the matrix from the conglomerate sample shown in (C). F) Location map of collection sites A and B; rock unit symbols and colors correspond to those in Figure 3A.

clasts in the Cuprite Hills conglomerate beneath the Spearhead Tuff is direct evidence that the western center was hydrothermally active, elevated, and significantly eroded prior to 7.61 Ma when the Spearhead Tuff was emplaced and prior to pervasive steam-heated alteration in the eastern center.

The Cuprite Hills conglomerate appears to be part of an eastward-thinning talus-fanglomerate wedge formed by debris eroded from an elevated altered western center. Scattered outcrops of unaltered Spearhead Tuff (Tsf1) deposited directly on Mule Springs Limestone and Harkless phyllite at the northern end of the western center (Fig. 3A), without the intervening Siebert and Tw volcanic units, indicates that erosion had stripped the Tertiary section from the western center at this location prior to eruption of the Spearhead Tuff. These outcrops apparently survived widespread erosion where the topographic gradient was low due to negligible vertical offset along the Prospect Fault Zone in this area.

Where well exposed farther south along the eastern margin of the western center, the Prospect Fault zone dips steeply (~70°) east, and beds of the Rabbit Springs Formation on the down-thrown side still dip gently east, probably close to their original orientation. This conglomerate was deposited syntectonically during fault movement or shortly thereafter as indicated by its relative thickness (up to 160 m) in boreholes just east of the fault (Swayze, 1997). In some locations where they are not in fault contact, the Rabbit Springs Formation lies unconformably on Harkless phyllite. Areas of silicification extend continuously from Harkless phyllite across the Prospect Fault Zone into adjacent Rabbit Springs Formation (see area marked "Hydrated Silica" in Fig. 17B) suggesting that the last stage of alteration in the western center post-dates down-to-the-east movement on this fault zone.

In places, there is a high degree of correlation between spectral phase identification and geologic units (Fig. 22). Most departures are due to scatter colluvium, which in places obscures the spectral signature of the underlying bedrock while reflecting that of the topographically higher units.

Outliers of the Rabbit Springs Formation capping the highest ridge of the western center (Trs in Fig. 3A) are mostly altered to advanced argillic grade as indicated by the 2-μm mineral map. The composition of the alunite is the same as that in the underlying Harkless phyllite: alunite composition remains K-rich across their mutual contact as shown at northernmost location marked by A in Figure 22 or varies from Na-K to K, in places, at high angles to their mutual contact as shown at southernmost location marked by A. Petrographic examination found that alunite replaces feldspar in matrix and rock fragments in conglomerate samples from these locations, confirming the rocks were altered *in situ*. At other locations along the ridge, alteration varies from absent to advanced argillic grade over distances of a few meters on a subpixel scale. This implies that the conglomerate at these locations may have been composed of material eroded from unaltered portions of the Harkless phyllite and Tertiary volcanic rocks to the west and deposited in its current position just prior to or after hydrothermal activity ended in this area of the western center.

Distribution, Alteration, and Post-Eruption Faulting of the Stonewall Flat Tuff

At the northeastern corner of the western center scattered outcrops of Spearhead Tuff lie directly on Mulesprings Limestone. The absence of the Siebert and Tw Tuffs is attributed to erosion. The eroded surface of the Siebert Tuff and this unit's eastward increase in thickness are consistent with a topographic high west of Cuprite. The lack of Stonewall Flat Tuff west of the

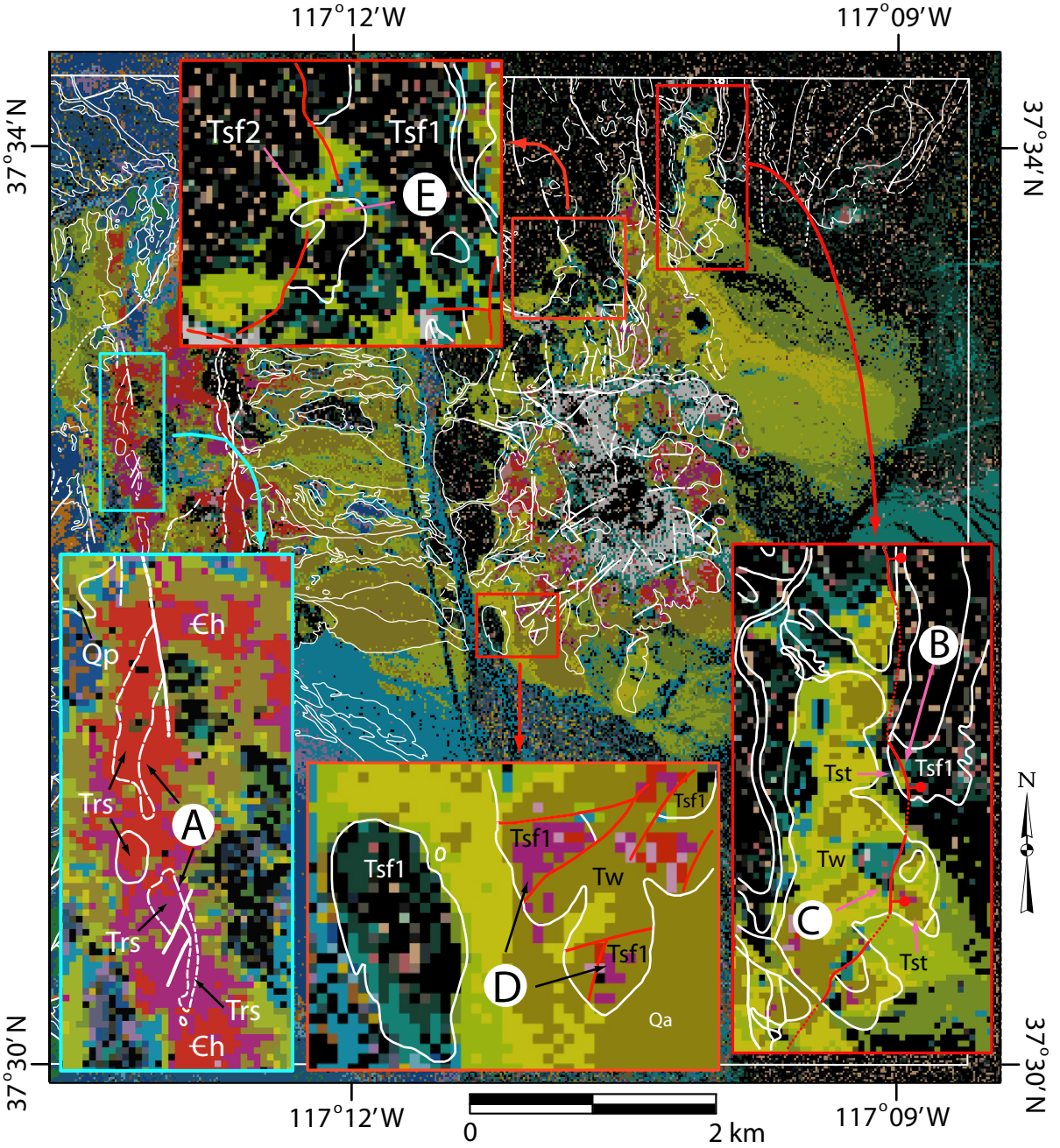

Fig. 22. Geologic unit contacts and faults from Figure 3A for Cuprite overlaid on the 2-µm vibrational mineral map from Figure 5B. In inset images, contacts are white and faults are red except in inset "A" where both are white with faults denoted by thicker lines. Inset "A" shows that alunite compositional zoning cuts across geologic contacts. The arrow from spot marked "B" in lower-right inset image points to the area where N–NE trending normal faults juxtaposes highly altered Siebert Tuff (Tst) against weakly to unaltered Spearhead member of the Stonewall Flat Tuff (Tsf1). The arrow from spot "C" points to an area of weakly altered crystal-rich rhyolitic tuff (Tw) in fault contact with highly altered Siebert Tuff. Arrows from spot "D" point to highly altered Spearhead Tuff (Tsf1). The arrow from spot "E" points to highly altered Civet Cat Canyon member of the Stonewall Flat Tuff (Tsf2).

western center (<10 km west of Stonewall Mountain) and its presence up to 40 km northwest and 34 km southwest of the Stonewall Mountain volcanic center is also consistent with a topographic high that was a barrier to pyroclastic flows moving west of Cuprite at the time of eruption. Weiss et al. (1993) documented stages of erosion, fanglomerate deposition, and local basalt outflows prior to eruption of the Spearhead Tuff in the Gold Mountain-Slate Ridge area 25 km to the southwest. The same sequence is observed at Cuprite, where the lower conglomerate-basalt sequence (Tch - Tb1) may indicate the onset of cauldron collapse with fault movement, erosion, and discharge of basalt prior to the eruption of the Stonewall Flat Tuff. The same lithologic sequence (Trs – Tb2) repeats stratigraphically above the Stonewall Flat Tuff. In this context, eruption of the Stonewall Flat Tuff was a short-lived event during a protracted cauldron collapse.

A north-trending normal fault juxtaposes altered Siebert Tuff (Tst) against weakly to unaltered Spearhead Tuff (Tsf1) in the northeastern part of the eastern center (spot B in Fig. 22). Further south, this same fault juxtaposes weakly altered crystal-rich rhyolite tuff (Tw) against down-dropped highly altered Siebert Tuff (spot C in Fig. 22), suggesting movement post-dates hydrothermal alteration in the eastern center. This fault may be part of a large array of circumferential faults that formed the edge of the Stonewall Mountain Caldera. Both members of the Stonewall Flat Tuff (Tsf1 and Tsf2) were involved in the most intense stage of advanced argillic alteration in the eastern center (marked by magenta and red alunite pixels in spots D and E in Fig. 22), indicating that hydrothermal activity there is younger than 7.54 Ma ($^{40}Ar/^{39}Ar$ date on sanidine from the Civet Cat Canyon member of the Stonewall Flat Tuff; Table 1). If the $^{40}Ar/^{39}Ar$ date on altered rocks from the eastern center is interpreted as the age of alunite formation, then hydrothermal activity ceased in the eastern center sometime after 6.9 ± 0.5 Ma. This date is from 0.1 to 1.1 m.y. younger than age estimates for cauldron collapse (Foley, 1978; Noble et al., 1984; Weiss and Noble, 1989). Hydrothermal activity in the eastern center chronologically overlaps with volcanic events at nearby Stonewall Mountain.

The old pediment (labeled TQoa in Fig. 3A) at the north end of Cuprite is covered with cobbles of Emigrant Formation that were eroded and transported southeast from the nearby Goldfield Hills. Currently this area is starved for sediment because subsequent movement on the NE-trending Cuprite Hills fault has lowered the source streams. Weiss et al. (1993) reasoned that faults with this trend formed shortly after the eruption of the Stonewall Flat Tuff and that much of the present topography of the area dates from late Miocene time. Isotopic dating of supergene jarosite at Goldfield confirms that the late Miocene was a time of weathering in this area (Vasconselso et al., 1994). The topographic profile of the western center, as seen from the Goldfield Hills, suggests that the Cuprite Hills Fault truncated the east-sloping pediment surface upon which the Rabbit Springs Formation was deposited. This fault also down-dropped rocks, altered to advanced argillic grade, along the NW margin of the western center (Fig. 17). The fine-grained alunite sample (CU93-316A; Table 1 and Fig. 3A) that was collected for $^{40}Ar/^{39}Ar$ dating from just under the erosional surface next to altered outliers of the Rabbit Springs Formation, has a date of 6.48 Ma, thus providing a minimum age for deposition of the conglomerate at that locality. Because these outliers cap the highest peaks in the western center, deposition of the conglomerate predated movement on the Cuprite Hills Fault. The Cuprite Hills Fault continues northeast from the western center, with progressively less vertical offset. It intersects the western margin of the remnant (~20 km diameter) Stonewall Mountain Caldera, leaving the range containing the eastern center isolated and elevated above Stonewall Playa. This playa occupies the moat surrounding the Stonewall Mountain resurgent dome, formed in the

caldera sometime after 7 Ma.

Geologic Cross Section

The illustrative geologic cross section shown in Figure 23 is based on the geoelectric cross section, borehole data, outcrop geology, and the 2-μm region spectral alteration zone map from Figure 17A. The interpretation that advance argillic alteration zones overprint adularia – sericite type low-sulfidation alteration is based on observations of these zones where they are exposed in gullies and their relative positions in boreholes. The western center is considered to be the result of two hydrothermal centers recognizable at the surface as two N-S trending alunite zones separated locally by remnant sericite (kaolinite + white mica) and propylitic zones (compare Figs. 8 and 23). These and other pyrite-bearing propylitic zones, exposed beneath advanced argillic alteration in the southern portion of the western center, may have formed deeper in the hydrothermal system prior to development of the steam-heated zones. The older center underlies the westernmost ridge (see the highest point capped by Trs in Fig. 23) and has been eroded sufficiently to expose underlying adularia – sericite type alteration. This upland was the likely source of the altered detritus in the Cuprite Hills conglomerate. The youngest hydrothermal center formed along the eastern margin of the western center, and is marked by advanced argillic alteration that in places surrounds approximately 100 m thick silicified zones of altered Rabbit Springs Formation mostly on the down thrown side of the Prospect Fault Zone.

The pre-Spearhead Tuff volcanic section is thickest under the eastern center, having been tilted eastward prior to its removal by erosion from the western center and subsequent deposition of the overlying Cuprite Hills conglomerate. According to the well log of borehole CUP-1, a few meter thick portion of the Spearhead Tuff lies between the Prospect and Pediment Faults 200 m east of the western center (see Fig. 23). If so, then movement on the Prospect Fault Zone postdates the eruption of that volcanic unit (7.61 Ma). The westernmost and oldest hydrothermal system in the western center may have been more extensive prior to erosion and faulting. Restoration of the fault's offset suggests that altered Harkless phyllite is potentially concealed beneath unaltered Emigrant Formation and Mule Springs Limestone on the down-thrown side of the Cuprite Hills Fault along the section line.

Quartz latite dikes ranging in thickness from 10 to 50 m were intersected in 6 out of 9 boreholes, which penetrated the Harkless phyllite under the pediment between the hydrothermal centers (see borehole symbols with blue labels in Fig. 3A). In the boreholes, just as in outcrop, these dikes are restricted to Paleozoic rocks, suggesting that they do not intrude Tertiary rocks and may be pre-Tertiary in age. If this is the case, they could be chronologically and compositionally related to 170 Ma quartz monzonite dikes, which intrude the lower Cambrian rocks at Goldfield (Ashley and Silberman, 1976). Cuttings from borehole CP06 indicate the presence of Harkless phyllite at a depth of 137 m under the pediment just west of the eastern center. However, 8 boreholes within the eastern center penetrated up to 300 m of altered Tertiary volcanic rocks but did not intersect underlying Harkless phyllite or intrusive quartz latite, suggesting a pre-Spearhead Tuff eastward tilt of the Tertiary-basement erosional contact (Fig. 23).

Alteration Sequence

Hayba et al. (1985) point out that adularia – sericite type epithermal systems may occur along the margins of calderas. Advanced argillic alteration can form from oxidation of H_2S above the

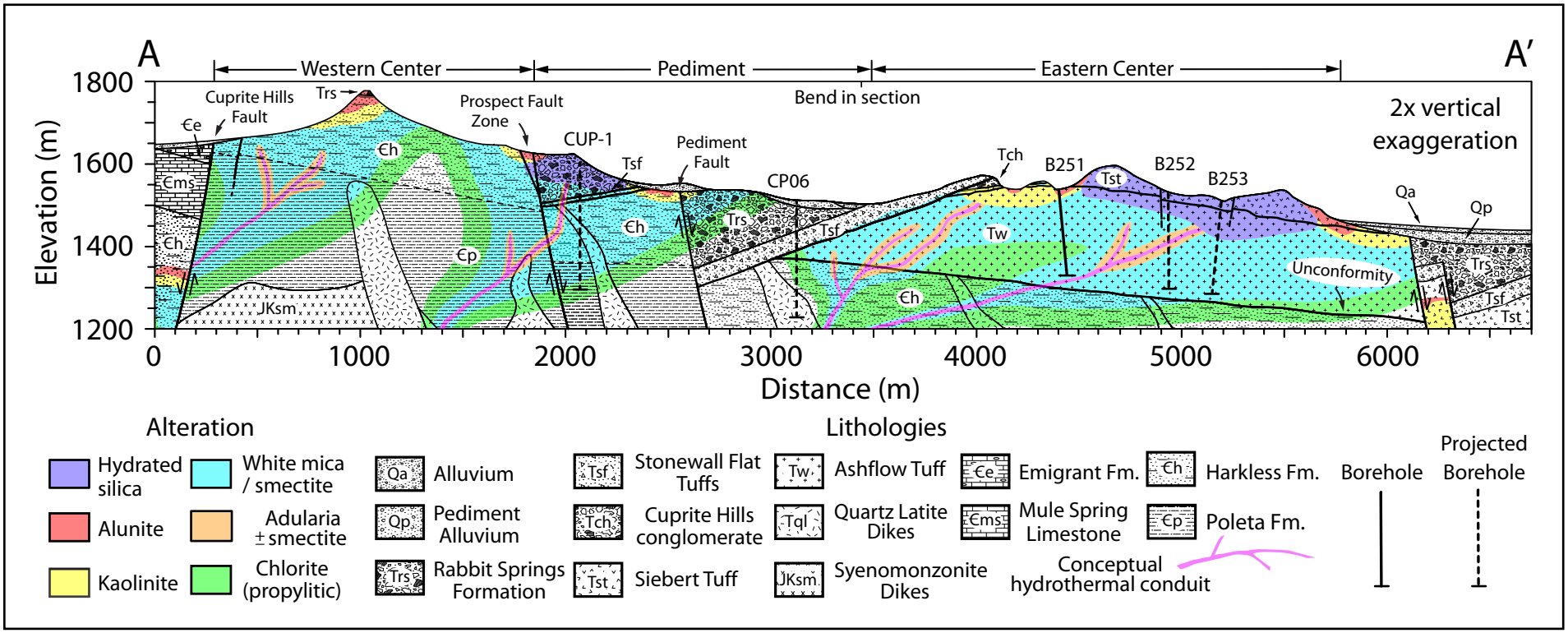

Fig. 23. Illustrative geologic cross section of the western and eastern alteration centers at Cuprite. 2x vertical exaggeration. Cross section is based on the geoelectric cross section, borehole cuttings, outcrop geology, and the spectral alteration zone map (Fig. 17A). Labeled vertical to near vertical lines with cross bars at bottom mark boreholes. Solid symbol is a borehole on the section line; dashed symbols are projected from nearby boreholes (< 450 m distance). Section line and borehole locations are shown in Figure 3A.

water table in these low-sulfidation systems (Rye et al., 1992) resulting in advanced argillic alteration overprinting from intense acid leaching of the rocks. Underlying siliceous blankets form where downward percolating acid solutions mix with ground water (Hedenquist et al., 2000; Fournier 1985). These are likely explanations for the advanced argillic (alunite/kaolinite) and underlying siliceous (chalcedony/opal) alteration zones evident on spectral mineral maps of Cuprite's eastern center.

Ebert and Groves (1996) note that the illite component of interlayered illite-smectite increases with depth in the Crofoot/Lewis Mine low-sulfidation hot spring deposit near Winnemucca, Nevada. At Cuprite, Na-montmorillonite was spectrally detected in both alteration centers but more so in the eastern center which is not as deeply eroded as the western center. If the illite component increases with depth below the advanced argillic and siliceous blankets, as happens at the Crofoot/Lewis deposit, then illite should be more abundant in the more deeply eroded western center. However, because it is difficult to spectrally differentiate illite from muscovite in the NIR, a correlation between illite content and depth of burial cannot be explicitly checked using AVIRIS data of the western center where muscovite-rich phyllites host the alteration.

Summary and Conclusions

Mineral maps based on 0.4 – 2.5 μm spectral data collected by the Airborne Visible/Infrared Imaging Spectrometer (AVIRIS) were used to characterize two centers of relict advanced argillic alteration at Cuprite, Nevada. In total, 36 mineral categories in the electronic and vibrational spectral regions were mapped using the Tetracorder spectral-shape matching system, and verified by laboratory analyses of field samples. These categories include Fe-bearing minerals, clays, sulfates, carbonates, and for alunite and micas, their solid-solution compositions. Jarosite, goethite, and hematite have absorptions in the electronic region (0.4 – 1.3 μm), and were successfully differentiated within the study area. Jarosite and mixtures dominate the western center, indicating low pH surface conditions in many areas that were created by sulfide mineral oxidation, while other areas are spectrally dominated by coarser-grained hypogene jarosite.

The distribution of minerals with absorption features in the vibrational region (1.3-2.5 μm) provides the most detailed picture of advanced argillic alteration at Cuprite. White mica compositions determined with Tetracorder are nearly identical to those measured in field samples. Micas become more Al-rich in the most intensely altered areas and near intrusive rocks. Alunite composition varies from pure K to intimate mixtures of Na-K endmembers with subpixel occurrences of huangite, the Ca-analogue of alunite. Na-K endmember mixtures may indicate areas of relatively lower temperature alunite alteration, while co-occurring Na-alunite and dickite may be proximal to hydrothermal conduits. Although intimate mixtures of Na-K alunite endmembers are difficult to confidently separate from intermediate composition alunites at AVIRIS spectral resolution, no intermediate alunite was detected in higher spectral resolution measurements of field samples. This is interpreted to indicate formation at temperatures below the alunite solvus. Dickite and halloysite were found in discrete spatial areas in the western center while well-ordered kaolinite was widely distributed in both centers. Mixtures of smectite, likely wind derived, white mica, and well-ordered kaolinite produce reflectance spectra that mimic the spectral signature of disordered kaolinite or halloysite. Chalcedony, opal, and hydrated volcanic glass were differentiated based on changes in the relative strengths of their Si-OH combination absorptions in the 2.2 – 2.3 μm region. Partial lichen cover on opal spectrally

mimics chalcedony; consequently opal was detected only where it exists in lichen-free areas not spectrally dominated by kaolinite and alunite. The distribution of the NIR-active minerals listed above was used to construct a synoptic map of spectral alteration zones, which resembles the traditional field-based alteration map but has additional detail shown by kaolinite and alunite zones. This spectral map enabled recognition of previously unrecognized early hydrothermal alteration in the western center.

Figure 24 summarizes geologic and hydrothermal events at Cuprite. The sequence of events begins with the formation of a regional high west of and including the present day western center. This uplift likely occurred during movement on the Silver Peak – Lone Mountain detachment about 11 Ma. Earlier deposited Tw and Siebert Tuffs were tilted eastward, and eroded to expose basement rock in the western center. Early adularia-sericite and steam-heated alteration in the western center is probably linked to activity in the nearby Stonewall Mountain volcanic complex. Eroded altered debris from the western center blanketed the remaining dissected pre-Stonewall volcanic section to the east. Flows of porphyritic basalt locally covered this debris. At 7.61 Ma the Stonewall Mountain volcanic complex erupted, depositing the Spearhead Tuff. Following eruption of the Civet Cat Canyon Tuff at 7.54 Ma, the volcanic complex collapsed piecemeal forming a caldera. Steam-heated hydrothermal activity spread east (toward the caldera) into the pediment and eastern center. During cauldron collapse, movement on the Prospect and Pediment Faults offset the western and eastern centers in stair-step down to the east fashion. Erosion of highlands to the west deposited conglomerate on top of the hydrothermally active western center. Hydrothermal activity may have continued during cauldron collapse but in places appears to have ceased prior to final movement on these faults in the eastern center. A resurgent dome formed in Stonewall Caldera sometime after 7 Ma.

Isotopic dating of the Stonewall Flat Tuff, the pediment basalt, and alunite collected from both centers give a minimum age of 7.61 Ma for onset of hydrothermal activity in the western center and a 6.2 Ma date for its cessation (based on the age of the unaltered pediment basalt Tb2). Hydrothermal activity ceased after late stage magmatic steam alunite veins formed at 6.21 Ma. These ages indicate the western center was intermittently active from at least 7.61 to 6.21 Ma. Subsequent movement on the Silver Peak – Lone Mountain detachment likely down-dropped the upland west of the western center around 5 Ma. Related movement on the west-dipping Cuprite Hills fault resulted in burial of altered rocks at the north end of the western center, left outliers of the Rabbit Springs Formation perched atop the western center, and down dropped Stonewall Flat Tuff north of the eastern center. What was once a western upland became the isolated Goldfield and Cuprite Hills ranges.

Both high- and low-sulfidation systems can have advanced argillic overprints (Hedenquist et al., 2000; White and Hedenquist, 1995). The existence of advanced argillic alteration at Cuprite, the lack of abundant pyrite (> 5% vol.), occurrence of bimodal rhyolite/basalt volcanism, location in the upper plate of a detachment associated with a metamorphic core complex in an extensional back arc rift tectonic setting, presence of a massive siliceous blanket (preserved in the eastern center), and recognition of a steam-heated alunite stable isotope signature, are all compatible with a low-sulfidation hydrothermal system (Hedenquist et al., 2000; Sillitoe and Hedenquist, 2003). Evidence summarized above suggests that Cuprite is a late Miocene low-sulfidation adularia – sericite type hot spring deposit overprinted by late-stage steam-heated advanced argillic alteration.

Spectral mineral maps can be used to help recognize the degree of sulfidation in an

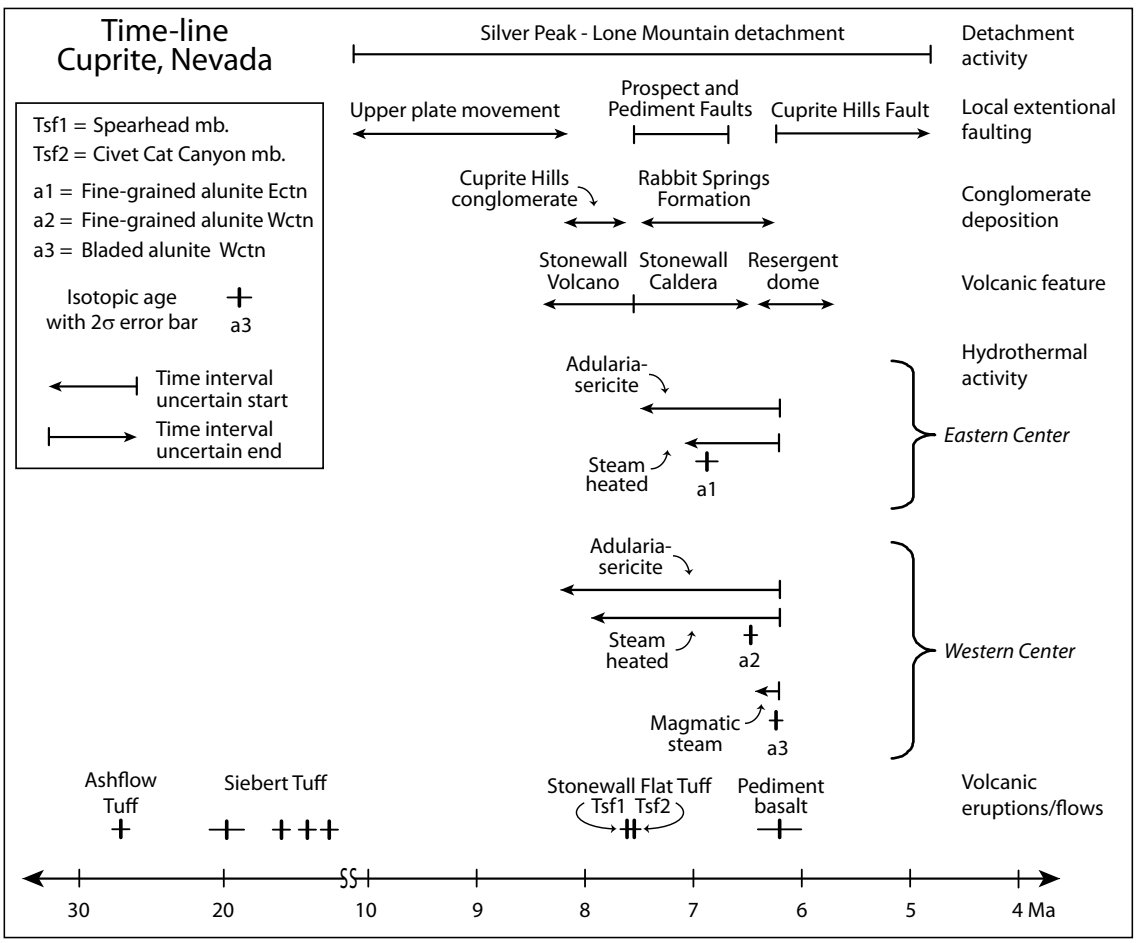

Fig. 24. Time-line for fault activity, conglomerate deposition, volcanic eruptions, and hydrothermal activity at Cuprite. Positions of isotopic age symbols are based on dates from Table 1.

epithermal system. Although the presence of dickite is typical of high-sulfidation systems, it can also occur as near-surface fluids descend down structures. Its presence exclusively in the western center may just indicate erosional exposure of a relatively deeper level of an older hydrothermal system there. Notable is the lack of pyrophyllite in either center, which is normally associated with high-sulfidation hydrothermal systems. Because imaging spectroscopy measures every square meter of exposed surface, and because pyrophyllite has sharp diagnostic spectral features at 2.17 μm, it can be easily detected if concentrated (> ~10 wt%) and exposed. From a remote sensing perspective, the spectral detection of pyrophyllite and/or intermediate composition alunite in areas of advanced argillic alteration with adequate erosional exposure would be a strong indication of a high-sulfidation epithermal system. Likewise, imaging spectroscopy is well suited to detection of buddingtonite, and as experience is gained at other epithermal deposits, this mineral may prove an effective indicator of low-sulfidation adularia – sericite type systems.

In conclusion, imaging spectroscopy can fill gaps in alteration mapping where access is limited and it helps to focus efforts on the ground. In this way, it is complimentary to field spectroscopy and other field methods. What takes weeks to measure on the ground takes an imaging spectrometer only a few minutes to measure from above. Adding imaging spectroscopy to a traditional exploration toolkit provides a bird's eye perspective of alteration, which can narrow the choice between deposit models and thereby expedite exploration.

Acknowledgements

Many people contributed their time, ideas, and mineral samples to this study. Special thanks are due G. Plumlee, R. Bisdorf, S. Cunningham, C. Alpers, A. Brayko, C. Gent, S. Huebner, T. King, M. Hudson, T. Grauch, I. Brownfield, W. Hamilton, C. Kortemeier, W. Buller, B. Atkinson, M. Kraus, B. Emery, A. Gallagher, R. Kokaly, D. Allerton, R. McDougal, D. Yager, C. Holm-Denoma, and many others. Thoughtful suggestions and/or reviews from J. Mars, S. Cunningham, J. Dilles, A. Thompson, T. Cudahy, J. Hedenquist, R. Rye, B. Rockwell, B. Berger, B. Minsley, D. Bish, W. Calvin, and E. Balan significantly improved the manuscript. R.O. Green and the AVIRIS team at the Jet Propulsion Laboratory supplied AVIRIS data and their "can do" attitude. R. Rye and P. Middlestead provided stable isotopic measurements. C.L. Deyell provided a huangite-bearing alunite sample. R. Fleck provided the whole rock isotopic age on the pediment basalt. Santa Fe Pacific Gold Corporation and Nevada Western Silica Corporation provided borehole data. Newmont Mining provided access to borehole cuttings. This study is dedicated to George Desborough for his relentless encouragement to investigate all things alunite and to Larry Rowan for introducing Cuprite to the remote sensing community. The USGS Spectral Library and Remote Sensing Projects, and the NASA program W15805 (R. Clark, PI) provided funding. Any use of trade, firm, or product names in this publication is for descriptive purposes only and does not imply endorsement by the U.S. Government.

References

Abrams, M.J., Ashley, R.P., Rowan, L.C., Goetz, A.F.H., and Kahle, A.B., 1977, Mapping of hydrothermal alteration in the Cuprite mining district, Nevada using aircraft scanner images for the spectral region 0.46-2.36 μm: Geology, v. 5, p. 713-718.

Albers, J.P., and Stewart, J.H., 1972, Geology and mineral deposits of Esmeralda County, Nevada: Nevada Bureau of Mines and Geology Bulletin 78, 80 p.

Aines, R.D., Kirby, S.H., and Rossman, G.R., 1984, Hydrogen speciation in synthetic quartz: Physics and Chemistry of Minerals, v. 11, p. 204-212.

Ashley, R.P., and Abrams, M.J., 1980, Alteration Mapping Using Multispectral Images-Cuprite Mining District, Esmeralda County, Nevada: U.S. Geological Survey Open File Report 80-367, 17 p.

Ashley, R.P., and Silberman, M.L., 1976, Direct dating of mineralization at Goldfield, Nevada, by Potassium-Argon and fission-track methods: Economic Geology, v. 71, p. 904-924.

Balan, E., Saitta, A.M., Mauri, F., and Calas, G., 2001, First-principles modeling of the infrared spectrum of kaolinite: American Mineralogist, v. 86, p. 1321-1330.

Balan, E., Lazzeri, M., Saitta, A.M., Allard, T., Fuchs, Y., and Mauri, F., 2005, First-principles study of OH-stretching modes in kaolinite, dickite, and nacrite: American Mineralogist, v. 90, p. 50-60.

Barton, P.B., Steven, T.A., and Hayba, D.O., 2000, Hydrologic budget of the late Oligocene Lake Creede and the evolution of the upper Rio Grande drainage system, *in* Bethke, P.M. and Hay, R.L., eds., Ancient Lake Creede: Its volcano-tectonic setting, history of sedimentation, and relation to mineralization in the Creede Mining District: Boulder, Colorado, Geological Society of America Special Paper 346, p. 105-126.

Basciano, L.C., and Peterson, R.C., 2008, Crystal chemistry of the natrojarosite-jarosite and natrojarosite-hydronium jarosite solid-solution series: A synthetic study with full Fe site occupancy: American Mineralogist, v. 93, p. 853-862.

Bigham, J.M., Schwertmann, U., Carlson L., 1992, In Biomineralization: Processes of Iron and Manganese, *in* Skinner, H.C.W., Fitzpatrick, R.W., eds., Catena Supplement 21: Cremlingen-Destedt, Germany, p. 219-232.

Bishop, J.L., and Murad, E., 2005, The visible and infrared spectral properties of jarosite and alunite: American Mineralogist, v. 90, no.7, p. 1100-1107, doi: 10.2138/am.2005.1700.

Bookin, A.S., Drits, V.A., Plancon, A. and Tchoubar, C., 1989, Stacking faults in kaolin-group minerals in the light of real structural features: Clays and Clay Minerals, v. 37, p. 297-307.

Burns, R.G., 1993, Mineralogical applications of crystal field theory: Cambridge University Press, 551p.

Chang, Z., Hedenquist, J.W., White, N.C., Cooke, D.R., Roach, M., Deyell, C.L., Garcia, J., Gemmel, J.B., McKnight, S., and Cusion, L.A., 2011, Exploration tools for linked porphyry and epithermal deposits: Examples from the Mankayan intrusion-centered Cu-Au district, Luzon, Philippines: Economic Geology, v. 106, p. 1365-1398.

Chen, Xinnfeng, Warner, T.A., and Campagna, D.J., 2010, Integrating visible, near-infrared and short-wave infrared hyperspectral and multispectral thermal imagery for geologic mapping at Cuprite, Nevada: a rule based system: International Journal of Remote Sensing, v. 31, no. 7, p. 1733-1752, doi: 10.1080/01431160902926616.

Clark, R.N., 1999, Chapter 1: Spectroscopy of rocks and minerals, and principles of spectroscopy, *in* A.N. Rencz, ed., Manual of Remote Sensing, Volume 3, Remote Sensing for the Earth Sciences: John Wiley and Sons, New York, p. 3-58.

Clark, R.N., Roush, T., 1984, Reflectance spectroscopy: quantitative analysis techniques for remote sensing applications: Journal of Geophysical Research, v. 89, p. 6329-6340.

Clark, R.N., T.V.V. King, M. Klejwa, G.A. Swayze, and N. Vergo, 1990, High spectral resolution reflectance spectroscopy of minerals: Journal of Geophysical Research, v. 95,

p. 12653-12680.

Clark, R.N., Livo, K.E. Livo, and Kokaly, R.F., 1998, Geometric Correction of AVIRIS Data Using On-Board Engineering Information, *in* Green, R.O., ed., Summaries of the 7th Annual JPL Airborne Earth Science Workshop: Jet Propulsion Laboratory Publication 97-21, p. 57-66.

Clark, R.N., Swayze, G.A., Livo, K. E., Kokaly, R.F., King, T.V.V., Dalton, J.B., Vance, S., Rockwell, B.W., Hoefen, T., and McDougal, R.R., 2002, Surface reflectance calibration of terrestrial imaging spectroscopy data, *in* Green, R.O., ed., Proceedings of the Eleventh JPL Airborne Earth Science Workshop: Jet Propulsion Laboratory Publication 03-04, p. 43-63.

Clark, R.N., Swayze, G.A., Livo, K. E., Kokaly, R.F., Sutley, S.J., Dalton, J. B., McDougal, R.R., and Gent, C. A., 2003, Imaging spectroscopy: Earth and planetary remote sensing with the USGS Tetracorder and expert systems: The Journal of Geophysical Research, v.108, no. E12, 5131, doi:10.1029/2002JE001847.

Clark, R.N., Swayze, G.A., Wise, R., Livo, E., Hoefen, T., Kokaly, R., Sutley, S.J., 2007, USGS digital spectral library splib06a: U.S. Geological Survey, Digital Data Series 231. (http://speclab.cr.usgs.gov/spectral.lib06)

Crowley, J.K., and Vergo, N., 1988, Near-infrared reflectance spectra of mixtures of kaolin-group minerals: use in clay mineral studies: Clays and Clay Minerals, v. 36, no. 4, p. 310-316.

Cruz-Cumplido, M., Sow, C. and Fripiat, J.J., 1982, Spectre infrarouge des hydroxyles, cristallinité et énergie de cohésion des kaolins: Bulletin de Minéralogie, v. 105, p. 493-498.

Cudahy, T.J., Okada, K., Ueda, K., Brauhart, C., Morant, P., Huston, D., Cocks, T., Cocks, P., Wilson, J., Ong. C., Mason, P., and Huntington, J.F., 1999, Mapping the Panorama VMS-style alteration and host rock mineralogy, Pilbara Block, using airborne hyperspectral VNIR-SWIR data: CSIRO Exploration and Mining Report 661F, 86p.

Cudahy, T., Hewson, R., Caccetta, M., Roache, A., Whitbourn, L., Connor, D., Mason, P., Yang, K., Huntington, J., Quigley, M., 2009, Drill core logging of plagioclase feldspar composition and other minerals associated with Archean gold mineralization at Kambalda, Western Australia, using a bidirectional thermal infrared reflectance system, *in* Bedell, R., Crósta, A.P., and Grunsky, E., eds., Remote Sensing and Spectral Geology: Reviews in Economic Geology, v. 16, p. 223-235.

Ducart, D.F., Crósta, A.P., Souza Filho, C.R., 2006, Alteration mineralogy at the Cerro La Mina Epithermal Prospect, Patagonia, Argentina: Field mapping, short-wave infrared spectroscopy, and ASTER images: Economic Geology, v. 101, no. 5, p. 981-996.

Duke, E.F., 1994, Near infrared spectra of muscovite, Tschermak substitution, and metamorphic reaction progress: implications for remote sensing: Geology, v. 22, p. 621-624.

Duke, E.F., and Lewis, R.S., 2010, Near infrared spectra of white mica in the Belt Supergroup and implications for metamorphism: American Mineralogist, v. 95, p. 908-920.

Dalrymple, G.B., Alexander, E.C., Lanphere, M.A., and Kraker, G.P., 1981, Irradiation of samples for $^{40}Ar/^{39}Ar$ dating using the Geological Survey TRIGA reactor: U.S. Geological Survey Professional Paper 1176, 55p.

Deyell, C.L., and Dipple, G.M., 2005, Equilibrium mineral-fluid calculations and their application to the solid solution between alunite and natroalunite in the El Indio-Pascua

belt of Chile and Argentina: Chemical Geology, v. 215, p. 219-234.
Deyell, C.L., Rye, R.O., Landis, G.P., Bissig, T., 2005, Alunite and the role of magmatic fluids in the Tambo high-sulfidation deposit, El Indio-Pascua belt, Chile: Chemical Geology, v. 215, p. 185-218.
Ebert, S.W., and Groves, D.I., 1996, Geology, alteration, and ore controls of the Crofoot/Lewis Mine, Sulphur , Nevada: A well-preserved hot-spring gold-silver deposit, *in* Coyner, A.R. and Fahey, P.L., eds., Geology and Ore Deposits of the American Cordillera, Symposium Proceedings, v. 1: Geological Society of Nevada, Reno, Nevada, p. 209-234.
Farmer, V.C., 1964, Infrared absorption of hydroxyl groups in kaolinite: Science, v. 145, p. 1189-1190.
Farmer, V.C., 1974, The Infrared Spectra of Minerals: Mineralogical Society, London, 539 p.
Farrand, W.H., Glotch, T.D., Rice, J.W., Hurowitz, J.A., and Swayze, G.A., 2009, Discovery of jarosite-bearing sediment within the Mawrth Vallis region of Mars: Implications for the geologic history of the region: Icarus, v. 204, no.2, p. 478-488.
Felzer, B., Hauff, P., and Goetz, A.F.H, 1994, Quantitative reflectance spectroscopy of buddingtonite from the Cuprite mining district, Nevada: Journal of Geophysical Research, v. 99, no. B2, p. 2887-2895.
Fialips, C.-I., Petit, S., Decarreau, A., and Beaufort, D., 2000, Influence of synthesis pH on kaolinite "crystallinity" and surface properties: Clays and Clay Minerals: v. 48, no. 2, p. 173-184.
Fleck, R.J., Turrin, B.D., Sawyer, D.A., Warren, R.G., Champion, D.E., Hudson, M.R., and Minor, S.A., 1996, Age and character of basaltic rocks of the Yucca Mountain region, southern Nevada: Journal of Geophysical Research, v. 101, no. B4, p. 8205-8227.
Foley, D., 1978, The geology of the Stonewall Mountain volcanic center, Nye County, Nevada: Ph.D. dissertation, Ohio State University, Columbus, 139 p.
Fournier, R.O., 1985, The behavior of silica in hydrothermal solutions, *in* Berger, R.R., and Bethke, P.M., eds., Geology and Geochemistry of Epithermal Systems, Society of Economic Geologists: Reviews in Economic Geology, v. 2, p. 45-62.
Gulbrandsen, R.A., 1974, Buddingtonite, ammonium feldspar, in the Phosphoria Formation, southeastern Idaho: USGS Journal of Research, v. 2, no. 6, p. 693-697.
Gao, B-C, Heidebrecht, K.B., and Goetz, A.F.H., 1993, Derivation of scaled surface reflectances from AVIRIS data, Remote Sensing of Environment, v. 44, no. 2, p. 165-178.
Giggenbach, W.F., 1992, Isotopic shifts in waters from geothermal and volcanic systems along convergent plate boundaries and their origin: Earth and Planetary Science Letters, v. 113, issue 4, p. 495-510.
Goetz, A.F.H., and Strivastava, V., 1985, Mineralogical mapping in the Cuprite mining district, *in* Vane, G., and Goetz, A.F.H., eds., Proceedings of the Airborne Imaging Spectrometer (AIS) Data Analysis Workshop: Jet Propulsion Laboratory Publication 85-41, p. 22-29.
Goetz, A.F.H., Vane, G., Solomon, J.E., and Rock, B.N., 1985, Imaging spectrometry for Earth remote sensing: Science, v. 228, p. 1147-1153.
Graetsch, H., 1994, Structural characteristics of opaline and microcrystalline silica minerals, *in* Heaney, P.J., Prewitt, C.T., and Gibbs, G.V., eds., Reviews in Mineralogy, Silica: Physical Behavior, Geochemistry and Materials Applications: Mineralogical Society of America, v. 29, p. 209-232.
Grauch, V.J.S., Sawyer, D.A., Fridrich, C.J., and Hudson, M.R., 1999, Geophysical framework

of the Southwestern Nevada Volcanic Field and hydrogeologic implications: U.S. Geological Survey Professional Paper 1608, 39 p.

Green, R.O., Eastwood, M.L., Sarture, C.M., Chrien, T.G., Aronsson, M., Chippendale, B.J., Faust, J.A., Pavri, B.E., Chovit, C.J., Solis, J., Olah, M.R., Williams, O., 1998, Imaging spectroscopy and the Airborne Visible/Infrared Imaging Spectrometer (AVIRIS): Remote Sensing of Environment, v. 65, p. 227-248.

Haest, M., Cudahy, T., Laukamp, C., Gregory, S., 2012, Quantitative mineralogy from visible to shortwave infrared spectroscopic data - II. 3D mineralogical characterisation of the Rocklea Dome channel iron deposit, Western Australia: Economic Geology, v. 107, p. 229 - 249.

Hallam, M. and Eugster, H.P., 1976, Ammonium silicate stability relations: Contributions to Mineral Petrology, v. 57, p. 227-244.

Hausback, B.P., Deino, A.L., Turrin, B.T., McKee, E.H., Frizzell, V. A., Jr., Noble, D.C., Weiss, S.I., 1990, New $^{40}Ar/^{39}Ar$ ages for the Spearhead and Civet Cat Canyon Members of the Stonewall Flat Tuff, Nye County, Nevada - evidence for systematic errors in standard K-Ar age determinations on sanidine: Isochron/West (December), no. 56, p. 3-7.

Harraden, C.L., McNulty, B.A., Gregory, M.J., and Lang, J.R., 2013, Shortwave infrared spectral analysis of hydrothermal alteration associated with the Pebble Porphyry copper-gold-molybdenum deposit, Iliamna, Alaska: Economic Geology, v. 108, p. 483-494.

Hayba, D.O., Bethke, P.M., Heald, P. and Foley, N.K., 1985, The geological, mineralogical and geochemical characteristics of volcanic-hosted epithermal deposits, *in* Berger, B.R., and Bethke, P.M., eds., Geology and Geochemistry of Epithermal Systems, Society of Economic Geologists: Reviews in Economic Geology, v. 2, p. 129-168.

Hedenquist, J.W., Matsuhisa, Y., Izawa, E., White, N.C., Giggenbach, W.F., and Aoki, M., 1994, Geology, geochemistry, and origin of high sulfidation Cu-Au mineralization in the Nansatsu District, Japan: Economic Geology, v. 89, p. 1-30.

Hedenquist, J., Arribas, A.R., and Gonzalez-Urien, E., 2000, Exploration for epithermal gold deposits: Reviews in Economic Geology, v. 13, p. 245-277.

Hearny, P.J., 1994, Structure and chemistry of the low-pressure silica polymorphs, *in* Heaney, P.J., Prewitt, C.T., and Gibbs, G.V., eds., Reviews in Mineralogy, Silica: Physical Behavior, Geochemistry and Materials Applications: Mineralogical Society of America, v. 29, p. 1-40.

Herrmann, W., Blake, M., Doyle, M., Huston, D., Kamprad, J., Merry, N., and Pontual, S., 2001, Short wavelength infrared (SWIR) spectral analysis of hydrothermal alteration zones associated with base metal sulfide deposits at Rosebery and western Tharsis, Tasmania, and Highway-Reward, Queensland: Economic Geology, v. 96, p. 939-955.

Hunt, G.R., 1977, Spectral signatures of particulate minerals in the visible and near infrared: Geophysics, v. 42, no. 3, p. 501-513.

Hunt, G.R., and Ashley, R.P., 1979, Spectra of altered rocks in the visible and near infrared: Economic Geology, v. 74, p. 1613-1629.

Hunt, G.R., and Salisbury, J.W., 1970, Visible and near-infrared spectra of minerals and rocks: I silicate minerals: Modern Geology, v. 1, p. 283-300.

Hunt, G.R., Salisbury, J.W., and Lenhoff, C.J., 1971, Visible and near-infrared spectra of minerals and rocks: IV. Sulphides and sulphates: Modern Geology, v. 3, p. 1-14.

Hurlbut, C.S., Jr., and Klein, C., 1977, Manual of Mineralogy (after J.D. Dana), 19th Edition:

John Wiley & Sons, New York, 532 p.
Johnston, C.T., Kogel, J.E., Bish, D.L., Kogure, T., and Murray, H.H., 2008, Low-temperature FTIR study of kaolin-group minerals: Clays and Clay Minerals, v. 56, no. 4, p. 470-485.
Joussein, E., Petit, S., Churchman, J., Theng, B., Righi, D., and Delvaux, B., 2005, Halloysite clay minerals – a review: Clay Minerals, v. 40, p. 383-426.
Kerr, A., Rafuse, H, Sparkes, G., Hinchey, J., and Sandeman, H., 2011, Visible/Infrared Spectroscopy (VIRS) as a research tool in economic geology: background and pilot studies from Newfoundland and Labrador: Current Research (2011) Newfoundland and Labrador Department of Natural Resources Geological Survey, Report 11-1, p. 145-166.
Kruse, F.A., Keirein-Young, K.S., and Boardman, J.W., 1990, Mineral mapping at Cuprite, Nevada with a 64-channel imaging spectrometer: Photogrammetric Engineering and Remote Sensing, v. 56, no. 1, p. 83-92.
Kruse, F.A., Bidell, R.L., Taranik, J.V., Peppin,W.A., Weatherbee, O., and Calvin, W.M., 2011, Mapping alteration minerals at prospect, outcrop, and drill core scales using imaging spectrometry: International Journal of Remote Sensing, v. 33, no. 6, p. 1780-1798, DOI:10.1080/01431161.2011.600350.
Kogure, T., Elzea-Kogel, J., Johnston, C.T., and Bish, D.L., 2010, Stacking disorder in a sedimentary kaolinite: Clays and Clay Minerals, v. 58, no. 1, p. 62-71.
Landis, G.P., Snee, L.W., and Juliani, C., 2005, Evaluation of argon ages and integrity of fluid-inclusion compositions: stepwise noble gas heating experiments on 1.87 Ga alunite from Tapajos Province, Brazil: Chemical Geology, v. 215, p. 127-153.
Langer, K. and Flörke, O.W., 1974, Near infrared absorption spectra (4000-9000 cm^{-1}) of opals and the role of "water" in these $SiO_2 \bullet nH_2O$ minerals: Fortschritte der Mineralogie, v. 52, no. 1, p. 17-51.
Longhi, I., Mazzoli, C., and Sgavetti, M., 2000, Determination of metamorphic grade in siliceous muscovite-bearing rocks in Madagascar using reflectance spectroscopy: Terra Nova, v. 12, p. 21-27.
Loughnan F.C., Roberts, F.I., and Lindner, A.W., 1983, Buddingtonite (NH_4-feldspar) in the Condor Oilshale Deposit, Queensland, Australia: Mineralogical Magazine, v. 47, no. 344, p. 327-334.
Madejova, J., Kraus, I., Tunega, D., and Samajova, E., 1997, Fourier transform infrared spectroscopic characterization of kaolin group minerals from the main Slovak deposits: Geologica Carpathica Clays, v. 6, no. 1, p. 3-10.
Mars, J.C., and Rowan, L.C., 2006, Regional mapping of phyllic- and argillic-altered rocks in the Zagros magmatic arc, Iran, using Advanced Spaceborne Thermal Emission and Reflection Radiometer (ASTER) data and logical operator algorithms: Geosphere, v. 2; no. 3; p. 161-186, DOI: 10.1130/GES00044.1.
Mars, J.C., and Rowan, L.C., 2010, Spectral assessment of new ASTER SWIR surface reflectance data products for spectroscopic mapping of rocks and minerals: Remote Sensing of Environment, v. 114, no. 9, p. 2011-2025.
Martinez-Alonso, S.E., Rustad, J., Bianco, R., and Goetz, A.F.H., 2002, *Ab initio* quantum mechanical modeling of infrared vibrational frequencies of the OH group in dioctahedral phyllosilicates: Part II, Main physical factors governing the OH vibrations: American Mineralogist, v. 87, p. 1224-1234.
Milliken, R.E., Swayze, G.A., Arvidson, R.E., Bishop, J.L., Clark, R.N., Ehlmann, B.L., Green,

R.O., Grotzinger, J.P., Morris, R.V., Murchie, S., Mustard, J.F., Weitz, C., and the CRISM Science Team, 2008, Opaline silica in young deposits on Mars: Geology, v.36, no. 11, p. 847-850.

Noble, D.C., Korringa, M.K., Church, S.E., Bowman, H.R., Silberman, M.L., and Heropoulos, C.E., 1976, Elemental and isotopic geochemistry of nonhydrated quartz latite glasses from the Eureka Valley Tuff, east-central California: Geological Society of America Bulletin, v. 87, p. 754 - 762.

Noble, D.C., T.A. Vogel, S.I. Weiss, J.W. Erwin, E.H. McKee, and L.W. Younker, 1984, Stratigraphic relations and source areas of ash-flow sheets of the Black Mountain and Stonewall Mountain Volcanic Centers, Nevada: Journal of Geophysical Research, v. 89, no. B10, p. 8593-8602.

Noble, D.C., McKee, E.H., and Weiss, S.I., 1988, Nature and timing of pyroclastic and hydrothermal activity and mineralization at the Stonewall Mountain volcanic center, southwestern Nevada: Isochron/West, no. 51, p. 25 - 28.

Oldow, J.S., Kohler, G., and Donelick, R.A., 1994, Late Cenozoic extensional transfer in the Walker Lane strike-slip belt, Nevada: Geology, v. 22, p. 637-640.

Ong, C., G. Swayze, and R. Clark, 2003, An investigation of the use of the Tetracorder expert system for multi-temporal mapping of acid drainage-related minerals using airborne hyperspectral data: Proceedings of the 3rd EARSel Workshop on Imaging Spectroscopy, May 13-16, 2003, Herrsching, Germany, p. 357-362.

Queralt, I., Kanazirski, M., and Gorova, M., 1995, Adularia-sericite type wallrock alteration at the María Josefa gold mine: An example of low sulfidation epithermal ore deposit, within the volcanic Rodalquilar Caldera (SE, Spain): Acta Geologica Hispanica, v. 20, no. 4, p. 91-100.

Papin, A., Sergent, J., and Robert, J.-L., 1997, Intersite OH-F distribution in an Al-rich synthetic phlogopite: European Journal of Mineralogy, v. 9, p. 501-508.

Post, J.L., and Borer, L., 2002, Physical properties of selected illites, beidellites and mixed-layer illite-beidellites from southwestern Idaho and their infrared spectra: Applied Clay Science, v. 22, p. 77-91.

Post, J.L., and Noble, P.N., 1993, The near-infrared combination band frequencies of di-octahedral smectites, micas, and illites: Clays and Clay Minerals, v. 41, no. 6, p. 639-644.

Ransome, F.L., 1909, The geology and ore deposits of Goldfield, Nevada: U.S. Geological Survey Professional Paper 66, 258 p.

Reyes, A.G., 1991, Mineralogy, distribution and origin of acid alteration in Philippine geothermal systems: Geological Survey of Japan Report, v. 277, p. 59-65.

Reynolds, R.C., and Bish, D.L., 2002, The effects of grinding on the structure of a low-defect kaolinite: American Mineralogist, v. 87, p. 1626-1630.

Rockwell, B.W., Cunningham, C.G., Breit, G.N., and Rye, R.O., 2006, Spectroscopic mapping of the White Horse Alunite Deposit, Marysvale Volcanic Field, Utah: Evidence of a magmatic component: Economic Geology, v. 101, p. 1377-1395, doi:10.2113/gsecongeo.101.7.1377.

Roddick, J.C., 1983, High precision intercalibration of $^{40}Ar/^{39}Ar$ standards: Geochimica et Cosmochimica Acta, v. 47, p. 887-898.

Rossman, G.R., 1984, Spectroscopy of micas, in Bailey, S.W., ed., Micas: Mineralogical Society of America Reviews in Mineralogy, v. 13, p. 145-181.

Rowan, L.C., Wetlaufer, P.H., Goetz, A.F.H., Billingsley, F.C., and Stewart, J.H., 1974, Discrimination of Rock Types and Detection of Hydrothermally Altered Areas in South-Central Nevada by the use of Computer Enhanced ERTS Images: U.S. Geological Survey Professional Paper 883, 35 p.

Rowan, L., Hook, S., Abrams, M., and Mars, J., 2003, Mapping hydrothermally altered rocks at Cuprite, Nevada using the Advanced Spaceborne Thermal Emission and Reflectance Radiometer (ASTER), a new satellite imaging system: Economic Geology, v. 98; no. 5; p. 1019-1027; doi: 10.2113/98.5.1019.

Rye, R.O., Bethke, P.M., and Wasserman, M.D., 1992, The stable isotope geochemistry of acid sulfate alteration: Economic Geology, v. 87, no. 2, p. 225-262.

Sainz-Diaz, C.I., Timon, V., Botella, V., and Hernandez-Laguna, A., 2000, Isomorphous substitution effect on the vibration frequencies of hydroxyl groups in molecular cluster models of the clay octahedral sheet: American Mineralogist, v. 58, p. 1038-1045.

Saksena, B.D., 1964, Infrared hydroxyl frequencies of muscovite, phlogopite and biotite micas in relation to their structures: Journal of the Chemical Society, Faraday Transactions, v. 60, p. 1715-1725.

Samson, S.D., and Alexander, E.C., 1987, Calibration of interlaboratory $^{40}Ar/^{39}Ar$ dating standards Mmhb-1: Isotope Geoscience, v. 66, p. 27-34.

Sharp, Z.D., Atudorei, V., Durakiewicz, T., 2001, A rapid method for determination of hydrogen and oxygen isotope ratios from water and hydrous minerals: Chemical Geology, v.178, p. 197-210.

Silberman, M.L., and McKee, E.H., 1972, A summary of radiometric age determinations from Nevada and eastern California – Part II, western Nevada: Isochron/West, no. 4, p. 7-28.

Sillitoe, R.H., and Hedenquist, J.W., 2003, Linkages between volcanotectonic settings, ore-fluid composition, and epithermal precious metal deposits: Society of Economic Geologists Special Publication 10, p. 315-343.

Snee, L.W., 2002, Argon thermochronology applied to mineral deposits - a review of analytical methods, formulations, and selected applications: U.S. Geological Survey Bulletin B2194, 39 p.

Steiger, R.H., and Jäger, E., 1977, Subcommission on geochronology – Convention on the use of decay constants in geo- and cosmochronology: Earth and Planetary Science Letters, v. 36, p. 359-362.

Stewart, J.H., 1988, Tectonics of the Walker Lane Belt, Western Great Basin - Mesozoic and Cenozoic deformation in a zone of shear, *in* Ernst, W.G., ed., Metamorphism and Crustal Evolution of the Western United States, VII: Englewood Cliffs, New Jersey, Prentice-Hall, p. 684-713.

Stoffregen, R.E., and Alpers, C.N., 1992, Observations on the unit-cell dimensions, H_2O contents, and δD values of natural and synthetic alunite: American Mineralogist, v. 77, p. 1092-1098.

Stoffregen, R.E. and Cygan, G. L., 1990, An experimental study of Na-K exchange between alunite and aqueous sulfate solutions: American Mineralogist, v. 75, p. 209-220.

Stoffregen, R.E., Rye, R.O., and Wasserman, D.O., 1994, Experimental studies of alunite 1: ^{18}O-^{16}O and D-H fractionation factors between alunite and water at 250°C – 450°C: Geochimica et Cosmochimica Acta, v. 58, p. 903-916.

Swayze, G.A., 1997, The hydrothermal and structural history of the Cuprite Mining District,

southwestern Nevada: an integrated geological and geophysical approach: unpublished Ph. D. Dissertation, University of Colorado Boulder, 399 p.

Swayze, G.A., R.N. Clark, F. Kruse, S. Sutley, and A. Gallagher, 1992, Ground-truthing AVIRIS mineral mapping at Cuprite, Nevada, *in* Green, R.O., ed., Summaries of the Third Annual JPL Airborne Geosciences Workshop, Volume 1: JPL Publication 92-14, p. 47-49.

Swayze, G.A., K.S. Smith, R.N. Clark, S.J. Sutley, R.N. Pearson, G.S. Rust, J.S. Vance, P.L. Hageman, P.H. Briggs, A.L. Meier, M.J. Singleton, and S. Roth, 2000, Using imaging spectroscopy to map acidic mine waste: Environmental Science and Technology, v. 34, no. 1, p. 47-54.

Swayze, G.A., Clark, R.N., Sutley, S.J., Gent, C.A., Rockwell, B.W., Blaney, D.L., Post, J.L., and Farm, B.P., 2002, Mineral mapping Mauna Kea and Mauna Loa Shield Volcanos on Hawaii using AVIRIS data and the USGS Tetracorder spectral identification system: Lessons applicable to the search for relict Martian hydrothermal systems, *in* Green, R.O., ed., Proceedings of the 11th JPL Airborne Earth Science Workshop: Jet Propulsion Laboratory Publication 03-4, p. 373-387.

Swayze, G.A., Clark, R.N., Goetz, A.F.H., Chrien, T.G., and Gorelick, N.S., 2003, Effects of spectrometer band pass, sampling, and signal-to-noise ratio on spectral identification using the Tetracorder algorithm, Journal of Geophysical Research v. 108, no. E9, 5105, doi: 10.1029/2002JE001975.

Swayze, G.A., Desborough, G.A., Clark, R.N., Rye, R.O., Stoffregen, R.E., Smith, K.S., and Lowers, H.A., 2006, Detection of jarosite and alunite with hyperspectral imaging: prospects for determining their origin on Mars using orbital sensors: Workshop on Martian Sulfates as Recorders of Atmospheric-Fluid-Rock Interactions, Lunar and Planetary Institute, 7072.pdf.

Swayze, G.A., Desborough, G.A., Smith, K.S., Lowers, H.A., Hammerstrom, J.M., Diehl, S.F., Leniz, R.W., and Driscoll, R.L., 2008a, Chapter B: Understanding jarosite – from mine waste to Mars, *in* Verplank, P.L., ed., Understanding Contaminants Associated With Mineral Deposits: U.S. Geological Survey Circular 1320, p. 8-13.

Swayze, G.A., Ehlmann, B.L., Milliken, R.E., Poulet, F., Wray, J.J., Rye, R.O., Clark, R.N., Desborough, G.A., Crowley, J.K., Gondet, B., Mustard, J.F., Seelos, K.D., Murchie, S.L., and the MRO CRISM team, 2008b, Discovery of the acid-sulfate mineral alunite in Terra Sirenum, Mars, using MRO CRISM: possible evidence for acid-saline lacustrine deposits?: Eos Trans. AGU 89(53), Fall Meet. Suppl. Abstract P44A-04.

Taggart, J.E. and Siems, D.F., 2002, Major elemental analysis by wavelength dispersive x-ray fluorescence spectrometry: U.S. Geological Survey Open File Report 02-223-T, 9 p.

Taylor, B.E., 1992, Degassing of H_2O from rhyolitic magma during eruption and shallow intrusion, and the isotopic composition of magmatic water in hydrothermal systems: Geological Survey of Japan Report 279, p. 190-194.

Thompson, A.J.B., Hauff, P.L., and Robitaille, A.J., 1999, Alteration mapping in exploration–application of short-wave infrared (SWIR) spectroscopy: Society of Economic Geologists Newsletter 39, p. 1, 16 - 27.

Thompson, A., Scott, K., Huntington, J., and Yang, K., 2009, Mapping mineralogy with reflectance spectroscopy: examples from volcanogenic massive sulfide deposits, *in* Bedell, R., Crósta, A.P., and Grunsky, E., eds., Remote Sensing and Spectral Geology: Reviews in Economic Geology, v. 16, p. 25-40.

van Ruitenbeek, F.J.A., Cudahy, T., Hale, M., and van der Meer, F.D., 2005, Tracing fluid pathways in fossil hydrothermal systems with near-infrared spectroscopy: Geology, v. 33, no. 7, p. 597-600, doi: 10.1130/G21375.1.

Vasconcelos, P.M., Brimhall, G.H., Becker, T.A., and Renne, P.R., 1994, $^{40}Ar/^{39}Ar$ analysis of supergene jarosite and alunite: implications to the paleoweathering history of the western USA and West Africa: Geochimica et Cosmochimica Acta, v. 58, p. 401-420.

Vikre, P.G., 1998, Intrusion-related polymetallic carbonate replacement deposits in the Eureka District, Eureka County, Nevada: Nevada Bureau of Mines and Geology, Bulletin 110, 52 p.

Wasserman, M.D., Rye, R.O., Bethke, P.M., Arribas, A. Jr., 1992, Methods for separation and total stable isotope analysis of alunite: U.S. Geological Survey Open-File Report 92-9, 20 p.

Weiss, S.I., and Noble, D.C., 1989, Stonewall Mountain Volcanic Center, Southern Nevada: stratigraphic, structural, and facies relations of outflow sheets, near-vent tuffs, and intracaldera units: Journal of Geophysical Research, v. 94, p. 6059-6074.

Weiss, S.I., Noble, D.C., Worthington, J.E. IV, 1993, Neogene tectonism from the Southwestern Nevada Volcanic Field to the White Mountains, California: Part I. Miocene volcanic stratigraphy, paleotopography, extensional faulting and uplift between Northern Death Valley and Pahute Mesa, *in* Lahren, M.M., Trexler, J.H., Jr., and Spinosa, C., eds., Crustal Evolution of the Great Basin and Sierra Nevada: Geological Society of America Guidebook, Department of Geological Sciences, University of Nevada, Reno, p. 352-382.

White, N.C., and Hedenquist, J.W., 1995, Epithermal gold deposits: styles, characteristics and exploration: SEG Newsletter, no. 23, p. 1, 9-13.

Wray, J.J., Milliken, R.E., Dundas, C.M., Swayze, G.A., Andrews-Hanna, J.C., Baldridge, A.M., Chojnacki, M., Clark, R.N., Murchie, S.L., Ehlmann, B.L., Bishop, J.L., Seelos, F.P., Tornabene, L.L., Squyers, S.W., 2011, Columbus Crater and other possible groundwater-fed paleolakes of Terra Sirenum, Mars: Journal of Geophysical Research, v. 116, E01001, doi:10.1029/2010JE003694, 41p.

Yang, K., Huntington, J.F., Boardman, J.W., and Mason, P., 1999, Mapping hydrothermal alteration in the Comstock mining district, Nevada, using simulated satellite-borne hyperspectral data: Australian Journal of Earth Sciences, v. 46, p. 915-922.

Yang, K. Browne, P.R.L., Huntington, J.F., and Walshe, J.L., 2001, Characterising the hydrothermal alteration of the Broadlands – Ohaaki geothermal system, New Zealand, using short-wave infrared spectroscopy: Journal of Volcanology and Geothermal Research, v. 106, p. 53-65.

Yang, K., Huntington, J.F., Gemmell, J.B., and Scott, K.M., 2011, Variations in composition and abundance of white mica in the hydrothermal alteration system at Hellyer, Tasmania, as revealed by infrared reflectance spectroscopy: Journal of Geochemical Exploration, v. 108, p. 143-156, doi: 10.1016/j.gexplo.201.01.001.

Zohdy, A.A.R., 1989, A new method for the automatic interpretation of Schlumberger and Wenner sounding curves: Geophysics, v. 54, no. 2, p. 245-253.

Zohdy, A.A.R, Eaton, G.P., and Mabey, D.R., 1974, Application of surface geophysics to ground-water investigations, *in* Techniques of Water-Resources Investigations for the United States Geological Survey, Book 2, Collection of Environmental Data: U.S. Geological Survey, Washington D.C., 66 p.

dickite relative stability at 150-300°C and the thermodynamic properties of dickite: American Mineralogist, v. 83, p. 516-524.

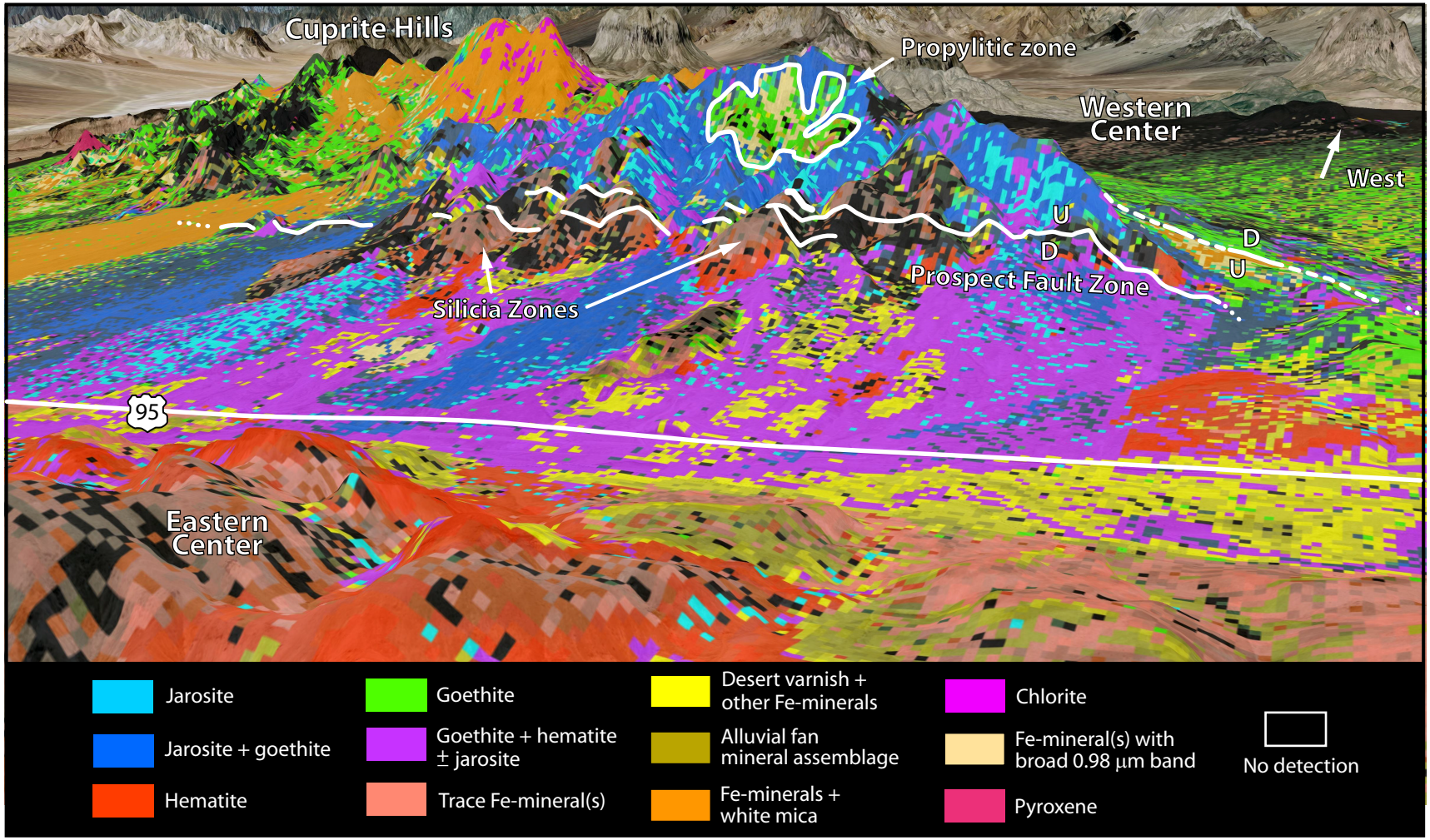

Fig. A1. 3-D view of 1-µm region electronic mineral map draped on Google™ Earth topography looking SW toward the western center at Cuprite (3x vertical exaggeration). Position of faults from Figure 3A. AVIRIS image does not extend to mountains west of the Cuprite Hills area so colors there are from Google™ Earth base images.

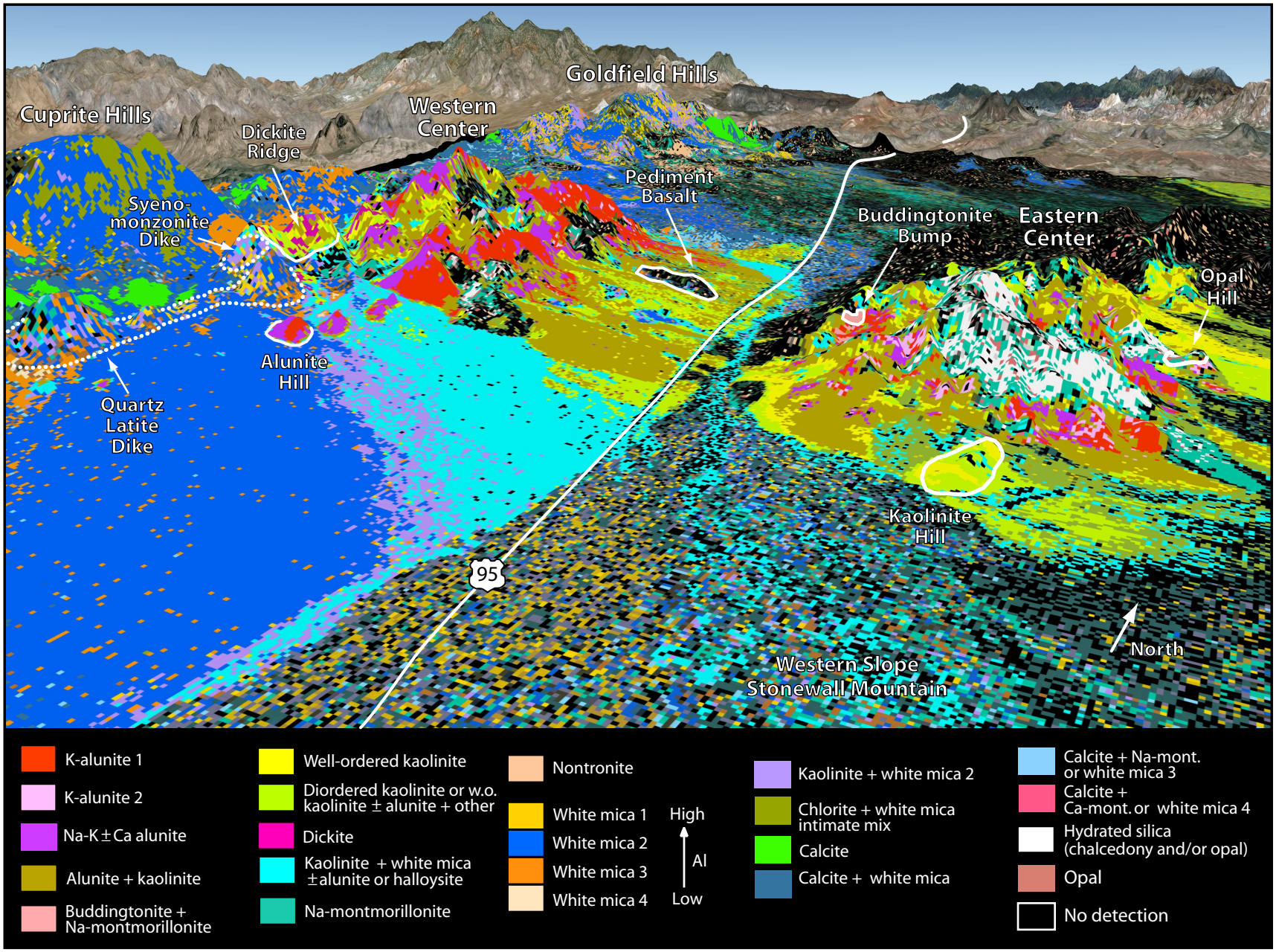

Fig. A2. 3-D view of 2-µm region vibrational mineral map draped on Google™ Earth topography looking NW toward Cuprite alteration centers (3x vertical exaggeration). Position of faults from Figure 3A; dotted lines show approximate location of intrusive rocks. w.o. = well-ordered. AVIRIS image does not extend to mountains northwest of the Cuprite and Goldfield Hills areas so colors there are from Google™ Earth base images.

Table A1. Field sample verification of mineralogy derived from Tetracorder mapping.

Spectral category (map code)	Sample ID	Sample location (NAD27 Datum)		Tetracorder mapping results spectral regions		Sample verification
				electronic (1 μm)	vibrational (2 μm)	
(See Figure 5A)						
Jarosite (1A)	CU91-20A	N37° 33' 12" W117° 10' 33"	N part Ectr	Jarosite	Alunite + kaolinite	XRD of coating: K-jarosite. LS: jarosite in coating
Hematite (3B)	CU91-223A	N37° 33' 05" W117° 10' 41"	NW part of Ectr	Hematite	Kaolinite	XRD: disordered hematite, kaolinite, quartz, calcite, and tridymite (tr)? LS: hematite and kaolinite
Goethite (4C)	CU91-236A	N37° 32' 32" W117° 13' 24"	Central part Wctr along W margin	Goethite	w.o. kaolinite + white mica [/1] or halloysite [/2]	XRD: goethite, kaolinite, quartz LS: goethite, w.o. kaolinite, dickite
Chlorite (5D)	CU91-238A	N37° 31' 49" W117° 13' 56"	SW part of Wctr	Chlorite	Chlorite + white mica	XRD: Fe-chlorite, muscovite, quartz, and kaolinite LS: chlorite and white mica
Pyroxene (6E)	CU01-20A	N37° 29' 07" W117° 14' 29" (GPS)	S of Wctr (basalt plug)	Pyroxene	N.D.	XRD: augite (M), diopside (M), anorthite (M), forsterite (tr),quartz (tr),analcime(tr) LS: pyroxene + trace hydrated phases
(See Figure 5B)						
K-alunite 1 (7F)	CU91-217G	N37° 31' 27" W117° 12' 43"	Alunite Hill, SW part of Wctr	Goethite	K-alunite (wide band)	XRD: K-alunite and quartz XRF: alunite Na/K = 0.05 LS: K-alunite Na/K = 0.01
K-alunite 2 (8G)	CU98-5C	N37° 32' 05.2" W117° 10' 11.6" (GPS)	SE part of Ectr	Trace Fe-mineral	K-alunite	XRD: alunite (M), opal-A (M), tridymite (m), and quartz (tr) LS: K-alunite Na/K = 0.07

Spectral category (map code)	**Sample ID**	**Sample location** (NAD27 Datum)		**Tetracorder mapping results spectral regions**		**Sample verification**
				electronic (1 μm)	**vibrational (2 μm)**	
Na-K±Ca alunite (9H)	CU91-217H	N37° 31' 26" W117° 12' 41"	Alunite hill, SW part of Wctr	N.D.	Multiple component alunite	EM: K, Ca, and Na components XRD: Na-alunite and quartz XRF: alunite Na/K = 0.64 bulk comp. LS: multiple alunite components Na/K alunite 1 = 0.08 alunite 2 = 1.03
Buddingtonite + Na-montmorillonite (11I)	CU91-260B	N37° 32' 35" W117° 11' 10"	Buddingtonite bump, W central Ectr	Jarosite[/3]	Buddingtonite ± Na-montmorillonite	XRD: buddingtonite in solid-solution with K-feldspar, also quartz LS: buddingtonite and Na-montmorillonite
Well ordered (w.o.) kaolinite (12J)	CU91-200A	N37° 31' 36" W117° 10' 29"	Kaolinite hill, S part of Ectr	N.D.	w.o. kaolinite	XRD: w.o. kaolinite, quartz, feldspar, and alunite LS: w.o. kaolinite
Disordered kaolinite or w.o. kaolinite ± alunite + other (13K)	CU00-19A	N37° 32' 05" W117° 11' 03" (GPS)	SW part of Ectr	Hematite	Disordered kaolinite or w.o. kaolinite ± alunite + other	XRD: clay separate contains w.o. kaolinite, smectite (tr), and illite (tr) LS: Hematite, disordered kaolinite or w.o. kaolinite + white mica/smectite
Dickite (14L)	CU91-219B	N37° 31' 54" W117° 13' 18"	Dickite ridge, SW part of Wctr	Jarosite [/3] +goethite	Dickite	XRD: dickite, kaolinite, quartz, calcite LS: dickite
Kaolinite + white mica ± alunite or halloysite (15P)	CU91-242D	N37° 32' 04" W117° 13' 11"	SW part of Wctr	Jarosite[/3] +goethite	Kaolinite + white mica ± alunite or halloysite	XRD: halloysite, quartz, mica, alunite, possibly dickite LS: trace goethite, halloysite or w.o. kaolinite + white mica/smectite
Na-montmorillonite (16Q)	CU93-52	N37° 31' 51" W117° 09' 25"	Stonewall playa	Desert varnish + other Fe-minerals	Na-montmorillonite[/4]	XRD: quartz (M), anorthite (m), albite (m), calcite (m), orthoclase (m), muscovite (m), montmorillonite (m), kaolinite (tr), magnesiohornblende (tr) LS: Na-montmorillonite

Spectral category (map code)	**Sample ID**	**Sample location** (NAD27 Datum)		**Tetracorder mapping results spectral regions** electronic (1 μm)	vibrational (2 μm)	**Sample verification**
Nontronite (17R)	CU00-13A	N37° 35' 52" W117° 14' 04" (GPS)	4 km NW of Wctr	Goethite	Nontronite[/5]	XRD: clay separate contains smectite[/6] (M), kaolinite (tr), mica (tr) LS: nontronite
High-Al white mica 1 (18S)	CU00-5B	N37° 31' 39" W117° 13' 11" (GPS)	S part of Wctr	Goethite	High Al-white mica[/7] Al^{oct} = 1.835	XRD: quartz (M), Illite (both 1M and 2M2 polytypes) EM: high Al-illite Al^{oct} = 1.836 LS: high Al-white mica Al^{oct} = 1.845
Medium high Al-white mica 2 (19T)	CU91-252D	N37° 31' 45" W117° 13' 46"	SW part of Wctr	Fe-minerals + muscovite	Med. high Al-white mica Al^{oct} = 1.795	XRD: quartz (M), muscovite (mostly 2M1 with trace 1M polytypes), clinochlore (tr) EM: med. high Al-muscovite Al^{oct}=1.789 LS: med. high Al-white mica Al^{oct}=1.783
Medium low Al-white mica 3 (20U)	CU91-250A	N37° 31' 46" W117° 13' 31"	SW part of Wctr	Fe-minerals + muscovite	med. low Al-white mica Al^{oct} = 1.701	XRD: quartz (M), muscovite (both 2M1 and 1M polytypes) EM: med. low Al-muscovite Al^{oct}= 1.762 LS: med. low Al-white mica Al^{oct} = 1.707
Low Al-white mica 4 (21V)	CU98-8H	N37° 33' 30.8" W117° 12' 59.4" (GPS)	N part of Wctr	Fe-mineral(s) with broad 0.98 μm band	Low Al-white mica Al^{oct} = 1.651	XRD: quartz (M), muscovite (both 1M and 2M1 polytypes) EM: low Al-muscovite Al^{oct} = 1.701 LS: low Al-white mica Al^{oct} = 1.642
Calcite (23W)	CU02-11A	N37° 36' 54.5" W117° 14' 23.6" (GPS)	Goldfield Hills 5 km N of Wctr	N.D.	Calcite	XRD: calcite (M), quartz (tr) LS: calcite
Hydrated silica (Chalcedony and/or opal) (25X)	CU91-6A	N37° 32' 26" W117° 10' 15"	SE part of Ectr	N.D.	Chalcedony	XRD: quartz[/8] SEM: chalcedony LS: chalcedony

Spectral category (map code)	Sample ID	Sample location (NAD27 Datum)		Tetracorder mapping results spectral regions electronic (1 μm)	vibrational (2 μm)	Sample verification
Opal (26Y)	CU00-15E	N37° 32' 50" W117° 10' 01" (GPS)	Opal Hill, E central Ectr	N.D.	Opal	XRD: cristobalite and/or opal (M), quartz (M), calcite (m), tridymite (tr) LS: opal
Hydrated volcanic glass (27Z)	CU01-4A	N37° 37' 25" W117° 13' 55" (GPS)	Goldfield Hills 6 km N of Wctr	Trace Fe-mineral(s)	Hydrated volcanic glass	XRD: anorthite (M), sanidine (M), quartz (M), cristobalite or opal (m), nontronite (m), muscovite (tr), volcanic glass[/9] LS: hydrated volcanic glass, nontronite

See Figures 1 and 2 for geographic landmarks. Map code refers to sample collection locations shown in Figures 5A and 5B. N= north; E = east; W = west; S = south; Ectr = eastern center; Wctr = western center. Sample position is ±100m or better, unless GPS is specified then position is accurate to within ± 15m or better (using NAD27 datum). Digital spectra for these samples are downloadable from Clark et al. (2007). http://speclab.cr.usgs.gov/spectral.lib06
N.D. = no detection; XRD = X-ray diffraction analysis, (M) = major component 20 wt% or more, (m) = minor 5-20 wt%, (tr) = trace < 5 wt% (these are relative concentration levels based on operator expertise and experience and not on a quantitative algorithm); LS = laboratory spectroscopy; XRF = X-ray fluorescence; SEM = scanning electron microscopy; EM = electron microscopy; w.o. = well ordered; Med. = medium; bulk comp. = bulk composition.
Na/K = cation ratio; temp. = temperature, interm. = intermediate; Al^{oct} = cation number of Al in the octahedral position of white mica, sample compositions calculated using equations in Figures 9B and 11C for laboratory spectroscopy measurements.
[/1] XRD may not detect low abundances of white mica. [/2] Halloysite, in the kaolin group, is spectrally similar to well-ordered kaolinite mixtures with muscovite, illite, or montmorillonite and is sometimes confused with these mixtures. [/3] Trace hematite, goethite, jarosite and other Fe^{3+}-bearing minerals can be difficult for XRD to detect, even when red and yellow Fe^{3+} colors are present in the sample. [/4] Montmorillonite is a type of Al-smectite. [/5] Nontronite is a type of Fe-smectite. [/6] XRD unable to identify specific mineralogy of smectite. [/7] Spectroscopy cannot differentiate muscovite from illite at AVIRIS spectral resolution. [/8] XRD can have difficulty distinguishing between quartz and chalcedony. [/9] An "amorphous hump" in the XRD pattern may indicate the presence of volcanic glass.

Table A2. $^{40}Ar/^{39}Ar$ data for isotopic dating of rocks exposed at Cuprite, Nevada. [1]

Temp (°C)	$^{40}Ar_R$ [2]	$^{39}Ar_K$ [2]	$^{40}Ar_R/^{39}Ar_K$ [2]	$^{39}Ar/^{37}Ar$ [2,3]	$\%^{40}Ar_R$	$\%^{39}Ar$	Apparent age [4,5] (Ma at ± 1σ)
Sample: CU93-45 Sanidine from biotite-crystal-rich rhyolitic tuff (Tw) north of Western Center							
Latitude: N37° 35' 13" Longitude: W117° 13' 33" NAD27 datum, J = 0.007341, sample wt = 77.8 mg							
700	0.03071	0.02896	1.0604	11.15	10.9	0.2	13.99 ± 1.54
800	0.07670	0.03891	1.9712	16.65	50.8	0.3	25.92 ± 0.16
900	0.23078	0.11325	2.0378	25.83	46.5	0.8	26.79 ± 0.39
1000	3.68840	1.79169	2.0586	61.37	92.6	12.6	27.06 ± 0.05
1050	3.51330	1.71345	2.0504	84.69	96.9	12.0	26.95 ± 0.04
1100	4.05589	1.97584	2.0527	96.49	97.6	13.9	26.98 ± 0.04
1150	4.18656	2.03976	2.0525	110.21	98.5	14.3	26.98 ± 0.04
1200	4.45839	2.17406	2.0507	125.15	98.6	15.3	26.96 ± 0.04
1250	4.76953	2.32059	2.0553	121.75	98.4	16.3	27.02 ± 0.04
1450	4.19158	2.02894	2.0659	79.90	97.7	14.3	27.15 ± 0.04
Total gas age = 26.98 ± 0.05 Ma							
Plateau age (steps 4-9) = 26.99 ± 0.04 Ma (for 84.5 percent of the gas produced during heating)							
Isochron age (steps 3-10) = 27.04 ± 0.02 Ma; $(^{40}Ar/^{36}Ar)_I = 293 \pm 0.61$							
Sample: CU93-45 Biotite from biotite-crystal-rich rhyolitic tuff (Tw) north of Western Center.							
Latitude: N37° 35' 13" Longitude: W117° 13' 33" (GPS) NAD27 datum, J = 0.007879, sample wt = 50 mg							
700	0.06131	0.04597	1.3337	16.76	7.4	0.7	18.86 ± 1.54
800	0.21801	0.13758	1.5846	28.45	38.6	2.1	22.38 ± 0.14
900	1.18831	0.58756	2.0224	52.63	75.3	9.1	28.52 ± 0.04
950	1.65053	0.84387	1.9559	84.60	81.1	13.1	27.59 ± 0.05
1000	2.24344	1.15264	1.9464	115.40	84.8	17.9	27.45 ± 0.06
1050	1.94321	1.00026	1.9427	50.13	75.2	15.6	27.40 ± 0.04
1100	1.96083	1.00742	1.9464	9.75	70.8	15.7	27.46 ± 0.06
1150	1.77446	0.91359	1.9423	18.23	73.3	14.2	27.40 ± 0.05
1200	1.24298	0.64225	1.9354	18.78	68.9	10.0	27.30 ± 0.12
1350	0.19455	0.10074	1.9312	6.93	32.9	1.6	27.24 ± 0.29
Total gas age = 27.37 ± 0.08 Ma							
Plateau age (steps 5-10) = 27.41 ± 0.10 Ma (for 74.9 percent of the gas produced during heating)							
Isochron age (steps 5-10) = 27.46 ± 0.02 Ma; $(^{40}Ar/^{36}Ar)_I = 294 \pm 0.34$							
Sample: CU93-339C Alunite from altered Siebert Tuff (Tst) in Eastern Center.							
Latitude: N37° 32' 26" Longitude: W117° 10' 11" NAD27 datum, J = 0.007825, sample wt = 161 mg							
450	0.04832	0.00749	6.4513	6.72	0.4	0.1	88.79 ± 43.15
500	0.03327	0.04432	0.7507	11.05	0.1	0.4	10.57 ± 32.44
525	0.01231	0.06913	0.1781	14.67	0.0	0.7	2.51 ± 7.26
550	0.01675	0.06304	0.2657	28.90	0.1	0.6	3.75 ± 2.93
575	0.35950	0.67143	0.5354	360.05	1.2	6.8	7.54 ± 0.09
600	0.47236	0.92093	0.5129	637.52	2.7	9.3	7.23 ± 0.04
625	1.14764	2.37146	0.4839	347.49	5.6	23.9	6.82 ± 0.03
650	1.58102	3.23362	0.4889	1254.75	8.8	32.7	6.89 ± 0.05
675	0.88256	1.81491	0.4863	771.42	4.9	18.3	6.85 ± 0.06
700	0.30173	0.54149	0.5572	344.32	1.5	5.5	7.85 ± 0.03
750	0.11537	0.12798	0.9015	126.43	0.6	1.3	12.68 ± 0.64
850	0.02797	0.02636	1.0611	20.71	0.1	0.3	14.92 ± 36.09
1150	0.21621	0.01085	19.9272	0.91	0.2	0.1	261.37 ±12.22
Total gas age = 7.42 ± 0.39 Ma							
Plateau age (steps 7-9) = 6.86 ± 0.05 Ma (for 74.9 percent of the gas produced during heating)							
Isochron age (steps 5-13) = 6.77 ± 0.05 Ma; $(^{40}Ar/^{36}Ar)_I = 296 \pm 0.07$							

Table A2. $^{40}Ar/^{39}Ar$ data for isotopic dating of rocks exposed at Cuprite, Nevada.[1/] – Continued

Temp (°C)	$^{40}Ar_R$ [/2]	$^{39}Ar_K$ [/2]	$^{40}Ar_R/^{39}Ar_K$ [/2]	$^{39}Ar/^{37}Ar$ [/2,3]	$\%^{40}Ar_R$	$\%^{39}Ar$	Apparent age [/4,5] (Ma at ± 1σ)
Sample: CU93-316A fine-grained alunite from altered Cambrian Harkless phyllite (Ch) in Western Center.							
Latitude: N37° 32' 25"	Longitude: W117° 13' 11"	NAD27 datum, J = 0.00763, sample wt = 207.6 mg					
450	0.04691	0.00864	5.4294	5.60	1.4	0.1	73.25 ± 2.25
500	0.01771	0.00560	3.1625	12.02	1.5	0.1	42.97 ± 6.83
525	0.00911	0.00395	2.3063	11.71	1.8	0.0	31.51 ± 13.71
550	0.02750	0.02937	0.9363	45.47	3.0	0.3	12.84 ± 1.73
575	0.05588	0.09325	0.5992	78.23	7.2	0.9	8.23 ± 0.11
600	0.10772	0.20880	0.5159	134.86	14.3	2.0	7.09 ± 0.21
625	0.37145	0.73814	0.5032	239.46	25.2	6.9	6.91 ± 0.06
650	0.75514	1.59160	0.4744	367.00	47.0	14.9	6.52 ± 0.02
675	0.77046	1.63580	0.4710	361.56	45.5	15.3	6.47 ± 0.01
700	0.76060	1.61874	0.4699	322.97	40.4	15.2	6.46 ± 0.02
725	0.75075	1.59440	0.4709	332.34	40.3	14.9	6.47 ± 0.03
750	0.55462	1.14176	0.4858	279.47	36.0	10.7	6.67 ± 0.04
850	0.55024	1.13442	0.4850	257.17	19.8	10.6	6.66 ± 0.07
1150	0.40753	0.87050	0.4682	56.37	7.1	8.2	6.43 ± 0.07
Total gas age = 6.67 ± 0.04 Ma							
Plateau age (steps 8-11) = 6.48 ± 0.03 Ma (for 60.3 percent of the gas produced during heating)							
Isochron age (steps 1-14) = 6.41 ± 0.02 Ma; $(^{40}Ar/^{36}Ar)_I$ = 299 ± 0.31							
Sample: CU93-316B Bladed vein alunite from altered Cambrian Harkless phyllite (Ch) in Western Center							
Latitude: N37° 32' 13"	Longitude: W117° 12' 54"	NAD27 datum					
450	0.08820	0.29490	0.2991	24.60	14.1	1.4	4.02 ± 0.24
500	0.00639	0.00713	0.8962	8.26	25.1	0.0	12.03 ± 1.50
525	0.00099	0.00074	1.3378	1.34	10.4	0.0	18.05 ± 25.73
550	0.00204	0.00282	0.7234	11.48	15.7	0.0	9.67 ± 12.43
575	0.00175	0.01319	0.1327	18.57	7.1	0.1	1.79 ± 2.05
600	0.00928	0.03230	0.2873	32.17	21.7	0.1	3.86 ± 0.15
625	0.03375	0.08133	0.4150	40.53	40.2	0.4	5.58 ± 0.44
650	0.11735	0.26409	0.4444	52.37	59.0	1.2	5.97 ± 0.29
675	0.28845	0.62754	0.4596	63.24	75.2	2.9	6.18 ± 0.04
700	0.70498	1.51427	0.4656	67.70	77.1	7.0	6.25 ± 0.03
725	1.52291	3.29464	0.4622	74.05	91.5	15.1	6.21 ± 0.01
750	2.18815	4.73427	0.4622	79.69	78.1	21.7	6.21 ± 0.02
775	2.58687	5.49647	0.4706	78.16	35.3	25.2	6.32 ± 0.01
800	1.88451	4.02422	0.4683	82.99	28.3	18.5	6.29 ± 0.01
825	0.49685	1.03197	0.4814	71.53	20.7	4.7	6.47 ± 0.05
875	0.13605	0.27546	0.4939	52.05	8.5	1.3	6.63 ± 0.23
1100	0.03832	0.07916	0.4841	7.88	1.8	0.4	6.50 ± 0.32
Total gas age = 6.24 ± 0.04 Ma							
Plateau age (steps 9-12) = 6.21 ± 0.03 Ma (for 46.7 percent of the gas produced during heating)							
Isochron age (steps 9-16) = 6.21 ± 0.01 Ma; $(^{40}Ar/^{36}Ar)_I$ = 298 ± 0.29							

Uncertainty in ages given at ± 1σ level. Sample position is ±100 m or better, unless GPS is specified then position is accurate to within ± 15m or better. [/1] Mineral separates were prepared after crushing, grinding, and heavy liquid separation. For irradiation an aluminum canister was loaded with six quartz vials each of which was loaded with samples and standards. Standards were placed between every two unknowns as well as at the top and bottom of each vial. Each standard was degassed to release argon in a single 20-minute long heating step at 1,250ºC. Each sample was degassed stepwise in a series of 10 to 17 individual temperature steps for 20 minutes each. All analyses

were done in the Argon Laboratory, U.S. Geological Survey, in Denver, Colorado. A detailed description of analytical procedures in this laboratory is given in Snee (2002). Decay constants are those of Steiger and Jäger (1977). The standards for these experiments is hornblende MMhb-1 with percent K=1.555, $^{40}Ar_R = 1.624x10^{-9}$ mole/g, and K-Ar age = 520.4 Ma (Samson and Alexander, 1987).

/2 Abundances of "Radiogenic ^{40}Ar" and "K-derived ^{39}Ar" are reported in volts measured on a Mass Analyzer Products 215 rare-gas mass spectrometer using the Faraday cup. Conversion to moles can be made using a sensitivity of $9.736x10^{-13}$ moles argon per volt of signal. Corrections were made for volume, mass fractionation, trap current, radioactive decay of ^{37}Ar and ^{39}Ar, and interfering Ar isotopes. Mass discrimination in our mass spectrometer is routinely determined by measuring the ^{40}Ar /^{36}Ar ratio of atmospheric argon; our measured value is generally 298.9; the accepted value is 295.5. The calculated discrimination is applied to all samples and standards equally. Production ratios measured on pure K_2SO_4 and CaF_2 salts irradiated with the samples were used to correct for irradiation-produced ^{40}Ar (from K) and ^{39}Ar (from Ca). Corrections for Cl-derived ^{36}Ar were determined using the method of Roddick (1983). Production ratios determined for samples irradiated in the 1995 TRIGA reactor experiment are: $(^{40}Ar/^{39}Ar)_K = 7.92x10^{-3}$, $(^{38}Ar/^{39}Ar)_K = 1.309x10^{-2}$, $(^{37}Ar/^{39}Ar)_K = 1.8x10^{-4}$, $(^{36}Ar/^{37}Ar)_{Ca} = 2.68x10^{-4}$, $(^{39}Ar/^{37}Ar)_{Ca} = 6.85x10^{-4}$, $(^{38}Ar/^{37}Ar)_{Ca} = 4.4x10^{-5}$. Analytical data for "Radiogenic ^{40}Ar" and "K-derived ^{39}Ar" are calculated to five places; "$^{40}Ar_R/^{39}Ar_K$" is calculated to three decimal places. "Radiogenic ^{40}Ar", "K-derived ^{39}Ar", and "$^{40}Ar_R/^{39}Ar_K$" are rounded to significant figures using associated analytical precisions. Apparent ages and associated errors were calculated from unrounded data and then rounded using associated errors.

/3 To calculate apparent K/Ca ratios, divide $^{39}Ar/^{37}Ar$ value by 2.

/4 Uncertainties in calculation for the apparent date of individual steps for a sample were calculated using the equations of Dalrymple et al. (1981).

/5 The reproducibility of split gas fractions from selected monitors was used to calculate imprecision in J values. This imprecision is generally 0.1%, at the1σ level. J values for each sample were interpolated from adjacent standards. The uncertainty in each apparent age includes the uncertainty in the J value.